Charge sensing and spin relaxation times of holes in Ge hut wires

by

Lada Vukušić

September, 2018

A Thesis
Presented to the Faculty of the Graduate School of the
Institute of Science and Technology Austria, Klosterneuburg, Austria
in Partial Fulfillment of the Requirements for the Degree
Doctor of Philosophy

The dissertation of Lada Vukušić, titled *Charge sensing and spin relaxation times of holes in Ge hut wires*, is approved by:

Supervisor: Georgios Katsaros, IST Austria, Klosterneuburg, Austria

Signature: _____

Committee Member: Mikhail Lemeshko, IST Austria, Klosterneuburg, Austria

Signature: _____

Committee Member: Floris Zwanenburg, University of Twente, Enschede, The Netherlands

Signature: _____

Exam Chair: Bernd Bickel, IST Austria, Klosterneuburg, Austria

Signature: _____

I hereby declare that this thesis is my own work and that it does not contain other people's work without this being so stated; this thesis does not contain my previous work without this being stated, and the bibliography contains all the literature that I used in writing the dissertation.

I declare that this is a true copy of my thesis, including any final revisions, as approved by my thesis committee, and that this thesis has not been submitted for a higher degree to any other university or institution.

I certify that any republication of materials presented in this thesis has been approved by the relevant publishers and co-authors.

Signature: _____

Lada Vukušić
September, 2018

Abstract

A qubit, a unit of quantum information, is essentially any quantum mechanical two-level system which can be coherently controlled. Still, to be used for computation, it has to fulfill criteria. Qubits, regardless of the system in which they are realized, suffer from decoherence. This leads to loss of the information stored in the qubit. The upper bound of the time scale on which decoherence happens is set by the spin relaxation time.

In this thesis I studied a two-level system consisting of a Zeeman-split hole spin confined in a quantum dot formed in a Ge hut wire. Such Ge hut wires have emerged as a promising material system for the realization of spin qubits, due to the combination of two significant properties: long spin coherence time as expected for group IV semiconductors due to the low hyperfine interaction and a strong valence band spin-orbit coupling. Here, I present how to fabricate quantum dot devices suitable for electrical transport measurements. Coupled quantum dot devices allowed the realization of a charge sensor, which is electrostatically and tunnel coupled to a quantum dot. By integrating the charge sensor into a radio-frequency reflectometry setup, I performed for the first time single-shot readout measurements of hole spins and extracted the hole spin relaxation times in Ge hut wires.

Acknowledgments

Doing a PhD for five years, starting in one institution, finishing in another one, means that I have encountered and worked with many nice people who deserve to be mentioned here.

First and foremost, Giorgos Katsaros.
Prof. Katsaros, thank you for giving me the opportunity to perform my PhD thesis on such an exciting subject and to be a member of your research group :) (sorry, I could not resist).
Thank you, Giorgos, for an exciting time, first in the cleanroom (when in doubt, add more fabrication steps!), then in the lab (although your music choice is terrible). I am very happy that you correctly predicted that the good results would eventually come; one just has to be stubborn. Thank you for being the supervisor who still knows how to fabricate and measure a sample. Thank you for always having time for answering my questions. Thank you for correcting the articles, all over again. As no one will proof-read this, they will probably be randomly distributed.

Floris, Misha and Bernd, thank you for taking the role of the defence committee and the chair.

F. A. Zwanenburg, sorry for misspelling your name in the bibliography. Thank you for reading the thesis very carefully and noticing it. Thank you for all the comments and suggestions how to make it better and more understendable.

I have spent quite some time fabricating the perfect sample. Cleanroom crews and buddies, both from JKU and IST, helped me a lot. Alma, Ursula, Albin, Stephan, Salvo, Lubuna, Juan, Philipp: thank you!

Martin, thank you for growing so many wafers for us!

At some point I had a working sample, but I could not even start with the serious experiments wihout the help of MIBA boys Todor, Thomas, Thomas and Peter. Gyrator is a miracle!

Of course, having a working device and the wired probe still does not guarantee a successful experiment. We had many visitors at IST and each of them gave a valuable input which brought me closer to finally measure the T_1. With T. Watson I discussed how to analyse the tunnelling times. F. Kuemmeth explained me how to start with the pulsing and what to test first. M. Veldhorst pointed out some very

stupid mistakes in our first attempts to measure T_1. Soon after his visit things started to work! A. Laucht told us the multiblips were nothing weird.

Josipe, thank you for your patience with explaining me how to use the reflectometry setup, AWG, UHFLI and actually every instrument we have in the lab. Thank you for sitting next to me during the pulsing experiments and for writing the initial measurement scripts.

Josh, thank you for running the simulations and sorry for giving you the wrong parameters. Three times.

A very big thank you goes to all Spajorana members ever, for making such a great group with a particular sense of humour. Giorgos, Violetta, Hannes, Alisha, Elli, Raimund, Josip, Daniel, Matthias, Jason, Andrea, Josh, Luka: thank you all for always being ready to help and to listen to my complaints. A special bonus for Hannes, who has to drive 40km/h slower when I am in the car WHILE listening to my complaints with music for young people in the background (or a very bad Christmas CD). Elli, thank you for the encouraging messages and dog videos. Daniel, thank you for often being the only one who appreciates my jokes. Luka, thank you for reminding me to chill. Andrea and Matthias, thank you for being the voice of reason in the group. And for raising the fashion and chocolate standards (guess who's who).

Special thanks go to JKU lunch-and-ducks-worshippers crew. I miss all of the nonsense conversations! I should also not forget to thank the Elitebüro - Office of Excellence members: Magdalena, Johannes, Marcus, Daniel, Martin, Hannes and Hui, for creating a great atmosphere. Yourhighness, thank you for playing football clubs anthems and Skype ringtone all over again. Almost comparable to Yeah Boi screams at IST.

Mami ide devet pusa jer se vrlo dobro nosi sa činjenicom da joj je kći fizičarka.

And of course, thank you, Konrád, for always being by my side. Szeretlek!

About the Author

I completed an integrated bachelor and master programme at the Physics department of Faculty of Science at the University of Zagreb and obtained the Master degree of Science in Physics in 2012. In 2012 I spent one semester at the Faculty of Physics at the University of Vienna as an exchange student. After I finished my physics studies, I started in 2013 a PhD programme at the Johannes Kepler University Linz, at the Institute of Semiconductor and Solid State Physics. Three years later I moved to IST Austria together with my supervisor.

List of Publications

1. Heavy-hole states in germanium hut wires
   Hannes Watzinger, Christoph Kloeffel, Lada Vukušić, Marta D. Rossell, Violetta Sessi, Josip Kukučka, Raimund Kirchschlager, Elisabeth Lausecker, Alisha Truhlar, Martin Glaser, Armando Rastelli, Andreas Fuhrer, Daniel Loss and Georgios Katsaros
   Nano Lett. **16**, 6879 - 6885 (2016)

2. Fast hole tunneling times in germanium hut wires probed by single-shot reflectometry
   Lada Vukušić, Josip Kukučka, Hannes Watzinger and Georgios Katsaros
   Nano Lett. **17**, 5706 - 5710 (2017)

3. Ge hole spin qubit
   Hannes Watzinger, Josip Kukučka, Lada Vukušić, Fei Gao, Ting Wang, Friedrich Schäffler, Jian-Jun Zhang and Georgios Katsaros
   Submitted, preprint at https://arxiv.org/pdf/1802.00395.pdf

4. Single-shot readout of hole spins in Ge
   Lada Vukušić, Josip Kukučka, Hannes Watzinger, Joshua M. Milem, Friedrich Schäffler and Georgios Katsaros
   Submitted, preprint at https://arxiv.org/pdf/1803.01775.pdf

Table of Contents

List of Tables

List of Figures

List of Abbreviations

ALD Atomic layer deposition

AWG Arbitrary waveform generator

BOE Buffered oxide etch

DC Direct current

DQD Double quantum dot

EHT Effective hole temperature

ES Excited state

GS Ground state

HF Hyperfine

HH Heavy-hole

HW Hut wire

LH Light-hole

MBE Molecular beam epitaxy

QD Quantum dot

PCB Printed circuit board

PMMA Poly(methyl methacrylate)

QPC Quantum point contact

RA Reflected amplitude

RF Radio-frequency

SEM Scanning electron microscope

SET Single-electron transistor

SHT Single-hole transistor

SK Stranski-Krastanov

SO Spin-orbit

SNR Signal-to-noise ratio

UHFLI Ultra high frequency lock-in

UHV Ultra high vacuum

xx

1 Introduction

1.1 Motivation

Quest for qubits

Living in the era of information technology, we experience a high demand for increased computational speed and miniaturization of the computers' processors hearts - the transistors. Industry has followed Moore's law successfully, but further shrinking of the devices may hit soon against a "wall". Channel lengths comparable with the wavelength of electrons bring quantum rules in play. In classical computers information is stored in bits, which take the discrete values 0 and 1. Because of superposition, a quantum state is a linear combination of 0 and 1 and it can form a quantum bit - the so-called qubit. Such qubits can be used for the realization of a quantum computer which is predicted to outperform classical ones in specific tasks [1, 2]. Quantum computers and their properties are not only interesting for basic science, but might have many practical advantages over the classical ones. They could help us design new materials more efficiently (room temperature superconductors, fertilizers), enable rapid searches in unstructured databases, help in identification of genetic diseases, solve complex optimization problems (weather and financial market forecasting) and, finally, improve cryptography and internet security [3, 4].

Nowadays, quantum computers are an object of an intensive experimental and theoretical research. In the last few years big companies like IBM, Microsoft, Google and Intel showed interest and are now supporting research in the field of quantum computation. Even though first devices are currently being produced, they cannot be used for anything that a standard PC can do almost trivially. The development of these devices is still part of fundamental research.

But what is actually a qubit? A qubit is essentially a two-level system which can be realized in different systems and ways. Among the most prominent ones are the polarization state of a photon [5],

energy levels in trapped atoms [6, 7], an-harmonic levels in superconducting circuits [8] or confined spins [9].

What are the criteria a useful qubit needs to satisfy? In 2000 DiVincenzo formulated five requirements for the physical implementation of quantum computation. One needs to have (i) a scalable physical system with well characterised qubits, (ii) a possibility to initialize the qubit state, (iii) a possibility to read out the qubit state, (iv) decoherence times long enough to do substantial amount of qubit operations, (v) a universal set of quantum gates [10]. For implementing quantum communication, i.e transmission of intact qubits from place to place, two additional requirements have to be met. (vi) stationary qubits (qubits for reliable local computation) and flying qubits (qubits that are readily transmitted from place to place) have to be interconvertable and (vii) flying qubits have to be faithfully transmitted between specified locations. The central challenge in actually building quantum computers is maintaining the simultaneous abilities to control quantum systems, to measure them, and to preserve their strong isolation from uncontrolled parts of their environment. Furthermore, quantum error correction is essential if one is to achieve fault-tolerant quantum computation that can deal not only with noise on stored quantum information, but also with faulty quantum gates, faulty quantum preparation and faulty measurements [11, 12]. A high quality factor, the ratio between the qubit dephasing (defined in the next chapter), and manipulation time T_Φ/T_π, is vital for accomplishing it.

From the scalability point of view, solid state qubits, especially spin qubits, have a big advantage. The nanofabrication techniques are very similar to those of the microelectronics industry which allows integrating multiple qubits in millimetre size chips.

Spin qubits

One of the most famous proposals for realizing a qubit in a solid state system is the one by Loss and DiVincenzo [9]. There, a spin of a particle confined in a quantum dot is used as a qubit. Depending on the type of the two-level system creating the qubit, we distinguish between spin 1/2 (single spin) qubits [13], singlet-triplet qubits [14] and exchange-only qubits [15]. In addition, spins can be confined also by using the attractive potential of individual impurities like nitrogen vacancy centres in diamond [16–18] or phosphorus donors in silicon [19–21].

Investigated mainly in the III-V material systems until 2010, spin qubits had rather short dephasing times (T_Φ=10 ns, [14]), predominantly due to the hyperfine interaction arising from the non-zero nuclear spins. Silicon, however, together with other group IV elements, has only one isotope having nuclear spin different from zero. Furthermore, it can be isotopicaly purified [22] and thus provide longer relaxation and dephasing times [20, 23–25]. Indeed, switching materials showed a big improvement in both the dephasing times (T_Φ=160 μs, [20]) and quality factor. The highest quality factor reported up to

now ($T_\Phi/T_\pi = 680$, [26]) is achieved using a micrometre-sized cobalt ferromagnet to create a magnetic field gradient in order to manipulate electrically the electron spins confined in ^{28}Si. However, such an approach could be problematic in terms of scale-up. These micromagnets are necessary because the low spin-orbit interaction prevents fast electrical manipulation of isolated electron spins in the first place. Alternatively, a qubit can as well be encoded in a hole spin. The strong spin-orbit interaction of holes, especially in germanium, grants the possibility for fast all-electric spin manipulation [27–29].

Hole spin qubits

Despite the predicted great properties for fast, long-lived qubit realization, the spin dynamics in Si or Ge hole systems has not been studied much. Experimental work has been done on Ge/Si core-shell nanowires, giving relaxation times T_1 of 0.6 ms [30] and dephasing times T_Φ of 0.18 μs for a singlet-triplet qubit [31]. Very recently, a hole spin qubit has been demonstrated in a nanowire field-effect transistor created in natural Si [32]. Even with all-electric manipulation, it showed a rather low quality factor, T_Φ/T_π being only 4.3, presumably due to the heavy-hole light-hole mixing and the hyperfine interaction still existing in non purified samples.

On the other hand, quantum dots formed in Ge hut wires create an appealing platform for building quantum devices with rich physics and technological potential. The confined hole wave function is almost of purely heavy-hole character [33], which can lead to long spin coherence times [34]. Furthermore, they are monolithically grown on Si, without the use of any catalyst, allowing the use of CMOS compatible processes for the device fabrication [35]. Very recently the first hole spin qubit formed in Ge hut wires grown with natural Ge has been demonstrated and a quality factor of 18 has been reported [36].

Spin qubits and DiVincenzo criteria

Experiments with spin 1/2 qubits show that they fulfill the DiVincenzo criteria. A scalable system with well characterized qubits is achieved by trapping single charges in (usually) gate-defined quantum dots [9]. The initialization of the state can be done by the deterministic loading of the spin ground state [23]. The qubit state readout is done by spin-to-charge conversion, essentially in a single-shot manner and a universal set of quantum gates is given by single-spin Rabi oscillations and a Ramsey-like rotation experiment [37–39]. Coherence times much longer than the gate-operation time can be achieved in ^{28}Si [26]. Furthermore, first steps have been made towards long-distance spin-spin coupling in Si [40, 41], important for implementing long distance quantum entanglement.

1.2 Thesis outline

The majority of the work presented in this thesis is done on self-assembled Ge hut wires. In short, we demonstrated charge sensing and for the first time single-shot spin readout measurements for holes. After I introduce the system and give the needed theoretical background, I will describe the fabrication of the devices suitable for spin relaxation measurements, which essentially need a charge sensor. Due to the strong spin-orbit coupling, which in general leads to shorter relaxation times, we integrated the charge sensor into a radio-frequency reflectometry setup. Big part of this thesis deals with the characterization of the devices ultimately used for spin readout measurements. Finally, I will present spin readout experiments and the obtained hole spin relaxation times. However, to tell the story from the beginning, I will also describe fabrication and initial measurements on other self-assembled nanostructures. These efforts finally led to the devices suitable for hole spin relaxation measurements.

2 Self-assembled SiGe nanostructures

2.1 Growth of SiGe self-assembled nanostructures

The work presented here is done on self-assembled SiGe nanostructures, created via the Stranski - Krastanov (SK) growth mode [42]. They are grown by the molecular beam epitaxy (MBE) technique, an epitaxy method used for the deposition of thin crystalline films under ultra-high vacuum (UHV) conditions. With this technique, the material flow and the temperature can be controlled very accurately, which results in a defect-free growth [33]. In our case, Ge, a material with a larger lattice constant (5.66 Å), is deposited on a Si substrate (normally a commercial Si(001) wafer), a material with a smaller lattice constant (5.43 Å). This lattice mismatch between Ge and Si causes a build-up of strain in the growing film. In the SK growth mode, the Ge lattice initially tries to adjust to the Si lattice below, but after the epitaxial growth of a few monolayers of Ge, islands form as a result of the competition between the strain energy release and the surface energy increase. The first islands appearing during the growth are hut clusters, which then evolve into pyramids with square base, larger multifaceted domes and dislocated islands called superdomes [43]. The type of the grown islands and their density depends on the growth temperatures and the amount of deposited material. Furthermore, in 2012 it was shown that annealing of hut clusters can lead to the formation of 1D nanowires (hut wires) [35, 44]. If one wants to use such nanostructures for making devices, a few nanometre (2-4 nm) thick Si cap has to be grown as well, as it prevents formation of Ge oxide. Both Si and Ge are oxidizing, but GeO_2 is soluble in water and hence requires additional passivation, while SiO_2 is easily and controllably removed with etching processes. A schematic of the evolution of the growth of Ge islands on Si and the strain relaxation taking place during the formation of a 3D island are shown in Figure 2.1.

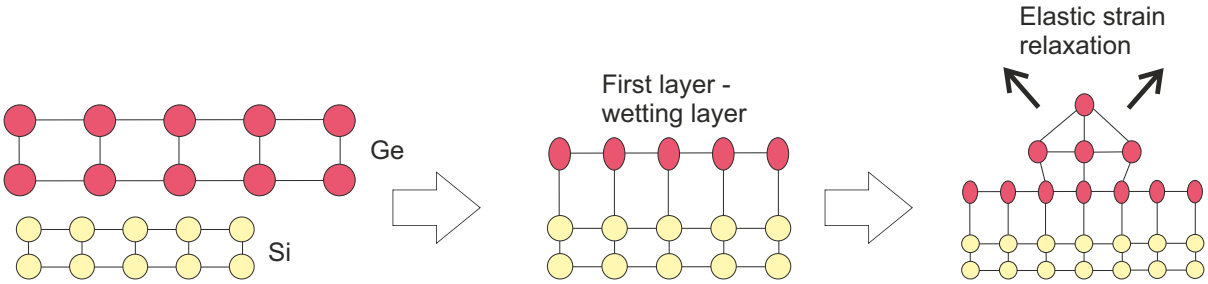

Figure 2.1: Principle of the SK growth mode. The Si lattice is shown in yellow, while the Ge lattice in pink. After the wetting layer is formed, the stored elastic strain in the growing film relaxes through the formation of islands.

Dome islands and hut wires

All the fabrication and experiments presented here were performed on dome islands (Figure 2.2 (a)) and hut wires (HWs) (Figure 2.2 (b)). They were grown at JKU Linz, by Martin Glaser (dome islands) and Hannes Watzinger (HWs). The dome islands have a size of about 80 nm x 80 nm x 20 nm. Their aspect ratio, which is defined by the ratio of the island height versus the square root of the island's base area, is ≈ 0.25. HWs, on the other hand, have a rectangular base area with an average width of about 20 nm, height of about 2 nm and typically grow up to 1 μm, resulting in a much lower aspect ratio of ≈ 0.04. This is the reason why HWs have stronger confinement potential in the [001] direction and strain than dome islands or typical core/shell type nanowires [45]. Additionally, HWs grow only in two crystallographic orientations, (100) and (010). Both type of nanostructures can be grown on pre-patterned substrates (Figure 2.2 (c)), which makes them suitable for building complex devices [46–48].

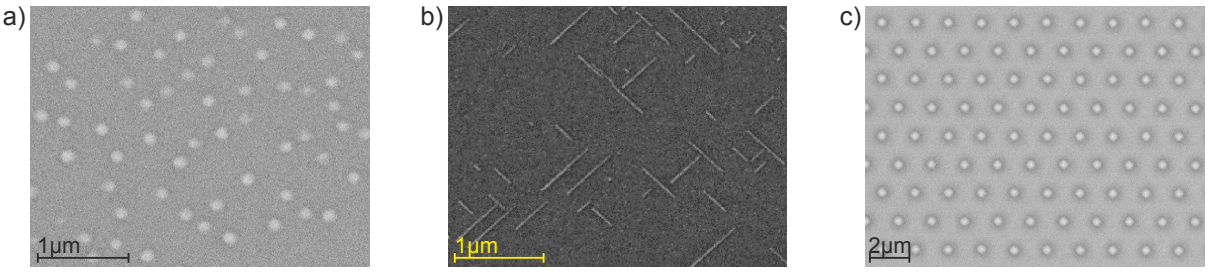

Figure 2.2: (a) SEM image of dome islands. (b) SEM image of hut wires. (c) SEM image of dome islands grown on pre-patterned substrates.

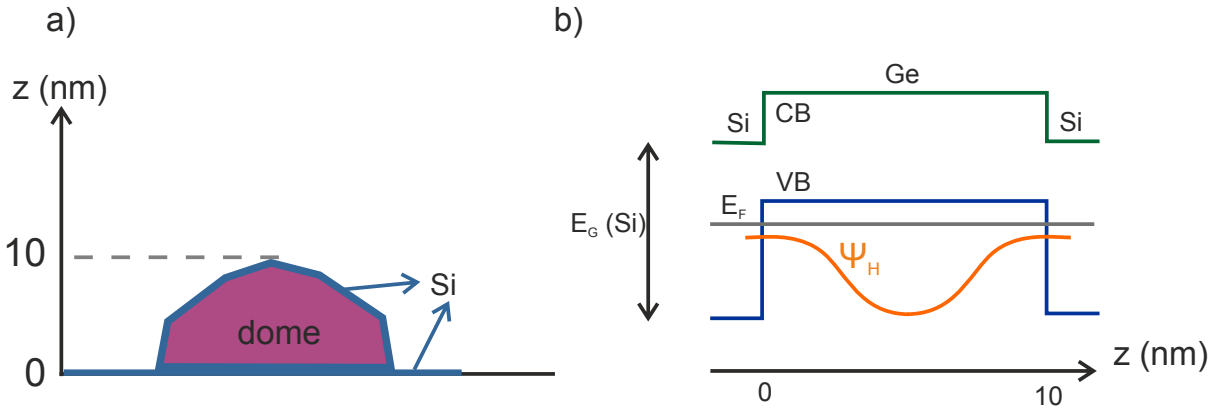

Figure 2.3: (a) Scheme of a dome with a simplified compositional cross-section. (b) corresponding conduction band (CB) and valence band (VB) alignment scheme, where E_G(Si) is the Si band-gap, E_F the Fermi energy and Ψ_H represents the hole wave function.

2.2 Band structure and its properties

Heavy and light holes

Due to the type-II band alignment in Si-Ge-Si, in the described structures a confinement potential for holes is created [49]. Holes have an orbital angular momentum quantum number $l = 1$, with three possible projections, or magnetic quantum numbers: $m = -1, 0, 1$. Taking the spin into account makes the valence band 6-fold degenerate. With spin-orbit interaction included, the total angular momentum is $J = \frac{3}{2}$ or $J = \frac{1}{2}$. The total angular momentum $J = \frac{3}{2}$ is associated with the so-called heavy-hole (HH) and light-hole (LH) band. Projections $m = \pm\frac{3}{2}$ correspond to HH states, $m = \pm\frac{1}{2}$ to LH states. The total angular momentum $J = \frac{1}{2}$ is associated with the so-called *split-off* band. The energy separation of the split-off band from the HH-LH bands (Δ_{SO}) gives the strength of the spin-orbit interaction. In bulk, HH and LH bands are degenerate, but this degeneracy can be lifted by strain and confinement; the larger the strain and confinement, the larger the HH-LH band splitting. In quantum wells, band dispersions depend on the direction of a wave vector $\vec{k}$. Furthermore, the coupling between the bands leads to anticrossing behaviour. A simplified band diagram of holes in a quantum well is shown in Figure 2.4, for a confinement potential in the z-direction (or for tensile strain along the z-direction). Confinement in 0D systems (often described with the *particle in a box* picture) results in the formation of bound states. Hole waves with wave vectors +k and -k will form a standing wave, which represents a 0D eigenstate Ψ_n of the system, with eigenenergy E_n. For the lowest energy, the wave function will be predominantly HH-like, but as the energy increases, the hole eigenstates will acquire more and more LH character.

Not only the angular momentum of a HH and a LH is different, but also their effective masses. They are

given by the following formulas:

$$m^*_{HH} \approx \frac{1}{\gamma_1 - 2\gamma_2}, \qquad m^*_{LH} \approx \frac{1}{\gamma_1 + 2\gamma_2}, \tag{2.1}$$

in the z-direction and

$$m^*_{HH} \approx \frac{1}{\gamma_1 + \gamma_2}, \qquad m^*_{LH} \approx \frac{1}{\gamma_1 - \gamma_2}, \tag{2.2}$$

in the x,y-directions, where γ_1, γ_2 are Luttinger parameters [50]. Since $\gamma_1 > \gamma_2$ (for Ge, $\gamma_1 = 13.38$, $\gamma_2 = 4.24$ [51]) and both are positive in most diamond- and zinc-blende-type semiconductors, for the direction of motion perpendicular to the confinement potential 'heavy' holes will have lower effective mass than 'light' holes. Thus, in order to avoid misinterpretations it might be actually better to describe the bands by the projection of their total angular momentum.

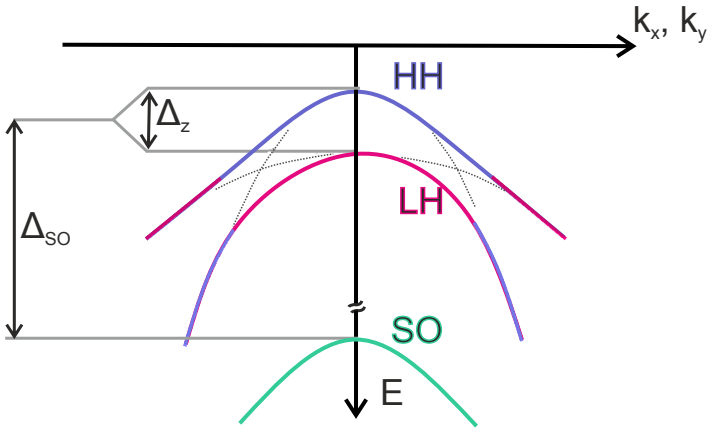

Figure 2.4: Simplified, qualitative band diagram of holes in a quantum well. The energy is denoted with E and the in-plane wave vectors with k_x and k_y. The HH and a LH branches are separated by Δ_z due to the presence of strain and confinement. The HH have lower energy at $\vec{k}$=0, but their energy rises more rapidly with $\vec{k}$ so the HH branch approaches the LH branch. Coupling between them leads to anticrossing behaviour. The split-off band appears as a result of the SO interaction in the valence band, quantified by Δ_{SO}.

2.2.1 Spin properties

The spin interacts with the environment through the spin-orbit (SO) interaction and the hyperfine (HF) interaction. These interactions can destroy information stored in the spin. We distinguish two processes contributing to it: dephasing (happening on a time scale T_Φ) and relaxation (happening on a time scale T_1). The latter happens when a spin relaxes from any prepared state to the ground state and energy is dissipated into environment. The former corresponds to the loss of information stored in the phase

of the qubit's eigenstate. During the dephasing process energy is conserved. The combination of both leads to the qubit decoherence, associated with a time scale T_2. It can be shown [52] that

$$\frac{1}{T_2} = \frac{1}{2T_1} + \frac{1}{T_\Phi}. \tag{2.3}$$

Spin-orbit interaction

The SO interaction is a relativistic interaction of a particle's spin with its motion inside a potential. It couples the orbital motion of a particle to its spin degree of freedom via electric fields, which transform into an effective magnetic field when observed from the particle's perspective. These electric fields can originate either from the bulk inversion asymmetry (Dresselhaus SO interaction), or from the structural inversion asymmetry (Rashba SO interaction) [53]. The above mentioned coupling can be understood as an effective Zeeman energy and can mix states with opposite spins, which leads to spin relaxation. In fact, the SO interaction is the dominating mechanism in spin relaxation [54, 55] and it scales with the atomic number of the atom.

The Hamiltonian for the SO interaction is given by

$$H_{SO} = \frac{\hbar}{4c^2m^2}\left(\vec{\nabla}\vec{V} \times \vec{p}\right)\vec{\sigma}, \tag{2.4}$$

where $\vec{\sigma}$ are the Pauli spin matrices [51]. The SO interaction in atomic physics is usually expressed in terms of angular momentum $\vec{L}$ and the spin $\vec{S}$ as

$$H_{SO} = \lambda \vec{L}\vec{S}, \tag{2.5}$$

where the constant λ is referred to as the SO coupling.

For holes, the spin and the orbital degrees of freedom are in general strongly intermixed, which occurs primarily due to the SO splitting of the valance band. Additionaly, holes in Ge HWs are expected to exhibit very strong SO interaction, due to the direct Rashba SO interaction [56].

Hyperfine interaction

Although a strong SO interaction can reduce the hole spin relaxation time, for pure HH states the dephasing time should be enhanced. From 2.3 it follows that in the case when T_Φ is long enough, the

upper limit for the coherence time T_2 is given by the relaxation time T_1. A longer dephasing time would thus allow more operations on a qubit before it completely decoheres.

The net magnetic field originating from the host nuclei fluctuates around its average value as a result of the redistribution of the nuclear spin polarization due to dipolar coupling or through virtual excitations [57]. As a consequence, it always points in a different direction, decreasing the qubit dephasing time. Nevertheless, there are cases when the unwanted net magnetic field points in a perpendicular direction and its influence can be reduced, as it will be shown it the following short analysis.

The hyperfine interaction Hamiltonian can be split into three terms:

$$H_{\mathrm{HF}} = \frac{Ze^2 g_e g_{nucl}}{4 m_e m_{nucl} c^2} \left(\underbrace{\frac{8\pi}{3} \vec{S} \cdot \vec{I} \delta(\vec{r})}_{\text{1st term}} + \frac{1}{r^3} \left[\underbrace{3(\hat{r} \cdot \vec{S})(\hat{r} \cdot \vec{I}) - \vec{S} \cdot \vec{I}}_{\text{2nd term}} + \underbrace{\vec{J} \cdot \vec{I}}_{\text{3rd term}} \right] \right), \tag{2.6}$$

where the first term is the Fermi contact interaction, the second is a dipole-dipole interaction and the third is the coupling of the angular momentum to the nuclear spin. For a system with holes, which have *p* symmetry, the contact term vanishes, already reducing the influence of the hyperfine interaction. However, the other two terms can stil contribute significantly [34]. In case of purely HH states, the hyperfine interaction is of Ising type and can be written as [58]:

$$H_{\mathrm{HF}} = \sum_k^N A_k S_z I_k^z, \tag{2.7}$$

where A_k is the coupling of the HH to the *k*th nucleus, S_z is the hole spin operator, and I_k^z is the *z* component of the *k*th nuclear spin operator $\vec{I}_k$. An alternative description of the effect of the nuclei on the hole spin is to treat the ensemble of nuclear spins as an apparent magnetic field $\vec{B}_N$, called the Overhauser field. The hyperfine interaction can be then written as

$$H_{\mathrm{HF}} = g \mu_B \vec{B}_N \cdot \vec{S}. \tag{2.8}$$

For HH, $\vec{B}_N = B_N \hat{z}$, i.e. the Overhauser field points in one certain direction. When we know the direction of the Overhauser field, we can apply the external magnetic field B_0 which creates the spin qubit in a certain orientation which can then reduce the effect of the hyperfine interaction, as can be seen below.

In the case when the Overhauser field is perpendicular to the applied external magnetic field B_0, the Zeeman splitting $E_Z^{\perp} = g\mu_B B_{\mathrm{tot}}$ is

$$E_Z^{\perp} = \sqrt{(g\mu_B B_N)^2 + (g\mu_B B_0)^2} = g\mu_B B_0 \sqrt{1 + \left(\frac{g\mu_B B_N}{g\mu_B B_0}\right)^2}. \tag{2.9}$$

.

Since $B_N << B_0$ we can use the Taylor expansion of $\sqrt{1+x^2}$ to get:

$$E_Z^{\perp} \approx g\mu_B B_0 + \frac{g\mu_B B_N^2}{2B_0}, \tag{2.10}$$

so the fluctuation in the Zeeman splitting due to the Overhauser field $\Delta E_Z^{\perp}$ is

$$\Delta E_Z^{\perp} = \frac{g\mu_B B_N^2}{2B_0} \tag{2.11}$$

.

When the Overhauser field is parallel to the applied external magnetic field B_0 the total Zeeman splitting is:

$$E_Z^{\parallel} = g\mu_B (B_N + B_0) \tag{2.12}$$

and the fluctuation is:

$$\Delta E_Z^{\parallel} = g\mu_B B_N. \tag{2.13}$$

As $B_N << B_0$, the fluctuating Zeeman splitting $\Delta E_Z^{\perp}$ is much smaller than $\Delta E_Z^{\parallel}$. That means that the qubit coherence for a system with purely HH states can be longer preserved if the applied external magnetic field is perpendicular to the nuclear Overhauser field. As for Ge HWs it has been shown that the lowest energy states consist almost exclusively (> 99 %) of HH states [33], this might be a promising way of how to increase the coherence of the hole qubit even without isotopical purification.

3 Basics of transport in quantum dots

3.1 Transport in single quantum dots

Besides in self-assembled semiconductor nanostructures, there are many other ways to realize QDs in different materials, for instance in one dimensional carbon nanotubes [59] or in two dimensional hole (electron) gases [60]. Regardless of its origin, in quantum electronics a QD can be understood as a box filled with charge carriers and coupled via tunnel barriers to source and drain reservoirs, with which charge carriers can be exchanged (Figure 3.1). The tunnel barrier is often understood as a resistor and a capacitor connected in parallel. Usually an additional tuning knob is added, a capacitively coupled gate electrode. This type of double tunnel-junction devices with a gate terminal are known as single-hole/electron transistors (SHTs/SETs).

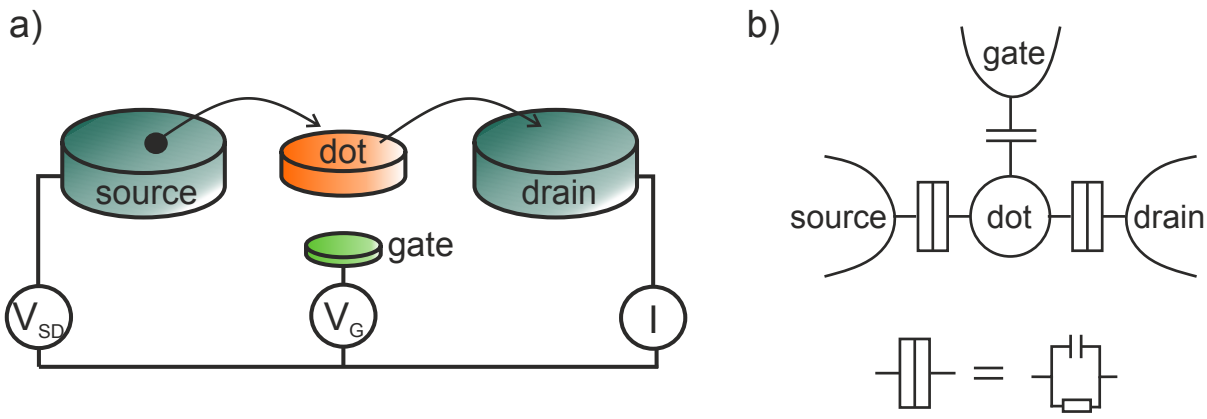

Figure 3.1: (a) Schematic picture of a quantum dot. The QD is connected to source and drain reservoirs via tunnel barriers, allowing the current through the device I to be measured in response to a bias voltage V_{SD} and a gate voltage V_G. (b) Classical electric circuit diagram representation of a single QD.

On a nanoscale, adding just one carrier from the leads to the dot results in a huge change of the electrostatic energy, called charging energy, E_C, which has to be paid for every charge carrier added to

the dot. Besides that, due to the confinement of charge carriers in all three spatial dimensions, energy levels in QDs show a discrete energy spectrum.

The spatial confinement of carriers in a QD leading to the discrete spectrum takes place when their de Broglie wavelength is comparable to the size of the dot:

$$\lambda = \frac{h}{\sqrt{2m^* k_B T}}, \tag{3.1}$$

where h is the Planck constant, m^* the effective mass, k_B the Boltzmann constant and T temperature. For typical effective masses (m^* = 0.067 m_0 - 1 m_0), formula 3.1 gives sizes of about 10 nm for room temperature and hundreds of nm at 4 K, meaning that we have to use either very low temperatures or a very small QD. Though 10 nm QDs can be routinely fabricated nowadays, there is an additional constrain: the broadening of the Fermi distribution of the leads contacting the QD.

In order that the quantized levels in QDs can be observed, the thermal energy of carriers must be lower than the energy level separation:

$$k_B T \ll \Delta E \sim \frac{1}{L^2}, \tag{3.2}$$

where L is the dimension of a QD. For typical QD dimensions of few hundreds of nm, this gives energy level separations of few tens of μeV, implying that the use of cryogenic temperatures is necessary.

The charge states in QDs can be described with a capacitance model [61]. In this description the interaction effects of the charges between each other and with the gate electrodes are represented by a capacitance matrix which relates the induced charge on each of the electrodes to the potential change V_j:

$$Q_i = \sum_{j=0}^{n} C_{ij} V_j + Q_i^{(0)}. \tag{3.3}$$

Here C_{ij} are the elements of the capacitance matrix describing the arrangement of conductors, Q_i denotes the charge that is induced on the electrostatic potentials V_j on the gates and in the source and drain contacts and the charges $Q_i^{(0)}$ are the charges that reside on the gates and on the dot if all voltages are zero. If we denote the QD with index i = 0, equation 3.3 can be written as

$$Q_0 = \sum_{j=0}^{n} C_{0j} V_j + Q_0^{(0)} = \sum_{j=1}^{n} C_{0j} V_j + C_{00} V_0 + Q_0^{(0)}, \tag{3.4}$$

where C_{00} is the self-capacitance of the QD. Due to overall charge neutrality C_{ij} obey the relation $\sum_{i=0}^{n} C_{ij} = 0$ and C_{00} is therefore given by:

$$C_{00} \equiv -\sum_{j=0}^{n} C_{0j}. \tag{3.5}$$

In this model, the total energy of a dot with N charges is

$$U(N) = \sum_{n=1}^{N} \varepsilon_n^{(0)} + \frac{e^2 N^2}{2C_{00}} + |e|N \sum_{i=1}^{n} \frac{C_{0i}}{C_{00}}(V_i - V_i^{(0)}), \tag{3.6}$$

where $\varepsilon^{(0)}$ is the energy of a discrete single-particle quantum level. The energy required to add a single charge to the QD is called the electrochemical potential and it is defined as

$$\mu(N) \equiv U(N) - U(N-1). \tag{3.7}$$

In this model it is equal to

$$\mu(N) = \varepsilon_N^{(0)} + \frac{e^2}{C_{00}}(N - \frac{1}{2}) + |e| \sum_{i=1}^{n} \frac{C_{0i}}{C_{00}}(V_i - V_i^{(0)}). \tag{3.8}$$

The first term in this expression is the chemical potential needed to add the Nth charge to the QD. The second one is the charging energy term and the last one, gate voltage dependent, is the electrostatic potential.

The electrochemical potentials of the transitions between successive ground states are spaced by the so-called addition energy:

$$E_{add} = \mu(N+1) - \mu(N) = E_C + \Delta\varepsilon. \tag{3.9}$$

It consists of a purely electrostatic part - the charging energy ($E_C = e^2/C_{00}$) - plus the energy spacing between two discrete quantum levels ($\Delta\epsilon$).

How charges move through a quantum device is strongly dependent on the energy scales. Internal energy scales, fixed by the confinement potential, need to be compared to the external ones (k_BT and eV_{SD}). The relevant internal energy scales include the already mentioned charging energy E_C and the level spacing $\Delta\varepsilon$, the level broadening hΓ and the Kondo temperature T_K [62]. Figure 3.2 schematically shows different transport regimes for different energy scales.

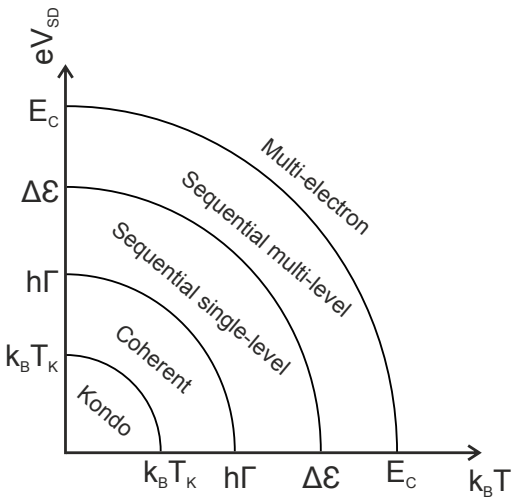

Figure 3.2: Different transport regimes as a function of the external energy scales k_BT and eV_{SD}. The transitions between regimes take place on the order of the internal energy scales E_C, $\Delta\varepsilon$, $h\Gamma$ and T_K. Adapted from [62].

Tunnelling processes

In order that electrical transport can take place, the addition energy has to be overcome by an external voltage - a bias voltage. If this condition is not met, the QD is in the so-called Coulomb blockade: the number of charge carriers in the dot remains constant and no current flows through the dot. When $E_C \gg eV_{\mathrm{SD}}$, we speak about sequential tunnelling processes. In this case the wave function phase is partially randomized by the scattering events that occur in the double barrier structure. Coulomb blockade can be also lifted by changing the voltage applied to the gate electrode, an electrode capacitively coupled to the dot, which shifts the electrochemical potentials in the dot with respect to the source and drain reservoirs.

For a QD filled with holes, which is our case, and for $eV_{\mathrm{SD}} \ll \Delta\varepsilon$, if the electrochemical potential $\mu(N)$ lies below the bias window (Figure 3.3 (a)), the hole number on the dot is N-1. That number stays constant and the measured current is equal to zero (Figure 3.3 (c)). By increasing the gate voltage, the electrochemical potential $\mu(N)$ can be brought in the bias window and transport can take place (Figure 3.3 (b)). Only one hole is tunnelling from the source onto the dot; the next one can tunnel onto the dot only after the first one has tunnelled to the drain. This single-hole cycle is manifested as a current peak (Figure 3.3 (c)). It is called Coulomb peak and the tunnelling process is called sequential single-level tunnelling process.

In the regime where $\Delta\varepsilon \ll eV_{\mathrm{SD}} \ll E_C$ the bias window is so large that also transport through excited states can take place. Additional levels in the bias window make more paths for hole tunnelling through the dot available (Figure 3.4 (a)). In this case we speak about sequential multi-level tunnelling process.

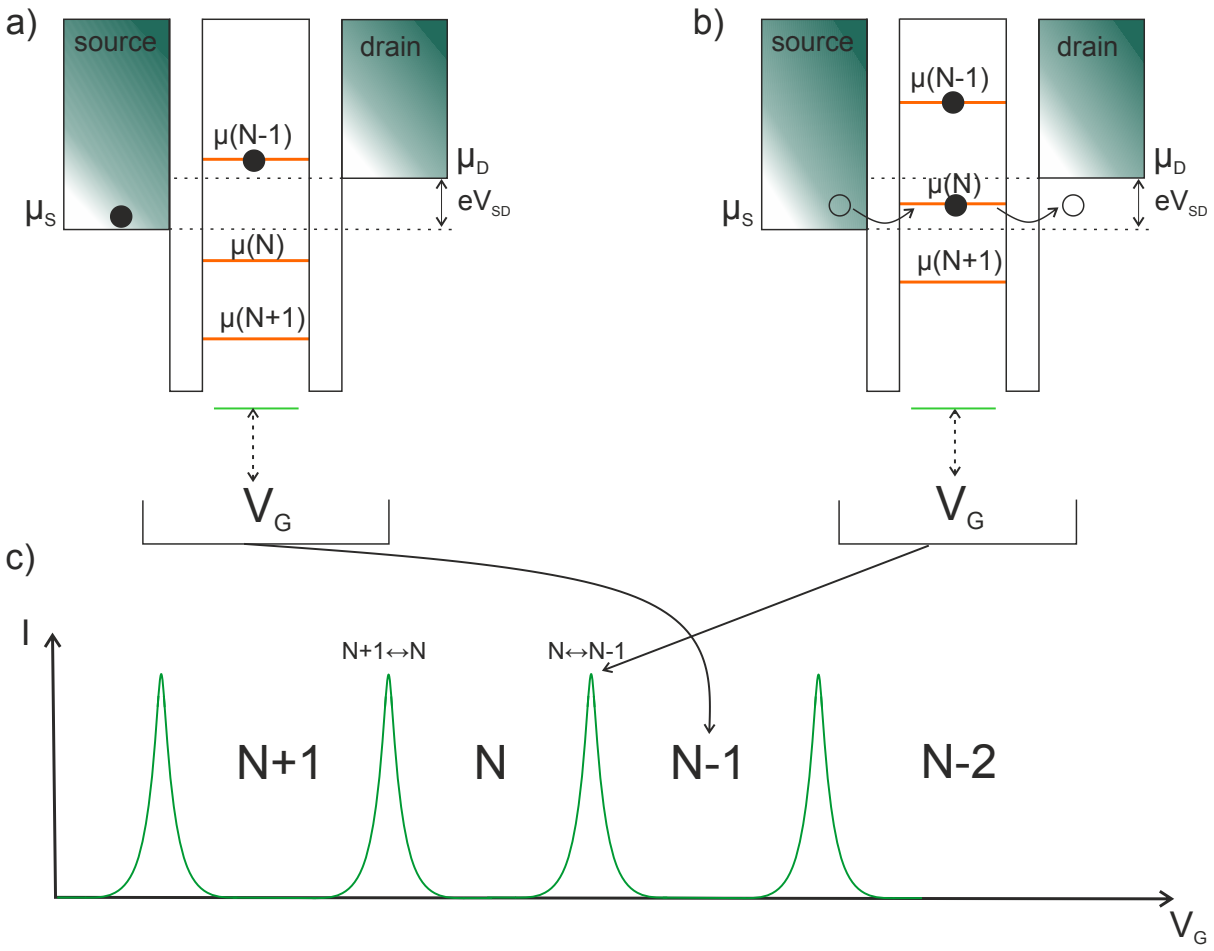

Figure 3.3: Schematics of the electrochemical potential levels of a QD in the sequential single-level tunnelling process regime. Occupied levels are indicated with solid black circles. (a) Case when no electrochemical potential in the dot falls within the bias window eV_{SD}. The number of holes occupying the QD is N-1. (b) After changing the gate voltage V_G, the $\mu(N)$ can be positioned in the bias window and the sequential single-hole tunnelling can take place. (c) Cartoon of the current through the QD as a function of V_G.

Usually, the current or the differential conductance is measured while sweeping the bias voltage for a series of different values of the gate voltage. Like this a stability diagram with characteristic shapes called Coulomb diamonds is obtained. Such a measurement is shown schematically in Figure 3.4 (b). In each diamond the current is equal to zero and the number of carriers is constant. The height of the diamonds is equal to the addition energy. From such a stability diagram also the energy of the excited states can be directly read out. If the state in a QD is strongly coupled to the contacts, higher-order transport processes where the transferred charge goes from the initial to the final state via a virtual state, become apparent in the Coulomb blocked region. These processes are called cotunnelling processes and they give rise to current inside the Coulomb diamond [63].

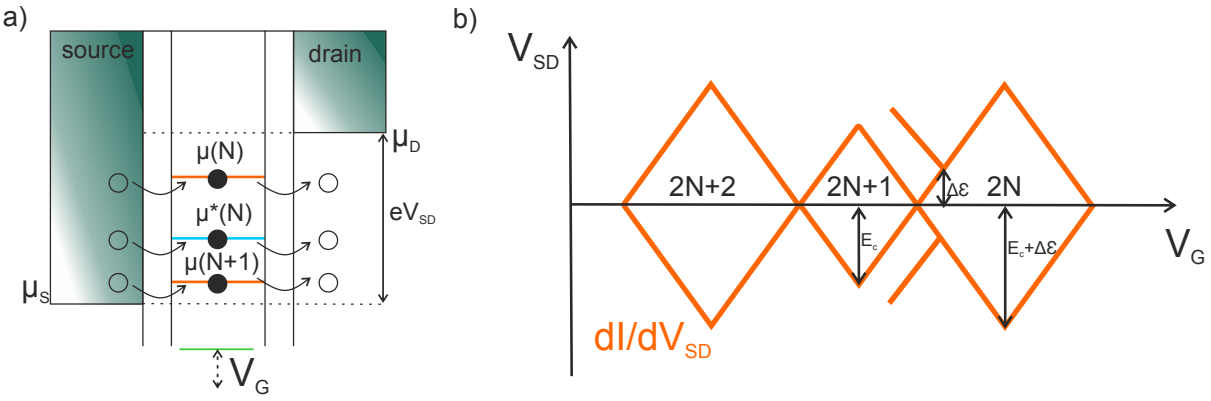

Figure 3.4: (a) Schematics of the electrochemical potential levels of a QD in the sequential multi-level tunnelling process regime. The level in blue corresponds to a transition involving an excited state. (b) Cartoon of a conductance measurement with V_{SD} and V_G swept. The edges of the diamond shaped regions correspond to the onset of current and N denotes number of holes in the QD. An additional line represents an excited state.

Coherent and Kondo regime

When $V_{\mathrm{SD}} \ll h\Gamma \ll \Delta\varepsilon$, tunnelling is coherent, since under this condition there is no scattering during the process and thus the phase of the wave function at each point in space is continuous in time. Finally, when $V_{\mathrm{SD}}, k_B T \ll T_K$, the Kondo regime occurs, where second-order charge transitions other than cotunnelling start to play a role in the transport processes. When the number of charges confined in a QD is odd, one charge stays unpaired (in case of typical even-odd filling of the (spin) states) and the localized state has a net magnetic moment. This manifests as a zero-bias resonance inside the Coulomb diamond for odd number of confined charges [64, 65].

3.2 Transport in coupled quantum dots

The next logical step after studying individual QDs is to study systems with more than one dot. Two or more individual QDs can be mutually coupled if they are fabricated close to each other. Usually two contributions to the coupling have to be considered: capacitive and tunnel coupling. The former arises from the electrostatic interaction between the charges of neighbouring dots, which leads to a mutual influence on the energy spectra. The latter may occur between neighbouring QDs leading to a splitting of resonant energy levels. Two coupled QDs are referred to as double quantum dots (DQDs).

Coupled QDs can be as well modelled as a network of tunnel resistors and capacitors. Figure 3.5 shows schematically different arrangements of two QDs. They may be either connected in series (Figure 3.5 (a)) or in parallel (Figure 3.5 (b) and (c)), between a source and a drain contact. Gate electrodes 1 and

2 allow us to control the number of charges in the two QDs. Due to the fact that all gates and dots are in close proximity to each other, the cross-capacitances cannot be neglected. That means that gate 1 will also act on dot 2, and gate 2 will tune dot 1.

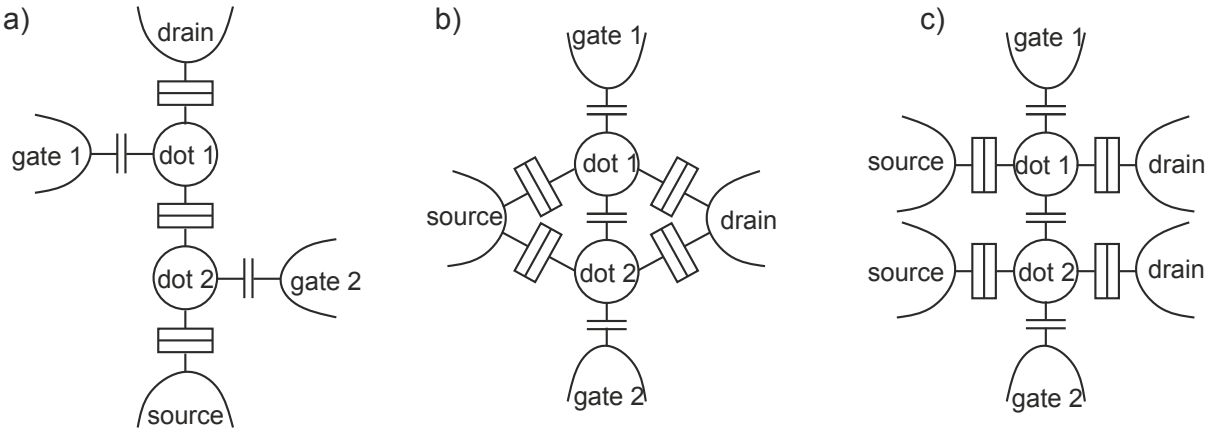

Figure 3.5: Schematic arrangement of typical DQD structures. (a) Two dots connected in series and placed between a source and a drain contact. (b) Two dots connected in parallel between the same pair of source and drain contacts. (c) Two dots connected in parallel with each dot having a separate pair of source and drain contacts.

In order to obtain the total energy of the DQD system within the capacitance model, we add to the total electrostatic energy of the two QDs the quantization energies of the levels in the two dots and neglect the tunnel coupling between them [61]. The total energy of the coupled system is the sum of the energies of the individual dots plus an electrostatic coupling energy:

$$\begin{aligned} U(K,N) = & \underbrace{\sum_{n=1}^{K} \varepsilon_n^{(1)} + \frac{e^2K^2}{2C_{1\sum}} - eK\sum_{j=2}^{n}\alpha_{1j}V_j}_{\text{QD1}} \\ & + \underbrace{\sum_{n=1}^{N} \varepsilon_n^{(2)} + \frac{e^2N^2}{2C_{2\sum}} - eN\sum_{j=2}^{n}\alpha_{2j}V_j}_{\text{QD2}} + \underbrace{\frac{e^2KN}{C_M}}_{\text{interaction}}, \end{aligned} \tag{3.10}$$

where K and N are the number of charges in the QD1 and the QD2, respectively, α_{1j}, α_{2j} are the lever arms of the gates which transform the addition energy to gate voltages, C_M is the mutual capacitance and

$$C_{\sum 1} = C_{11}\left(1 - \frac{C_{21}C_{12}}{C_{11}C_{22}}\right)$$
$$C_{\sum 2} = C_{22}\left(1 - \frac{C_{21}C_{12}}{C_{11}C_{22}}\right)$$

Comparing with the total energy of a single QD in 3.6, we see that the total energy of the coupled

system is the sum of the energies of the individual dots plus an electrostatic coupling energy (interaction) containing the product of numbers of charges on each individual dot and the mutual capacitance C_M. The electrochemical potential for QD1 with *K* charges, when QD2 is occupied with *N* charges, is given by:

$$\mu_K^{(1)}(N) = \varepsilon_K^{(1)} + \frac{e^2}{C_{1\sum}}(K - \frac{1}{2}) + |e|\sum_{j=2}^{n}\alpha_{1j}V_j + \frac{e^2}{C_M}N \tag{3.11}$$

That means that if we do tunnelling spectroscopy of the $\mu_{N_1}^{(1)}$, the electrochemical potentials of the QD1 depend on the charge state of QD2. An additional electron in QD2 shifts the whole ladder of electrochemical potentials in QD1 up in energy. In turn, the same is true for the spectrum of QD2.

The charge stability diagram, the plot of the current through the DQD versus two gate voltages, is shown in Figure 3.6, for three different interdot couplings. In case of very weak interdot coupling ($C_M \approx$0; Figure 3.6 (a)), we have two independent QDs and each can be tuned with its gate electrode individually. Vertical (horizontal) lines are the Coulomb peaks of QD1(2). In a more realistic regime, where one would actually operate a DQD system, $0 < C_m < C_{1(2)}$, we see two main differences in the stability diagram. First, the Coulomb peaks are slanted, with the slopes given by the ratios of the lever arms of the two gates acting on the two dots. Their finite slope is due to the fact that V_G2(1) also couples to QD1(2) and continuously moves the electrochemical potentials. Second, every time when an additional charge is added to the QD1, the shift in the electrochemical potential of QD2 causes the discontinuities in the Coulomb peaks of QD2. This can be easily understood if we think that an added charge is acting like an additional gate which is shifting our resonance condition for transport. In order to have current flowing through the device, we have to readjust the gate voltage.

These slanted Coulomb peaks, together with the breaks, form a recognizable DQD transport pattern: a honeycomb. In each hexagon the number of charges is fixed ((K, N) notations in Figure 3.6). The six corners of each hexagon are called triple points, because at these points, three charge states coexist (black points in Figure 3.6 (a) and (b)). Triple points are particularly important for QDs connected in series because these are the only points in parameter space where a charge can be transported from source to drain resonantly.

Finally, for a very large coupling a DQD behaves as a single QD, which can be tuned with two gates.

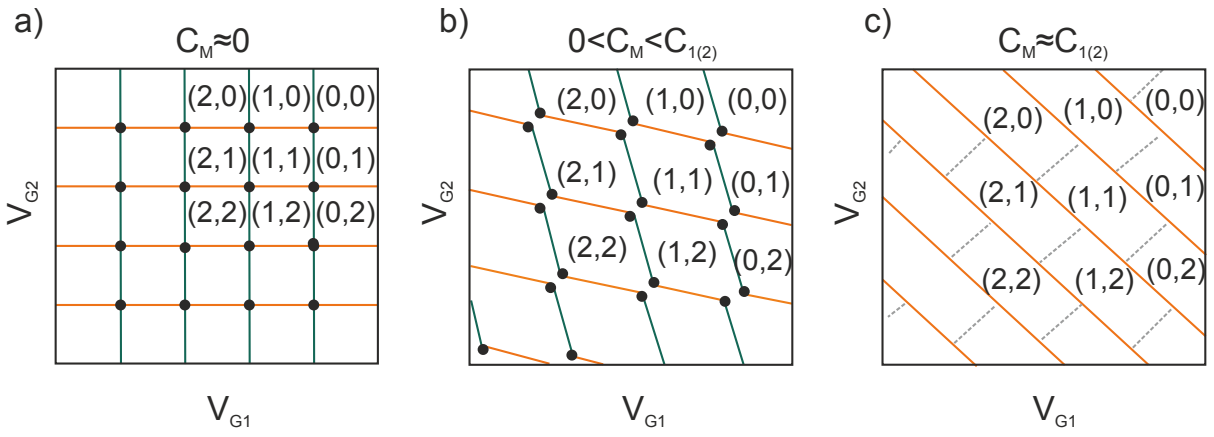

Figure 3.6: Charge stability diagram of a DQD with three different interdot couplings C_M for $V_{SD} \approx 0$. (K, N) denotes the hole occupation in the two dots. (a) Uncoupled dots (b) Intermediate coupling regime. (c) Strong coupling regime.

4 Fabrication and measurement techniques

There are two main approaches in fabrication of QD devices suitable for transport measurements: (i) a top-down approach and (ii) a bottom-up approach. The former is typically used in fabrication of devices in two dimensional electron or hole gases, where the QD is created by depleting locally the gas with metallic electrodes. In the case of self-assembled nanostructures, a bottom-up approach is used.

4.1 Fabrication of single-hole transistors

The first devices which I fabricated were single-hole transistors (SHTs), based on dome islands (Figure 4.1 (a)), with a goal to find a good recipe for more complicated devices.

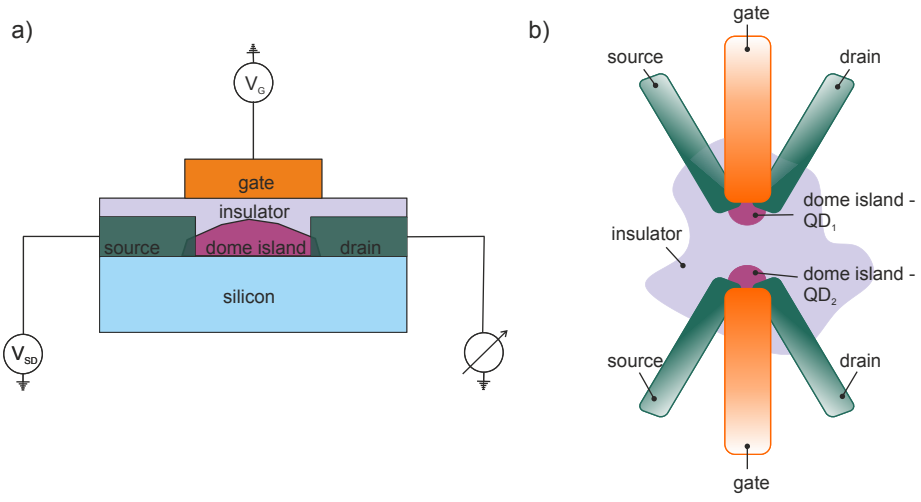

Figure 4.1: (a) Scheme of an SHT based on a dome island. (b) Scheme of a coupled quantum dots device with two nearby dome islands.

The fabrication process greatly depends on the available equipment. For the initial set of devices, a *Leo Supra 35* electron beam lithography system was used. The system had certain limitations when

it came to writing speed and stage control. That resulted in a quite tedious fabrication process which I will refer to as *random approach*. The second set of devices were fabricated with the new electron beam lithography system *E-line*. This simplified the whole fabrication process, which I will call *direct approach*.

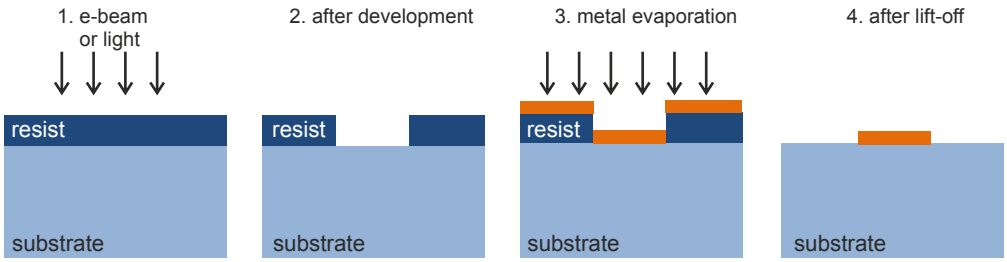

Figure 4.2: Fabrication processes for defining metallic electrodes: spin coating and lithography, development, metal deposition and lift-off.

4.1.1 Fabrication of single-hole transistors out of dome islands with the random approach

The idea behind this approach was to contact stochastically a dome island with the two electrodes. For that, several fabrication steps are needed, which I will briefly describe here. Typical device design and SEM images are shown in Figure 4.3 (a)-(e). All relevant fabrication parameters are given in Appendix A, Table A.1.

- Cutting the samples and defining the write fields

  The nanostructures are grown on a 4" intrinsic Si(001) wafer, which is cut in smaller pieces of a few cm^2 with a diamond saw. The first step is to define 4 write fields, each of them with 16 electrodes that shrink until they frame an area of 250x250 $\mu\mathrm{m}^2$ with a set of alignment crosses (Figure 4.3 (a)). This step is done with optical lithography (*Karl Suess Mask Aligner MJB3*). Usually, before the development a rinse in chlorobenzene is performed, which results in the formation of a resist profile called undercut, which makes the lift-off process easier. The development step is followed by metal deposition (see Figure 4.2). For this step typically a Cr/Au 10/65 nm combination is used. After lift-off, individual 5 mm x 5 mm samples are cut, again with the diamond saw.

- Defining the source and the drain electrodes

  In the first electron beam lithography step, a big number of source and drain contacts is defined in each of the 4 write fields (Figure 4.3 (b)). The gap between the source and the drain electrode is maximally 80 nm, otherwise the probability that a dome island would be stochastically contacted approaches zero. To ensure a clean gap, a double layer of PMMA (Poly(methyl methacrylate))

electron beam lithography resist is used. In this bilayer technique the PMMA on top is less sensitive than the PMMA on the bottom. As a consequence, it is less developed than the bottom layer, which results in an undercut. Additionally, different doses for beam exposure are used, which results in different sizes of gaps, making the design robust to beam current fluctuations.

- Metal deposition and lift-off

  Before the deposition, a 10 sec BOE (buffered oxide etch) dip is performed. Initially, Ti/Au 10/25 contacts were used, but they were giving extremely low yield of working devices, presumably due to the small work function of this metal combination. Pt, due to its large work function, has proven to be much better, giving good contacts and a yield of almost 100$\%$.

- Imaging and drawing a complete design

  After the lift-off, the sample is imaged with a scanning electron microscope (SEM), in order to check which source-drain pairs contacted a dome island (Figure 4.3 (d)). The design for the gate electrode and the electrodes connecting the source and drain to the larger connections made by optical lithography is drawn in the dedicated software accordingly (Figure 4.3 (e)).

- Defining the electrodes connecting the source and drain to the larger connections which were previously made by optical lithography

- metal deposition and lift-off

- Defining the gate electrode

- Metal deposition and lift-off

  The metal deposition is preceded by an atomic layer deposition (ALD) of few nanometres (6-8) of an oxide, normally HfO_2 (also called hafnia) or Al_2O_3 (also called alumina). Here a top or a side gate electrode is used (Figure 4.3 (f)).

The random approach is very limiting when it comes to devices which have more than three electrodes or are built out of more than one nanostructure. Besides statistics, another big problem was the alignment precision between two sequential steps in the fabrication process. Alignment before each e-beam exposure was done manually and that drastically reduced the yield of devices suitable for measurement.

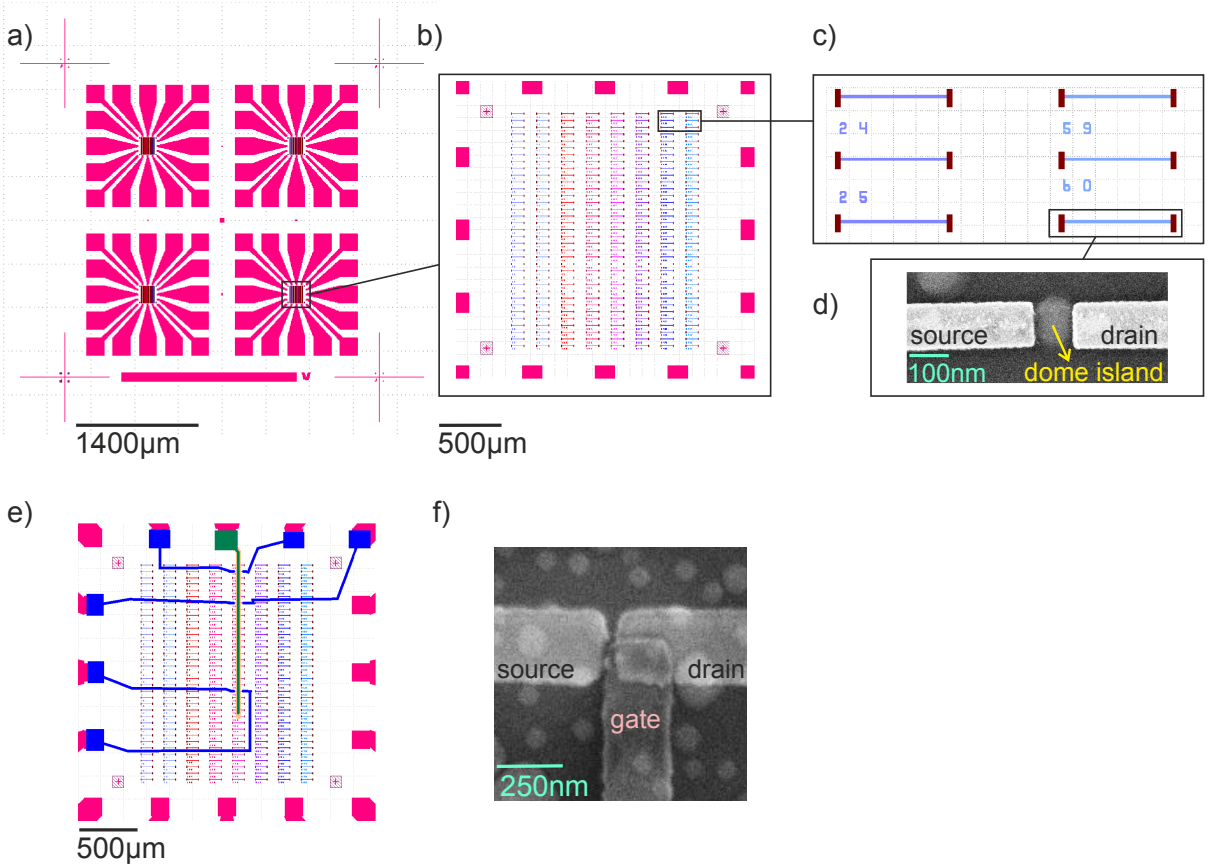

Figure 4.3: Device design and SEM images of an SHT fabricated with the random approach. (a) Alignment crosses and 4 times 16 electrodes which frame 4 write fields. (b) Zoom into one of the four write fields. The pairs of source and drain electrodes to be defined with the e-beam lithography are visible. Different colours are denoting different doses for beam exposure which lead to different sizes of gaps, making the design robust to beam current fluctuations. (c) Further zoom into the pairs of electrodes. Each of the pairs is labelled with a number used later for distinguishing them. (d) SEM image of a source-drain pair with a dome island located in-between. (e) Picture of the completed design of a write field showing the source and drain connections (blue) to the electrodes and the gate (green). (f) SEM image of a completed device, showing the source and drain electrodes and the gate electrode on top of them. An island can be seen under the gate. The thin hafnia layer is not visible here.

4.1.2 Fabrication of single-hole transistors out of dome islands with direct approach

When we switched to the *E-line* electron beam lithography system, equipped with a laser interferometer stage, a new pattern generator and a new software, the whole fabrication process got simplified. There was no need any more for an optical lithography step, since the beam currents could be chosen much higher and even big structures could be written with e-beam lithography. The laser interferometer stage enabled an alignment precision of 10 nm, the crucial improvement which made all the fabrication

processes described in this thesis, concerning the e-beam lithography, much more reproducible.

An additional key difference here is that after SEM imaging in the *E-line* system, the SEM images are automatically incorporated and aligned in a dedicated *E-line* software. Then the desired design for the e-beam lithography is directly drawn. The rest of the fabrication process is similar as that of section 4.1.1 and it is described in detail in Table A.2.

4.1.3 Single-hole transistor - magnetotransport spectroscopy

For checking which combination of metals for source, drain and gate electrodes and which oxide leads to good devices and in order to optimize the whole fabrication recipe, a substantial number of three terminal devices was fabricated and characterized at 4 K. On few selected devices detailed measurements at lower temperature (250 mK) were performed.

A characteristic conductance plot of one such device is shown in Figure 4.4 (a). In another device, the strong coupling regime between a QD and the leads could be achieved with Pt contacts. This allowed us to measure the Kondo effect [64] (Figure 4.4 (b)). We performed spectroscopy measurements for three different directions of the external magnetic field: perpendicular (labelled as B_x) and parallel to the growth plane (labelled as B_y and B_z). The extracted values g-factors of g_x=1.8, g_y=1.1, g_z=1 (Figures 4.4 (c) and (d)) are in agreement with the already shown g-factor anisotropy in SiGe dome islands [66].

4.2 Fabrication of coupled quantum dots out of dome islands

After establishing a good recipe for the reproducible fabrication of SHTs, we moved towards the fabrication of capacitively coupled individual QDs. The goal was to use one of the dots as a charge sensor (see Section 5.1) for the second one.

The device consists of two capacitively QDs, each contacted with source, drain and side gate electrodes and few nm of an insulator between source/drain electrodes and the gate electrode (Figure 4.1 (b)). Each QD with its electrodes, when observed isolated, is simply behaving as an SHT. The fabrication process can as well be split in two different approaches, a random and a direct. As before, the latter has a significant advantage, but for completeness (and to demonstrate the fabrication difficulties) the former will as well be described.

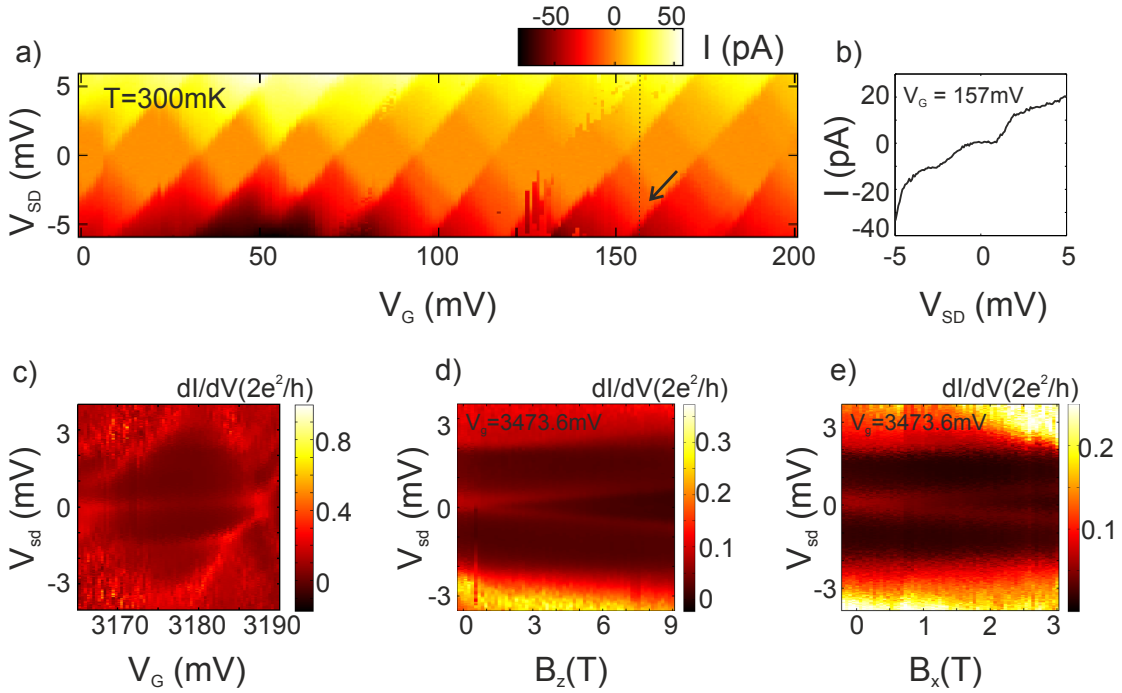

Figure 4.4: (a) Typical current measurement of a Ge dome island contacted with Ti/Au leads. The current through the device is measured while sweeping the bias voltage V_{SD} and stepping the gate voltage V_G. Steps in the current (black arrow) indicate that there is a transport channel through the excited states as well. The many-holes regime is evident from the same size of diamonds, a consequence of charge screening and smaller energy difference between consecutive states. (b) Current versus bias voltage line trace for a gate voltage value indicated with the dashed vertical line in (a). A step in the current value due to the transport through an excited state can be seen. (c) Part of a diamond plot with a zero bias peak inside a diamond, arising from the Kondo effect, measured for another device. The differential conductance is measured while sweeping the bias voltage V_{SD} and stepping the gate voltage V_G. (d) Splitting of the Kondo peak for a magnetic field parallel to the growth plane. The differential conductance is measured for a fixed gate voltage while sweeping the bias voltage V_{SD} and stepping the magnetic field in the direction parallel to the growth plane. (e) Splitting of the Kondo peak for a magnetic field perpendicular to the growth plane. The differential conductance is measured for a fixed gate voltage while sweeping the bias voltage V_{SD} and stepping the magnetic field in the direction perpendicular to the growth plane.

4.2.1 Fabrication of coupled quantum dots out of dome islands/superdomes with the random approach

Completely random approach

In contrast to the random approach described in Section 4.1.1, the goal here was to contact stochastically not one, but two domes. Since the two SHTs should be within few tens of nm from each other and not screened by the electrodes, a "V" shape for the source and the drain electrodes was chosen (Figure 4.5 (a)). Pairs of double "V" shapes were written on the four write fields, together with the additional set

of four fine alignment markers around them. These markers would be later used to position the gate electrode precisely. Besides rather low chances of randomly contacting two nearby domes, imaging of the completed devices revealed a big problem in the alignment of the electrodes. Since the alignment was done manually (see Figure 4.5 (b)), the gate electrodes were often misplaced.

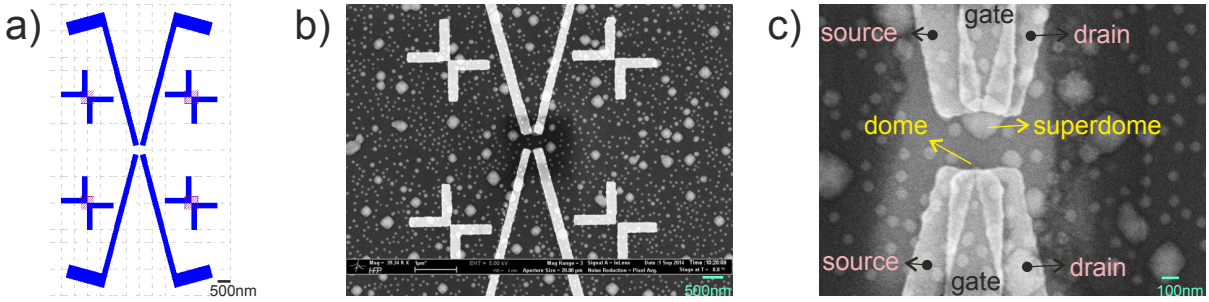

Figure 4.5: Device design and SEM images of a charge sensor with domes, random approach. (a) Picture showing the design of one "double V" unit with four alignment markers. Such a unit is repeatedly written within one write field. (b) SEM image of such "double V" unit with randomly contacted dome/superdome. Such high resolution images with all four fine alignment crosses are incorporated in the design software. (c) SEM image of a completed device with two SHTs, one with a dome (lower part), and the second with a superdome (upper part; to be used as a charge sensor for the dome device). To avoid screening effects side gates are fabricated (placed on top of the source and the drain pairs). The lighter area on the SEM image shows the hafnia layer.

Semirandom approach

In order to increase the yield of fabricated devices, a "semirandom" approach was tested. Conveniently, superdomes are bigger in size and they could be contacted directly even with the outdated e-beam system. Instead of writing pairs of "double V"-s, only single "V"-s were written, aiming at randomly contacting a dome island. In a second step a superdome was contacted deterministically (see Figure 4.6). Sometimes also a floating gate, which should act as an interdot antenna, was added, in order to enhance the capacitive coupling between the two QDs.

Obviously, random and semirandom ways of fabrication have many disadvantages. One has to be lucky to catch two domes between source and drain electrodes, with no other dome islands in-between, or just one but exactly where there is a superdome nearby. Often the placement of the electrodes is far from perfect, due to the manual image incorporation and alignment errors. However, several things have been learnt from the fabrication on such devices. As expected, when either the QD dome island or the QD sensor are covered with the gate electrode there is a screening effect and the sensor is decoupled from the QD to be sensed. To overcome this, side gates or partial side gates can be fabricated (Figure 4.5 (c)), which have experimentally proven to tune the QD as good as the top gates, when placed within

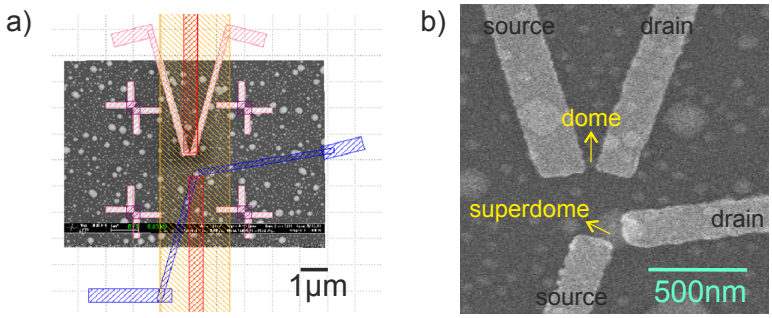

Figure 4.6: Device design and an SEM image of a charge sensor with domes in the semirandom approach. (a) Picture showing the SEM image incorporated in the design software. A contacted dome island together with four fine alignment crosses (light pink) can be distinguished. The nearby superdome would act as a charge sensor. It is contacted deterministically in a subsequent step (blue). The hafnia layer is shown in yellow, gates in red . (b) SEM image of a partially finished device; in this device the dome is randomly contacted with source and drain electrodes and the superdome is contacted deterministically.

few nm from the island. Besides, it could not be demonstrated that a floating gate helps in the capacitive coupling between the two QDs.

4.2.2 Fabrication of coupled quantum dots out of dome islands with direct approach

As discussed, the direct approach reduces the number of fabrication steps and at the same time allows us not to depend on luck, but to choose a pair of islands on our own and define the electrodes with a great precision. The steps are the same as for fabricating an SHT (described in Section 4.1.2).

In Figure 4.7 SEM images of devices fabricated with the direct approach after different steps are shown.

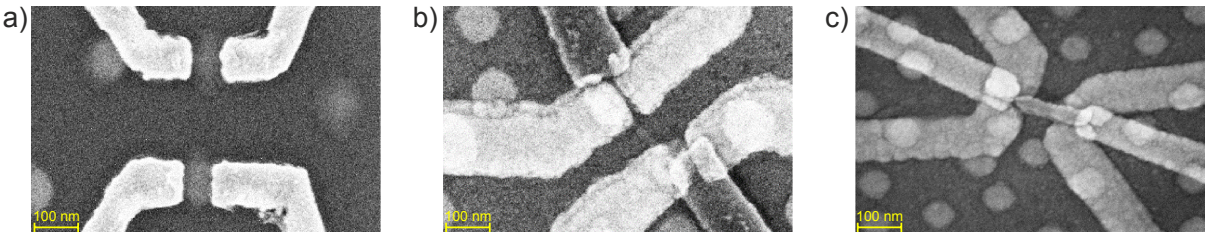

Figure 4.7: SEM images of charge sensing devices with two nearby dome islands after different steps of fabrication. (a) Two nearby dome islands with source and drain electrodes. (b) Two nearby dome islands with source, drain and side-gate electrodes. (c) Two nearby dome islands with source, drain, side-gate electrodes and a floating gate.

Although the fabrication of these devices does not seem much more complicated than the fabrication of

a conventional SHT, it has proven to be challenging having both individual SHTs working with a similar quality. In parallel with fabrication of coupled QDs based on the dome islands, we started to work on devices based on HWs. HWs devices, described in the next Chapter, are easier to fabricate and show more reproducible transport data.

4.3 Measurement techniques

4.3.1 Low-temperature setups

As already mentioned in the introductory part of this thesis, in order to study quantum phenomena, cryogenic temperatures are needed. The experiments described in this thesis were performed in different cryostats. For initial characterisations a home-made 4 K dip-stick was used, where the sample was cooled down to the temperature of liquid ^{4}He simply by immersion. A temperature of 1.2 K could be obtained by pumping on ^{4}He. Even lower temperature, 250 mK, could be reached with a ^{3}He based cryostat by pumping on ^{3}He. We used an Oxford Instruments *HelioxVL*, equipped with a vector magnet of 9 T in the z-direction and 3 T in the x-direction. Finally, temperatures of tens of mK could be reached in a dilution refrigerator, a system which uses the spontaneous phase separation of a mixture of ^{4}He and ^{3}He. The experiments described in Chapter 6 were carried out in a *CF-CS81-1400-MAG* dilution refrigerator from Leiden Cryogenics, and the experiments described in Chapter 7 in a *LD-250 EO* dilution refrigerator from BlueFors Cryogenics. Both fridges are cryogen-free and are equipped with a 9-3 vector magnet.

The fully fabricated sample has to be electrically connected with the measurement setup. Initially we were using commercial chip-carriers, which could be attached to the cold finger of a 4 K dip-stick or a ^{3}He cryostat. The sample was glued on a chip carrier and the electrodes defined on the sample were connected with the chip carrier with thin Al wires (this was done with a wedge bonder). The lack of a common ground plane caused our devices to explode very easily. Soon we switched to home designed DC printed circuit boards (PCBs), including also a ground plane. This protected the bonded sample from the electrostatic discharge. Additionally, all our PCBs had RC filters, necessary for reducing the high frequency noise. The PCB was connected to the measurement setup via a Micro-D connector. The first PCBs were developed at JKU Linz by Raimund Kirchschlager and Josip Kukučka and improved at IST Austria by Josip Kukučka with the help of Thomas Adletzberger.

For the DC electronic measurements we used a battery-powered low-noise electronics developed at the TU Delft. This electronics was optically isolated from the measurement computer and used a ground separate from the ground of the power grid in order to minimize the noise level. All DC lines were

filtered at two stages: once at room temperature (pi filters in the TU Delft electronics) and once at low temperature (RC filters on the PCBs). Additionally, both dilution fridges had one more set of LC filters on the mixing chamber.

For resolving less pronounced features, we used a lock-in amplifier (Stanford Research Systems *SR830* or Zurich Instruments *UHFLI*). To overcome the problem of a too low bandwidth to measure dynamic properties of a quantum system, we switched to a radio-frequency (RF) reflectometry readout.

4.3.2 Reflectometry

RF reflectometry is a readout technique where an RF signal is sent to a resonant circuit composed of the QD device and a matching circuit and the amplitude or phase of the reflected signal is measured [67–70]. If in a QD device the change of some external parameter (for instance a gate voltage) leads to a change in its active resistance or reactive load (typically capacitive), the resonance of the circuit is affected, resulting in a change of magnitude and phase of the reflected signal. The ratio between the reflected ($u_r(t)$) and the incident signal ($u_i(t)$) is given by the reflection coefficient Γ:

$$u_r = \Gamma u_i. \tag{4.1}$$

Γ is defined as

$$\Gamma = \frac{Z - Z_0}{Z + Z_0}, \tag{4.2}$$

where Z_0 is the characteristic impedance of the RF line (50 Ω) and Z is the impedance of a resonant circuit (see figure 4.8). The modification of the device parameter will lead to a very significant change in Γ only if an impedance matching condition is achieved.

We can illustrate the importance of the impedance matching with a simple example. Our devices usually have impedances of hundreds of kΩ when they are not in the Coulomb blockade. Let us take $Z_1 = 500\,k\Omega$ when the device is not in the Coulomb blockade and $Z_2 = 10\,M\Omega$, when the device is in the Coulomb blockade and calculate the reflection coefficients from equation 4.2. From equation 4.2 we have

$$\begin{aligned} \Gamma_1 &= \frac{500k\Omega - 50\Omega}{500k\Omega + 50\Omega} \approx 1 \\ \Gamma_2 &= \frac{10M\Omega - 50\Omega}{10M\Omega + 50\Omega} \approx 1 \end{aligned} \tag{4.3}$$

With reflectometry we would like to detect changes in the device impedance:

$$\Delta u_r(t) = u_{r2}(t) - u_{r1}(t) = (\Gamma_2 - \Gamma_1)u_i(t), \tag{4.4}$$

but regardless of the change in the sample impedance, $\Delta u_r(t) \approx 0$. On the other hand, if the impedance of the device is transformed to values close to 50 Ω with the help of the matching circuit (see Figure 4.8), the difference between the reflection coefficients becomes sufficient to see and measure the difference between $u_{r1}(t)$ and $u_{r2}(t)$.

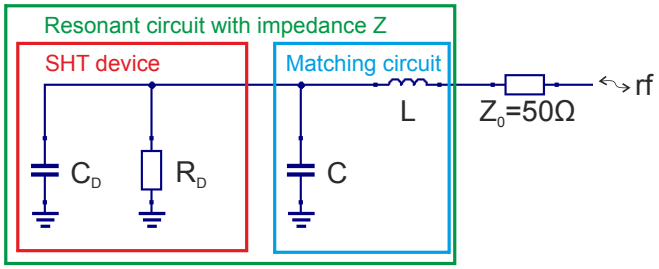

Figure 4.8: Basic scheme of ohmic reflectometry. The resonant circuit consists (green frame) of the SHT device (red frame) and the matching circuit (blue frame). The SHT is represented with a parallel combination of C_D and R_D. The matching circuit formed with an inductor L and a capacitance C is connected to the source contact.

In this measurement technique, an RF wave is constantly sent towards the device. Its power, hence, the amplitude, should be several times lower than the energy level spacing in the quantum dot, otherwise we lose the information due to the thermal broadening. The incoming signal is therefore attenuated on several stages of the dilution refrigerator (see Figure 6.2). The reflected signal is amplified first at the 3 K plate with a low-noise cryogenic amplifier, and then once more at room temperature.

For carrying out RF measurements, a different, RF PCB was used (see Figure 4.9(c)). The resonant circuit initially consisted of the SHT and a LC matching circuit. The capacitance was simply the parasitic capacitance C_{par}, which came from the various parts of the PCB and bonding wires. The inductance L was chosen in such a way that the typically large resistance (100-500 kΩ) of the SHT was transformed to nearly Z_0. In order to achieve a better matching condition and, consequently, higher sensitivity, we tested several different generations of RF PCBs, each of them having different components. Typically, each board had 4 different inductors, allowing measurements with four different matching circuits. Instead of having only an uncontrollable parasitic capacitance as a part of the matching circuit, for the experiments described in Chapter 7, variable capacitors (varactors) were added, in order to tune in-situ the matching condition [70]. Except RC filters for DC lines, the RF PCB was also incorporating the bias tees for the reflectometry and the fast gate lines. Component types and values are given in Appendix B.

There are several reasons why to choose reflectometry over current measurements. A reflectometry based system eliminates low-frequency disturbances, it is sensitive to both capacitive and resistive changes of a device (a current measurement is only sensitive to resistance changes) and does not require a current flow through the device. The latter allows a measurement of an isolated system, such as double-dot system, as well as measurements when the current signal is below the noise level.

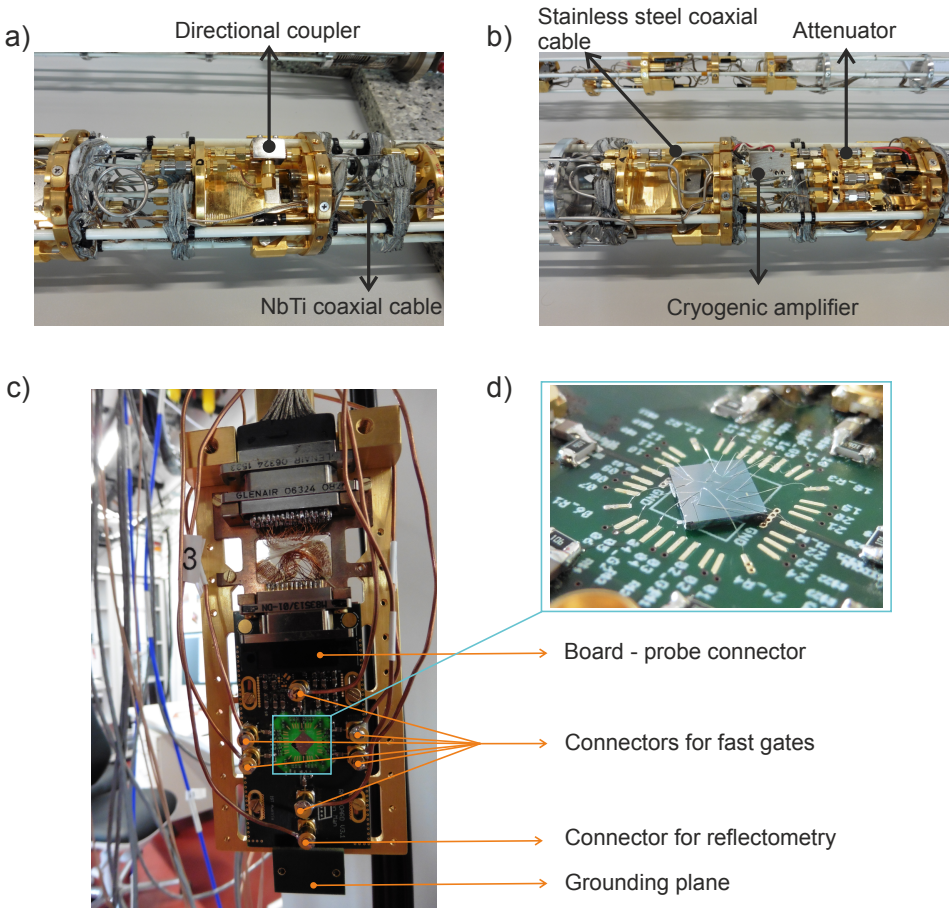

Figure 4.9: (a)-(b) Photos showing parts of the dilution refrigerator probe highlighting some of the elements (fast gates and reflectometry cables, direction coupler, attenuators and cryogenic amplifier). (c) Picture showing a PCB connected to the probe. Besides having a fast readout, for successful spin manipulation it is as well necessary to manipulate the system fast enough. For that purpose six fast gate lines for bringing the signal from an arbitrary wave generator *AWG5014C* to the gates of the device were installed. The DC lines are connected via a Micro-D connector, the six fast gates and the reflectometry matching circuit via SMP connectors. The probe has been wired by Thomas Adletzberger. (d) Picture showing a sample mounted on a PCB and bonded with Al bonding wires.

5 Charge sensing in Ge hut wires

5.1 Charge sensing techniques

Charge sensing is a method to detect changes in the number of QD charges with a nearby electrometer, a charge sensor, which needs to be very sensitive to its electrostatic environment. With this technique the dot can be probed non-invasively in the sense that no current needs to be sent through it. Additionally, a charge sensor is essential for spin-to-charge conversion, described in the next Chapter.

Typically, the charge sensor is fabricated in the vicinity of a QD device, and it is capacitively coupled to it. For achieving a good sensitivity, a charge sensor should show very abrupt change in current or conductance when varying the gate voltage. Most commonly used charge sensors are quantum point contacts (QPCs) [71] and SHTs [72] .

In case the charge sensor is a QPC, its conductance is very sensitive to the electrostatic environment when operated at the transition between two quantized conductance plateaus [73]. Similarly, if a QD is used as a charge sensor, its conductance is very sensitive at the flank of a Coulomb peak [72]. In both cases, a nearby charge displacement results in a large current/conductance change of the sensor. Whether to choose a QPC or an SHT as a charge sensor depends on the device. A QPC is easier to fabricate and it is less sensitive to the charge noise since the transition between quantized conductance plateaus has an almost constant slope over a wide range of electrostatic potential [73]. However, it can suffer from a back action since some current is always flowing through it. In contrast, an SHT can be completely switched off while a qubit operation is performed. To allow operation at high frequencies ($\approx$ 100 MHz) where the 1/f noise due to background charge motion is negligible, SETs as well as QPCs have been integrated in RF circuits [67, 74, 75].

The sensitivity of the detection scheme can be quantified by the charge-transfer signal $\Delta q/e$, where 1 e

Parts of this Chapter are published in Nano Letters **17**, 5706 - 5710 (2017)

is equivalent to the spacing between adjacent current peaks. In 2009, Morello et. al. [76] suggested to use a charge sensor, which is not only capacitively but also tunnel coupled to the spin qubit. In that case the QD hosting a qubit and the charge sensor are so close that the charge transfer signal is significantly increased. Additionally, the charge sensor can then as well act as a charge reservoir for the qubit, therefore simplifying the fabrication. In 2010 such a structure was implemented for a single-shot readout experiment of an electron spin in an individual donor in silicon. The observed high charge-transfer signals opened the path for fast and high-fidelity single-shot readout measurements of electron spins in Si donors [23, 77].

5.2 DC charge sensing in Ge hut wires

Inspired by the work on donors in Si, we realized a charge sensor for a QD formed in a Ge HW in a similar way. We chose HWs which are laying perpendicular to each other, in a T-like shape (Figure 5.1 (a), (b)), since measurements showed that, next to the expected electrostatic coupling between two hut wires, there is also a charge tunnel transfer between them, due to the leakage of the hole wave function through the SiGe substrate [78]. Even though the two HWs are not in the direct contact, there is a current of 10 nA flowing between them, due to the tunnelling of holes from one to another wire (Figure 5.1 (c)), already for an applied bias higher than $\pm$75 mV. Current through the Si substrate is not observed between two metal contacts at these bias voltages when no HWs are located in-between them.

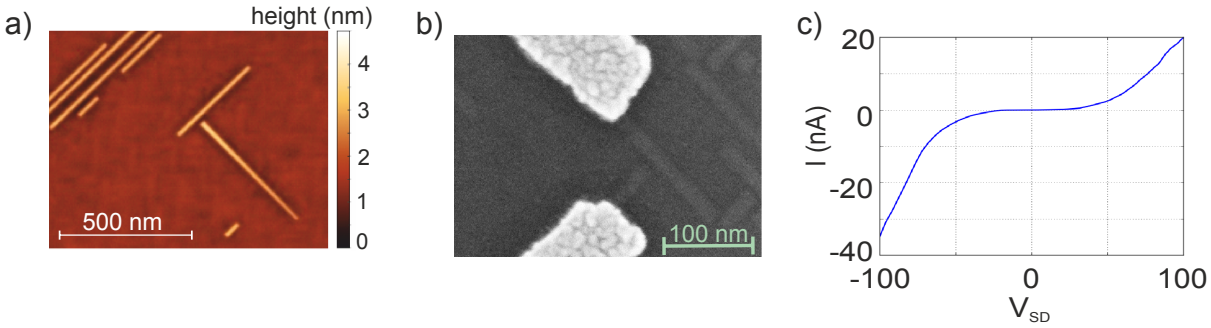

Figure 5.1: (a) Atomic force microscopy image showing a T-like Ge HW structure.(b) SEM micrograph of two non-touching perpendicular HWs, where each is contacted with only one electrode. (c) Current through the structure shown in (b) versus V_{SD}.

The devices used for the charge sensing experiment were fabricated out of the above mentioned T-like structures. The schematic of a device is shown in Figure 5.2 (a). The upper wire, contacted with source, drain and gate electrodes, acts as a single-hole transistor (SHT) and it is used both as a charge sensor and as a reservoir for holes. In the other wire, contacted only with a gate electrode, we create a QD that

can host a spin qubit. This QD is formed presumably between the gate and the end of the wire; its hole occupation is to be determined with the SHT sensor coupled to it. Usually, the gap between a source and a drain electrode is between 80 nm and 100 nm, while the perpendicular wire is covered fully with the gate except for a few tens of nm. The fabrication of the devices mainly follows the standard, direct approach procedure, as described in Section 4.1.2. For source and drain electrodes a combination of Pd and Al contacts were used (Pd 10 nm, Al 28 nm). All relevant parameters are given in Appendix A, Table A.3.

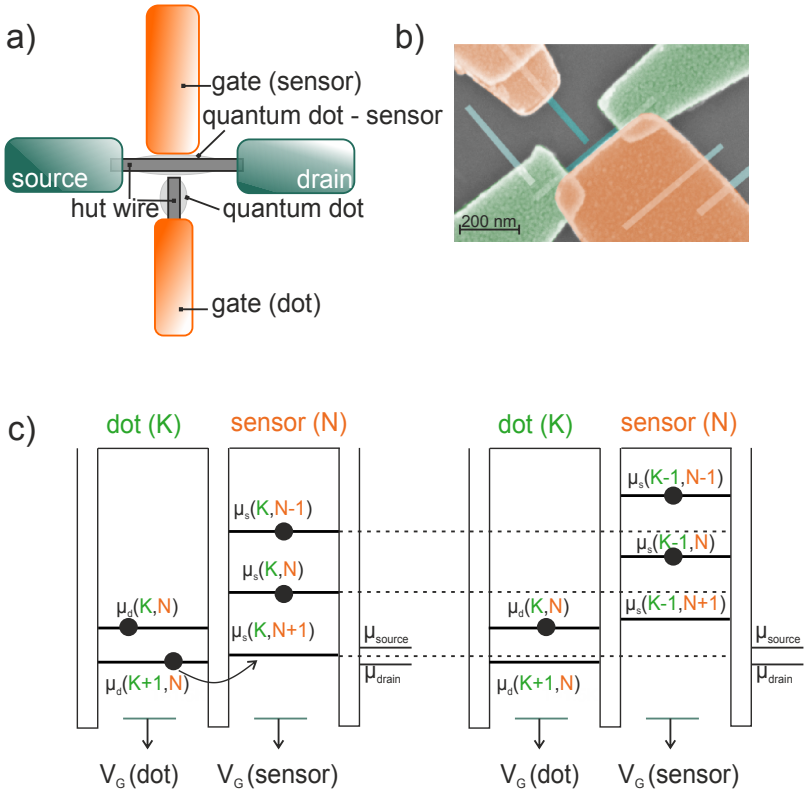

Figure 5.2: (a) Schematic of the charge sensor device used in this work. The two perpendicular HWs are shown in dark gray and the estimated position of the formed QDs in the wires in light gray. The source and drain contacts of the sensor - SHT - are shown in dark green and the gates of the sensor and the QD are shown in orange. (b) False color scanning electron micrograph of a device similar to those measured. (c) Schematic showing the ladder of electrochemical potentials of a capacitive and tunnel coupled QD-sensor system for the two cases of the dot occupancy, K and K+1.

In this configuration, the SHT sensor and the QD form a parallel DQD. As discussed in Section 3.2, for two coupled QDs, the electrochemical potential of one QD depends on the charge state of the other. This can be seen in Figure 5.2 (c), where the ladder of electrochemical potentials of the sensor is illustrated for two different QD charge configurations, K and K+1 [76]. Every time the condition for hole tunnelling from the QD to the SHT is satisfied, this tunnelling event will leave the dot with fewer holes, which will thus shift the electrochemical potentials of the SHT causing a break in the SHT Coulomb peak.

In order to return to the same SHT Coulomb peak the gate voltage of the sensor needs to be adapted. A stability diagram with characteristic shifts is shown in Figure 5.3 (b). The charge-transfer signal is very pronounced and equal to 30% (see Figure 5.3 (c)) and observable thus even at a temperature of 1.5 K.

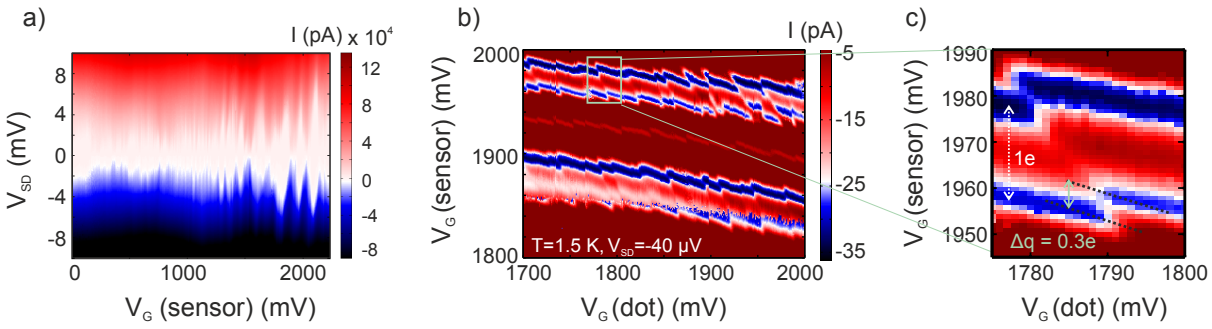

Figure 5.3: (a) Current versus V_{SD} and V_G diagram of the sensor dot, at a temperature of 1.5 K. (b) Stability diagram obtained by sweeping the gate of the QD versus the gate of the charge sensor, at V_{SD} = -40 μV. Every time when the number of holes in the dot changes, the Coulomb peak of the SHT breaks and shifts. (c) Zoom-in into the stability diagram, showing the discontinuity of a Coulomb peak. The dashed lines with the green (solid) double arrow are indicating the break in the Coulomb peak of the SHT while the white (dashed) double arrow indicates the Coulomb-peak spacing.

6 Hole tunnelling times in Ge hut wires

Single-shot readout of a single electron spin using the energy-selective readout technique described in the following paragraphs has been first demonstrated in gate defined GaAs/AlGaAs QDs [79]. Later on, a similar scheme was used in order to measure the spin relaxation times for electrons in Si [23]. Up to now, single-shot spin readout measurements for holes had not been realized. Presumably because the shorter relaxation times due to the strong spin-orbit interaction made the experiment challenging. To get around this obstacle, we integrated the charge sensor in a reflectometry setup. Such a setup allowed high bandwidths, which, due to the short hole tunnelling times, was a necessity for a successful spin measurement.

6.1 Spin-to-charge conversion and importance of single-shot measurements

To extract the spin relaxation time, the individual spin state has to be measured. Because of the tiny magnetic moment associated with the spin it is very challenging to measure it directly. However, by correlating the spin states to different charge states and subsequently measuring the charge of the dot, the spin state can be determined. This way, the measurement of a single spin is replaced by the measurement of a single charge. This can be done with the help of a charge sensor, which is a much easier task [79]. For measuring individual events a so-called single-shot measurement is necessary. The single-shot mode is important as it satisfies the DiVincenzo readout criterion and it allows the determination of the readout fidelity.

Single-shot readout of the spin state becomes possible when the relaxation time of the hole spin occurs on a longer time scale than needed to observe hole tunnelling. Hole tunnelling can be observed in

Parts of this Chapter are published in Nano Letters **17**, 5706 - 5710 (2017)

real time if the bandwidth of the charge detection exceeds the tunnel rate and when the signal from a single-hole charge tunnelling event exceeds the noise level, which is bandwidth dependent [80].

One way of achieving spin-to-charge conversion is by exploiting the energy difference of the spin states. In this energy-selective readout the spin levels are positioned around the electrochemical potential of the reservoir, such that a hole can tunnel off the dot from the spin excited state (ES), whereas tunnelling from the ground state (GS) is energetically forbidden. Therefore if the charge measurement shows that a hole tunnels off the dot, the state was the excited state, while if no hole tunnels the state was the ground state (Figure 6.1) [80].

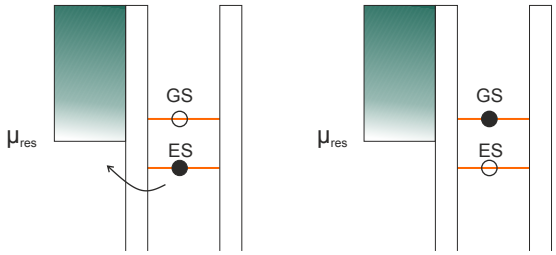

Figure 6.1: Electrochemical potential diagram depicting spin-to-charge conversion based on the energy-selective readout scheme. The GS corresponds to a spin-down, while the ES to a spin-up hole.

6.2 Hole tunnelling times in Ge hut wires

In order to investigate whether the charge sensor described in Chapter 5 is suitable for spin readout experiments, it was integrated into a resonant RF circuit and a reflectometry readout was performed. Additionally, the gates of the devices were connected to an arbitrary waveform generator (AWG), allowing fast gating. The resonant RF circuit consisted of a 2200 nH inductor and the parasitic capacitance to the ground. From the measured resonant frequency of 114.5 MHz, which for an LC resonant circuit is equal to

$$f = \frac{1}{2\pi\sqrt{LC}}, \tag{6.1}$$

a parasitic capacitance of ≈0.9 pF could be extracted. The scheme for the RF reflectometry and fast gating setup is shown in Figure 6.2, and the PCB details are given in Appendix B, Table B.1. Figure 6.3 (a) shows a stability diagram similar to that shown in Chapter 5, Figure 5.3. In contrast to the DC charge measurements shown in Figure 5.3, here the measured quantity is the amplitude of the reflected RF signal, integrated over approximately 10 ms, and the measurement was performed at a base temperature of about 30 mK.

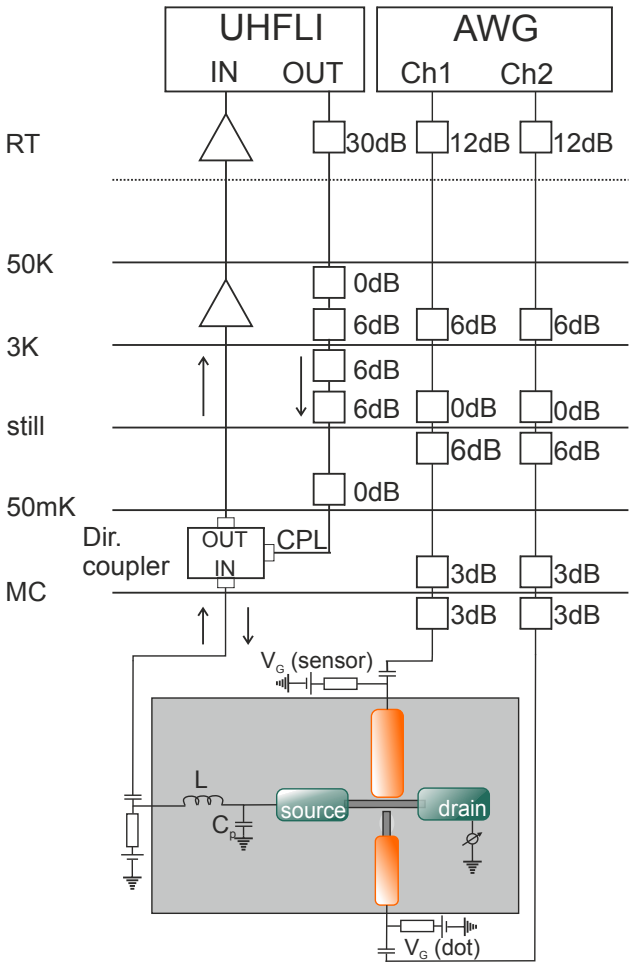

Figure 6.2: Simplified measurement circuit. The source of the charge sensor is connected to the matching circuit formed with an inductor L and the parasitic capacitance C_p to ground. The RF signal is sent to the sample from an ultra-high frequency *lock-in* (UHFLI) amplifier; it is attenuated at various dilution refrigerator stages. The reflected signal is amplified at two stages before the readout. Both gates of the device are connected to an AWG, which is used for applying short voltage pulses. The filtering of the DC lines is not shown.

6.2.1 Calibrating the pulsing sequence

In order to learn how our system behaves when applying the pulses on the gates, various introductory measurements were performed. First, a continuous pulsing sequence on the sensor gate was applied, while the gate voltage was swept. The waveform and duration of the pulse are shown in Figure 6.4. In order to eliminate the DC component of the applied pulse, which causes a warming up of the dilution fridge, the AWG output voltage was set in such a way that it had a mean value equal to zero.

Since the applied sequence is much faster than the gate sweep (tens of microseconds compared to hundreds of milliseconds), each Coulomb peak of the sensor appears as it was split in two and is shifted. In Figure 6.4 the blue peak is a Coulomb peak of the sensor when there is no sequence

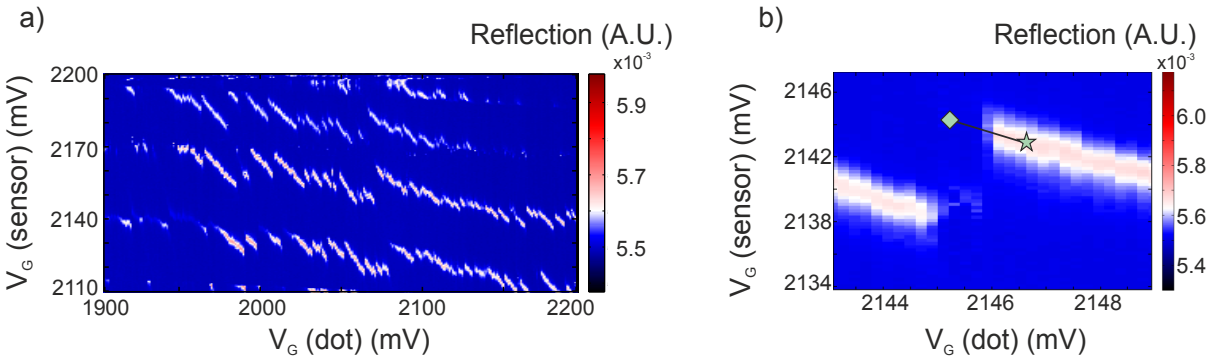

Figure 6.3: (a) Stability diagram, measured in reflection at a temperature of 30 mK. The power of the RF signal on the *lock-in* output was -35 dBm, the low-pass filter bandwidth 100 Hz and V_{SD} 80 μV. (b) Zoom-in of a stability diagram. The green rhombus (star) indicates the loading (unloading) position and the black line the direction of pulsing.

applied. The two green peaks are seen when the continuous, asymmetric sequence was applied on the sensor gate. The different distance of the green peaks from the blue one comes from the different pulse amplitudes and the difference in height from the different pulse durations. If a continuous pulsing sequence is applied in the positive direction, a peak will shift in the negative direction (effectively, the gate voltage has to be readjusted to compensate the pulse voltage).

In a second step, the diagonal pulsing was tested. Since both the gate of the dot and that of the sensor are influencing the ladder of electrochemical potentials of the SHT, the Coulomb peaks in the stability diagram are running under a certain angle. For the experiments it is important to apply pulses in the correct direction - along one Coulomb peak. This ensures that with the pulses we tune only the electrochemical potential of the QD, while the electrochemical potential of the SHT is constant. Additionally, without the diagonal pulsing one might easily end up in a different configuration of electrochemical potentials than expected.

To test this, we applied a simple, continuous pulse sequence to the gates of the device. The sequence consisted of two stages, the first one with an amplitude of 1000 mV, lasting 0.3 ms, and the second one with 0 mV, lasting 0.7 ms. First we applied the sequence to the sensor gate (Figure 6.5 (b)). When we compare it with the stability diagram when no sequence is applied (Figure 6.5 (a)), we can again see the split Coulomb peaks. The same occurs if we apply the same sequence to the QD gate (Figure 6.5 (c)). The diagonal pulsing is achieved by applying the sequence both on the dot and on the gate simultaneously, but with a different sign. The voltage pulse amplitude also needs to be adjusted; the factor in the voltage amplitude ratio for the sensor and the QD gate can be estimated from the slope of the Coulomb peak. Successful diagonal pulsing is shown in Figures 6.5 (d), (e). The applied amplitudes are -2500 mV to the QD gate and +3000 mV to the sensor gate, both for 0.3 ms. The amplitudes are on purpose chosen larger in order to see the result clearer. The ratio of 0.83 between the two amplitudes

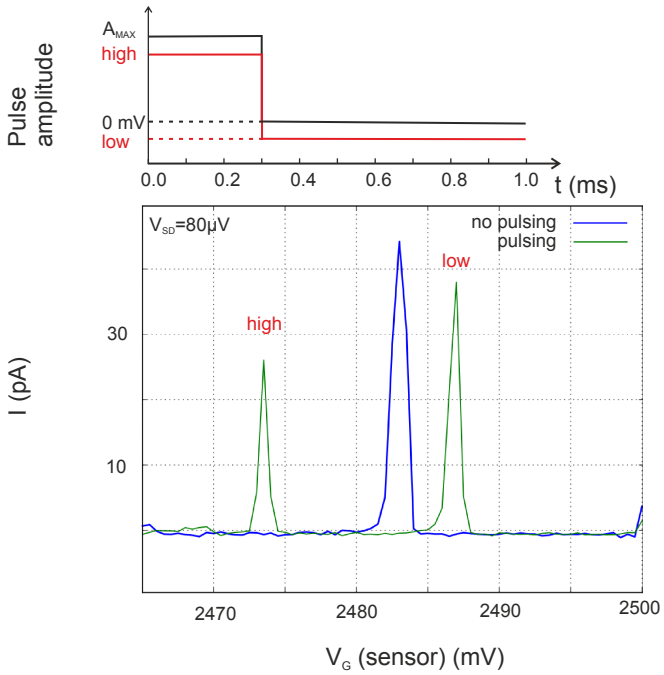

Figure 6.4: Current vs gate voltage showing a Coulomb peak of a charge sensor with (blue) and without (green) pulse sequence applied. The pulse sequence is schematically shown above the graph. To eliminate the DC component, the original pulse (black) was transformed (red) so that the pulse had a mean value equal to zero (dashed black line), resulting in a split and shifted peak.

is obtained from ΔV_G (QD)/ΔV_G (sensor), and can be read out from the reference stability diagram (Figure 6.5 (a)). Finally, Figure 6.5 (e) shows the diagonal pulsing in the other direction (for +2500 mV to the QD gate and -3000 mV to the sensor gate).

As a reminder, since we are dealing with holes, applying a pulse with the negative amplitude will leave the QD with more holes. Since the applied signal from the AWG is attenuated on the various stages of the dilution fridge, for these experiments an output voltage of 1000 mV corresponds to 4 mV arriving to the gates (see Figure 6.2, with the difference that here 30dB attenuators at the AWG outputs were used).

6.2.2 Real time detection of tunnelling events

For real time detection of tunnelling events between the QD and the sensor fast pulsing was used; a three-stage voltage pulse was applied to the gates of the device. The reference point for pulsing (0 mV) is at the position of the green star in Figure 6.3 (b). The way we were eliminating the DC component while calibrating the diagonal pulsing sequence could not be applied here, because it was moving our reference point. Here, after each three-stage voltage pulse we waited long enough before repeating it,

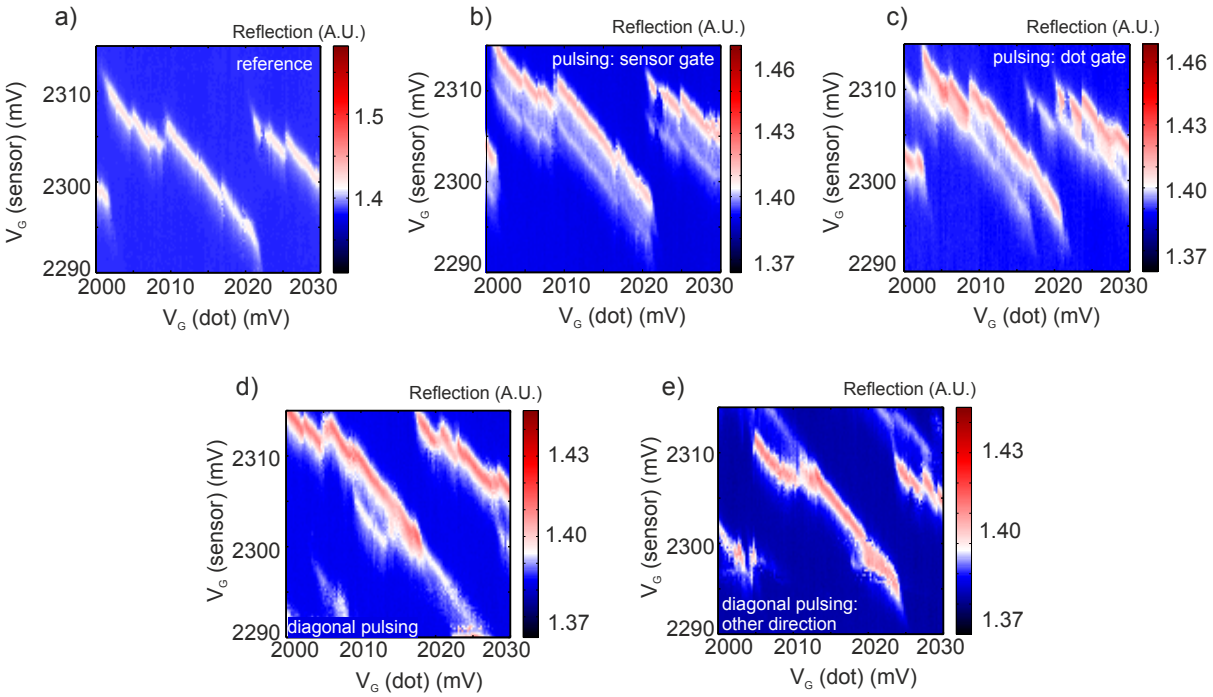

Figure 6.5: (a) Reference stability diagram without applying the pulsing sequence. (b) Stability diagram with the pulsing sequence applied to the sensor gate. (c) Stability diagram with the pulsing sequence applied to the QD gate. (d) Stability diagram when the sequence for the diagonal pulsing is applied. (e) Same as in (d), but with inverting the sings of the applied pulses. As a result the Coulomb peak moves in the opposite direction.

which resulted in the DC component tending to zero.

The pulse was applied along the upper part of the break in the Coulomb peak of the SHT shown in Figure 6.3 (b) (black solid line). Each stage of the pulse lasted for 500 μs. With the first stage of the pulse a hole is loaded into the dot (left part in Figure 6.6 (a); green rhombus in Figures 6.6 (b)), and with the last stage a hole is unloaded (right part in Figure 6.6 (a), green star in Figures 6.6 (b)); the reflection amplitude shows a minimum value when the hole is loaded into the QD and a maximum value when it is localized in the SHT. In between those two stages of pulses an additional one is applied aiming to align the electrochemical potentials of the QD (μ_{QD}) and the SHT (μ_{SHT}) (middle part in Figure 6.6 (a)). The voltage amplitude of this middle part of the pulse was varied in each of the 100 pulse sequences which were applied. The schematic of the applied pulse is shown in Figure 6.6 (b) and the reflected signal from the sensor in Figure 6.6 (c). When the electrochemical potentials between the QD and the SHT are aligned, continuous exchange of holes between the QD and the sensor can take place. This can be indeed observed in Figure 6.6 (c) for dot gate voltage levels between 2127μV and 2418 μV. The line trace shown in Figure 6.6 (c), taken at the position of the green dashed line in Figure 6.6 (b), shows indeed several tunnelling events during the align stage. The small and unequal peak heights of the tunnelling events are due to the limited bandwidth of the used setup, combined with different tunnel-in

and tunnel-out times. The same measurement was repeated with a higher bandwidth (Figures 6.6 (d) and 6.6 (f)). Although the peak heights of the tunnelling events are now higher, they are still unequal. Further increase of the bandwidth was not possible, due to the low signal-to-noise ratio (SNR). The effect of the limited bandwidth is described in detail in one of the next sections.

6.2.3 Hole tunnelling times measurements

Due to the limited setup bandwidth, the extraction of the hole tunnelling times cannot be achieved from an experiment similar to that described in Figure 6.6. In order to circumvent the problem of the slow rise time an experiment was devised in which the information of a tunnelling event was encoded in a signal of a much longer duration than the rise time. A three-stage voltage pulse was now applied along the lower part of the break in the Coulomb peak (black dashed line in Figure 6.7(a)) in order to load (pink hexagon in Figure 6.7 (a)) and unload (pink triangle in Figure 6.7 (a)) a hole into/from the dot. Again each stage of the pulse lasted for 500 μs. The shape of the applied pulse is shown in the inset in Figure 6.7 (b), with pink triangles labelling the position when a hole is unloaded from the QD and a pink hexagon labelling the position when a hole is loaded into the dot.

A 30 kHz bandwidth single-shot reflection amplitude measurement of the sensor during the three-part pulse is shown in Figure 6.7 (b). During the first stage of the applied voltage pulse, when a hole is removed from the dot (pink triangle in Figure 6.7 (a)), the reflected signal is at its minimum. With the second, negative voltage pulse stage, a hole is loaded into the dot (pink hexagon in Figure 6.7 (a)); the reflected signal from the sensor reaches its maximum. Finally, the hole is again removed from the dot in the last stage of the pulse and the reflected signal returns to its minimum. The green dashed (red solid) line indicates the starting edge of the second (third) part of the pulse. 1000 such measurements were performed and the delay times (t_1 and t_2) were extracted. A hole was considered to have tunnelled into (out of) the QD if the reflected signal was higher (lower) than a certain threshold value of the reflection amplitude.

The extracted times for measurement bandwidths of 30 kHz are shown in the histogram plots, in Figure 6.7 (c) for tunnelling into the dot and in Figure 6.7 (d) for tunnelling out of the dot. From the exponential fit a tunnelling-in time of $\approx$ 6 μs and a tunnelling-out time of $\approx$ 4 μs was determined for thresholds equal to 0 and -7.5×10^{-5}, respectively. Different thresholds are chosen in order to largely avoid false counts coming from noise peaks surpassing the threshold value. It was set as high as possible for the tunnel-in and as low as possible for the tunnel-out time. However, it was found that the tunnelling times depend only slightly on the chosen threshold; they are always between 2-10 μs.

It seems, at a fist glance, that with a low-pass filter bandwidth of 30 kHz we are only able to measure rise times of $\approx$ 0.35/30 kHz =12 μs (see Appendix C), hence faster tunnelling times should not be detected.

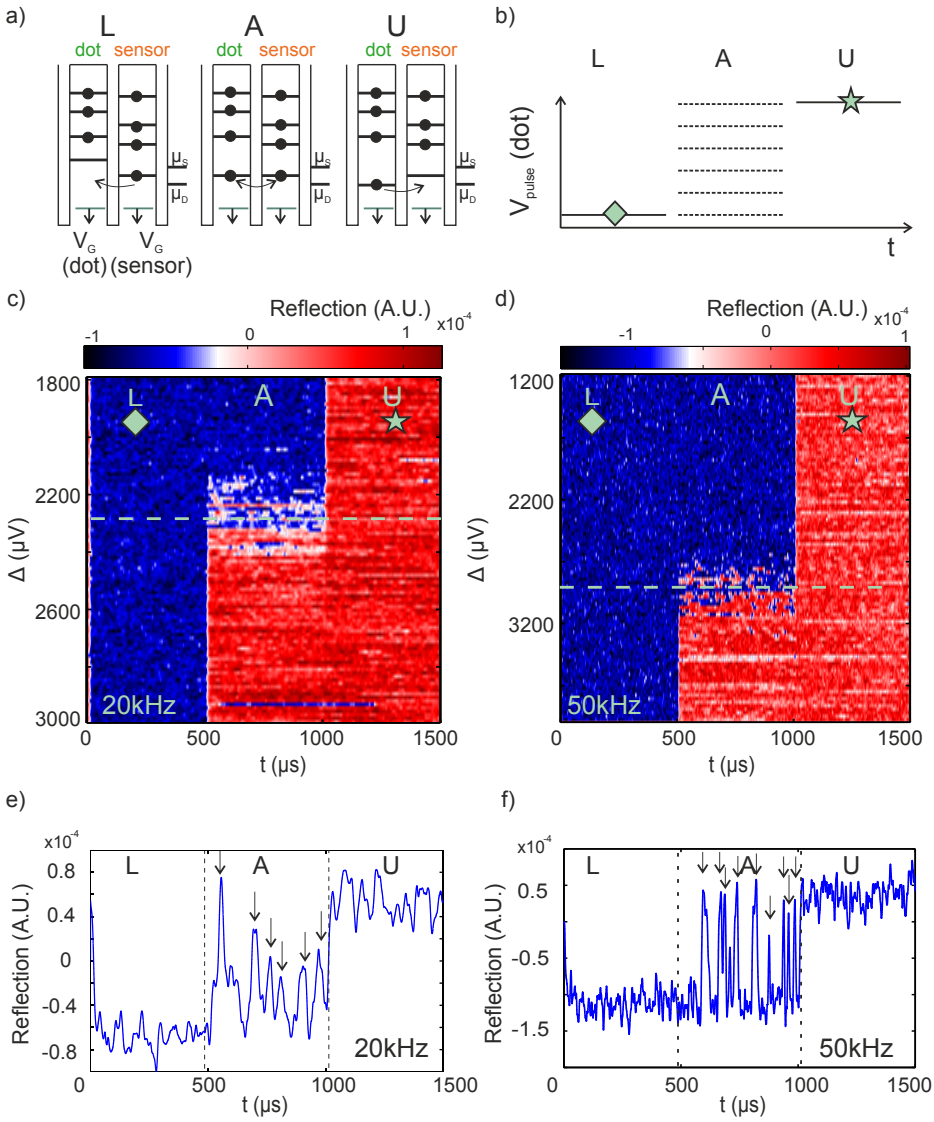

Figure 6.6: (a) Scheme showing the alignment of the electrochemical potentials of the dot and the sensor for three different conditions. In the left part a hole is loaded in the dot (L); in the middle the resonant tunnelling condition is achieved by aligning the electrochemical potentials (A) and on the right side a hole is unloaded from the dot (U). (b) Schematic showing the shape of the applied three-stage pulse. (c)-(d) Reflection amplitude of the sensor versus the relative voltage applied to the dot gate Δ in the align stage (A) and time t. The relative voltage $\Delta = 0$ corresponds to the load voltage. Loading and unloading of the hole is labelled with a green rhombus and a green star, respectively. The power of the RF signal on the *lock-in* output was -35 dBm, the low-pass filter bandwidth 20 kHz for (c), 50 kHz for (d) and V_{SD} 80 μV. (e)-(f) Single-shot reflectometry trace corresponding to the position of the green dashed line in (c) and (d), respectively, where the condition for resonant tunnelling is met. In the second stage of the pulse ($500\mu s < t < 1000\mu s$) several hole tunnelling events can be observed, indicated by black arrows.

However, the above described experiment allows us to circumvent the bandwidth limitation. In Section 6.2.4 it will be shown that the small bandwidth leads just to a shift of the histogram. Since the tunnelling

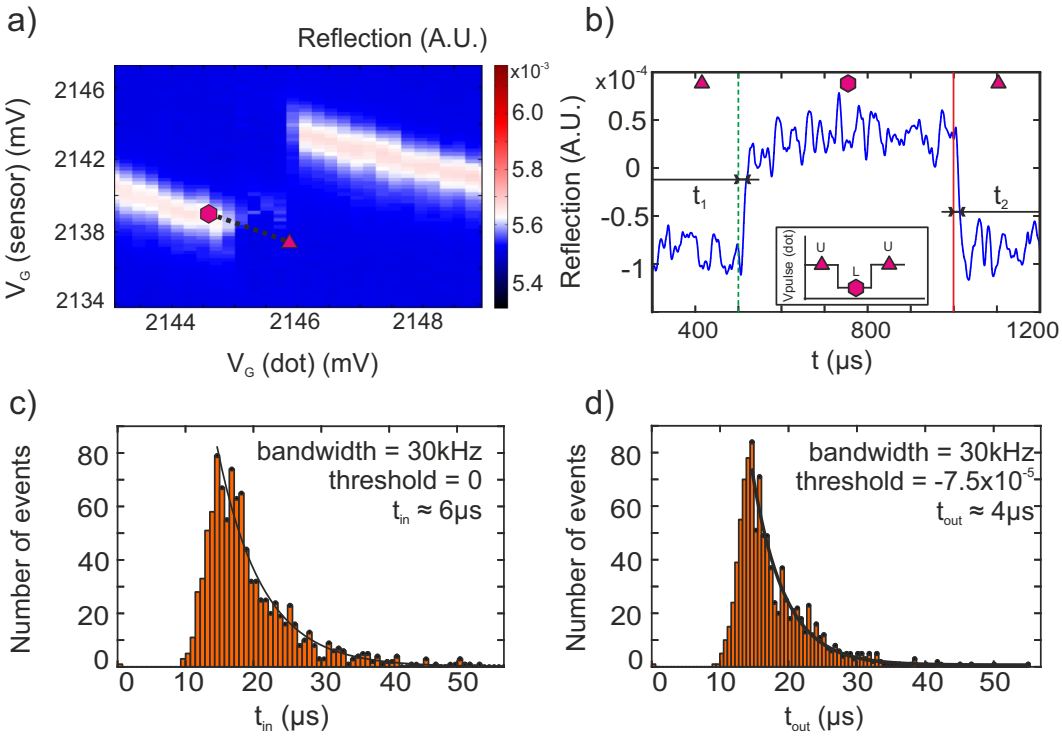

Figure 6.7: (a) Zoom-in of a stability diagram, measured in reflection. A pink hexagon (triangle) indicates the loading (unloading) position and the dashed black line the direction of pulsing. (b) Single-shot reflection amplitude measurement of the sensor vs time, taken with a bandwidth of 30 kHz. The reflection amplitude is recorded while unloading (labelled by triangles), loading (labelled by a hexagon) and again unloading a hole from the QD. The reflection amplitude is negative due to an offset in the instrumentation. The green dashed (red solid) line indicates the time when the loading (unloading) pulse was applied. The horizontal black lines indicate a threshold value above (below) which a tunnelling in or tunnelling out event is considered to have happened. The inset shows the shape of the applied pulse. (c)-(d) Histogram of the delay times for loading and unloading the dot for 30 kHz. From the exponential fit (solid black line) the tunnelling times were extracted. The counts at the beginning of the histograms are attributed to the Gaussian noise distribution.

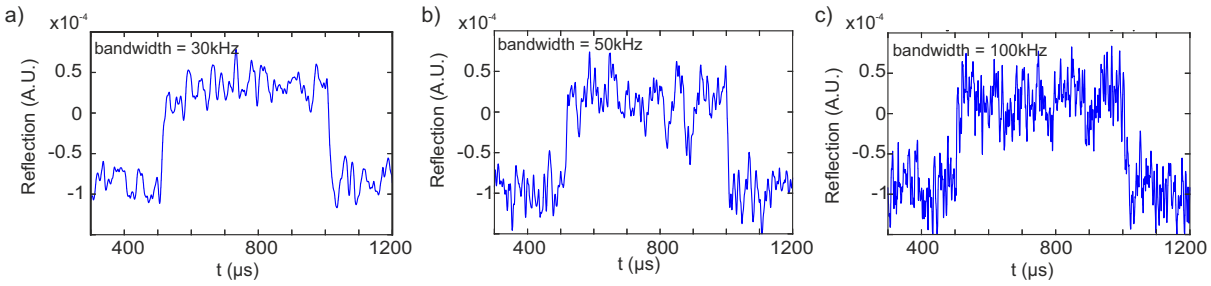

Figure 6.8: Single-shot reflection amplitude measurement of the sensor vs time for (a) 30 kHz bandwidth, (b) 50 kHz bandwidth and (c) 100 kHz bandwidth.

times are extracted from the exponential fit, they are not influenced by such a shift.

Tunnelling time measurements for different bandwidths, loading levels and Coulomb peak breaks

The same measurement and analysis were repeated for higher bandwidths, along the same Coulomb peak break (Figure 6.7 (a)). Figures 6.8 (a)-(c) show the comparison of the reflection amplitudes for bandwidths of 30 kHz, 50 kHz and 100 kHz, respectively. Similarly, figures 6.9 (a)-(b), (c)-(d) and (e)-(f) show the comparison of tunnelling-in and tunnelling-out times for bandwidths of 30 kHz, 50 kHz and 100 kHz, respectively. The extracted tunnelling in and out times (see Figure 6.9 insets) for bandwidths of 50 kHz and 100 kHz are in the same range as those extracted for the bandwidth of 30 kHz. Comparing Figures 6.8(a)-(c), one can see that the measurements taken with higher bandwidths have lower SNR, as expected. That is the reason why we performed more measurements of this type with lower bandwidths, since it gives cleaner measurements and the only consequence is that the histograms are shifted on the x-axis, but this is not influencing the exponential fit.

Furthermore, we repeated similar measurements for two additional levels, +1 mV and +2 mV relative to the loading level of Figure 6.9 (see Figure 6.10). Different loading levels could influence the tunnelling times, since the difference between the two electrochemical potentials (one of the QD and one of the SHT) is varied. The measurements were taken at the same Coulomb peak break as the previous measurements, with 30 kHz bandwidth. The histograms are shown in Figure 6.11 and the extracted tunnelling times are given as an inset in each graph. Once more, we see no difference within the experimental error. However, additional experiments should be performed before concluding whether the loading depth influences the tunnelling times.

Finally, in order to check if there is a back-action mechanism involved when loading and unloading the QD, the same experiment was repeated once more, but this time along the upper part of the Coulomb peak break (see Figure 6.3 (b)), where the SHT is off during the tunnelling event. The extracted tun-

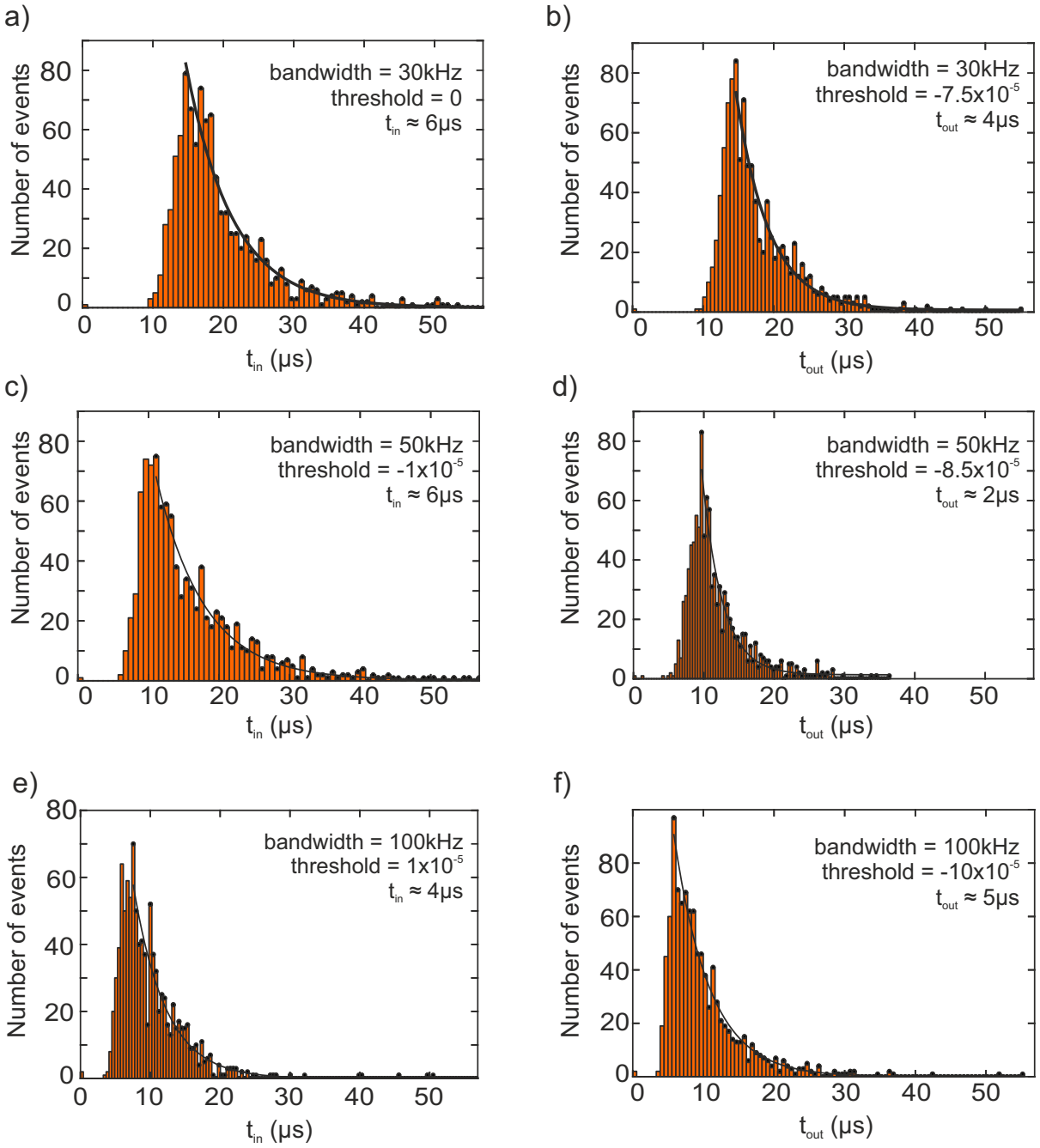

Figure 6.9: Histograms of the delay times for loading and unloading the dot for (a)-(b) 30 kHz bandwidth; (c)-(d) 50 kHz bandwidth; (e)-(f) 100 kHz bandwidth, respectively.

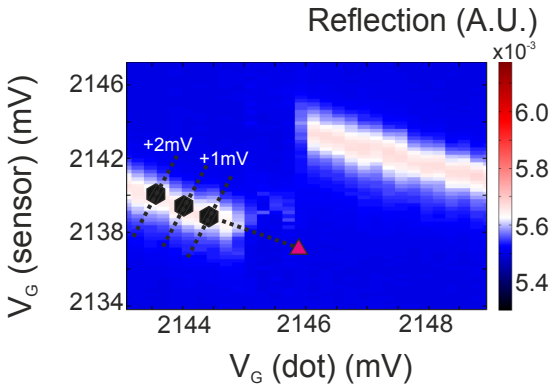

Figure 6.10: Zoom-in of a stability diagram, measured in reflection, with hexagons labelling three different loading levels for which tunnelling time measurements were performed.

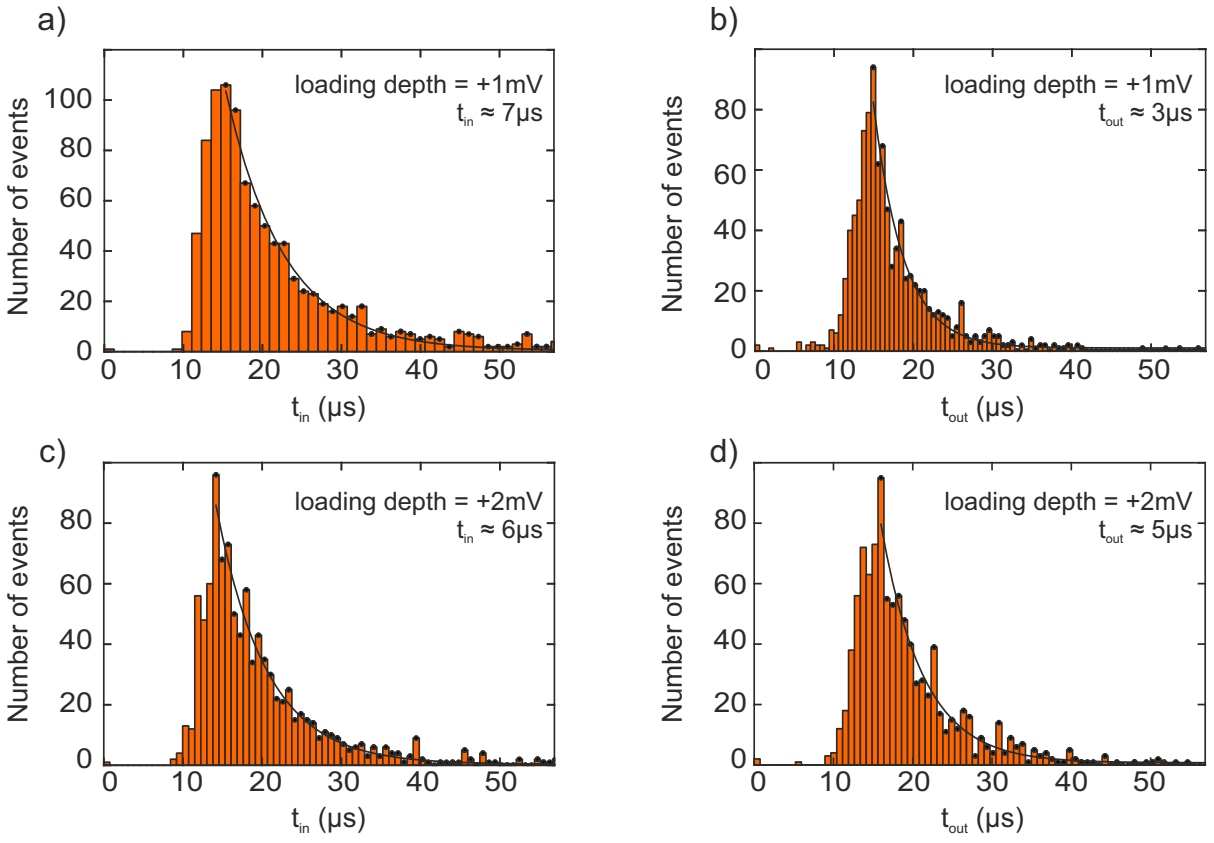

Figure 6.11: Histograms of the delay times for loading ((a) and (c)) and unloading ((b) and (d)) the dot for the additional different loading levels. The extracted tunnelling times are given as an inset in each graph. The bandwidth of the measurements was 50 kHz.

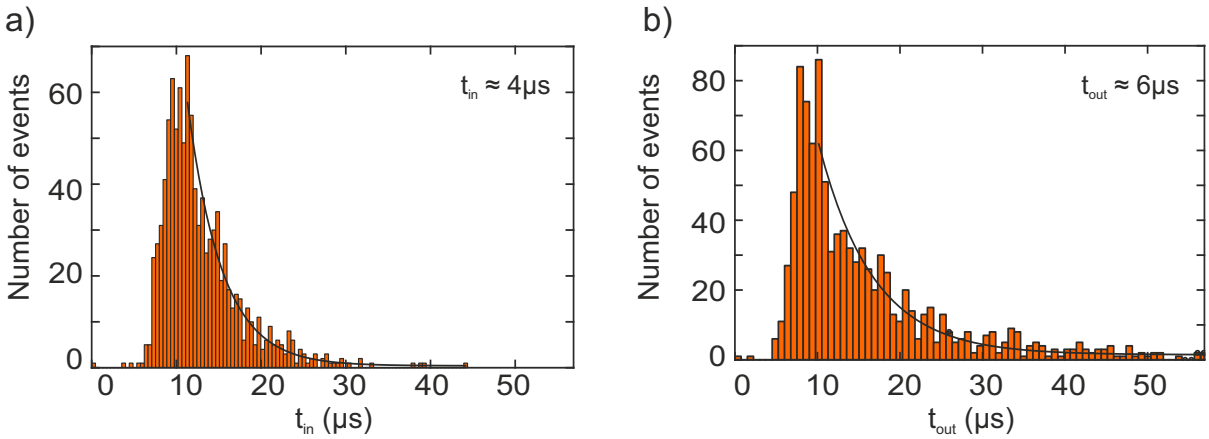

Figure 6.12: Histograms of the delay times for loading (a) and unloading (b) the dot, taken at the upper part of the Coulomb peak break (see Figure 6.3 (b)), taken with a bandwidth of 50 kHz. The extracted tunnelling times are given as an inset in each graph.

nelling in and out times are still in line with the ones from the other measurements (see inset of Figure 6.12).

In conclusion, the demonstrated charge sensing in Ge HWs based on a capacitive and tunnel coupling mechanism, together with the implemented RF reflectometry readout enabled the detection of single-hole tunnelling events. The extracted short hole tunnelling times of a few microseconds allowed more advanced spin readout experiments, which will be presented in the next chapter.

6.2.4 Demonstration of the validity of the performed experiment

Effect of the finite rise time of the low pass filter on the extracted tunnelling times

We made a simple simulation of our experiment in order to explain the possibility to measure tunnel events on a microsecond time scale even if the low pass filter rise time is several times longer. The setup of the simulated experiment is shown in Figure 6.13.

A square waveform 1 (see Figure 6.13) with the amplitude of 0.2 mV was generated and sent out from the 1st channel of the AWG; it corresponds to the pulse applied in order to load a hole inside the QD. A similar square waveform 2 (see Figure 6.13) was generated from the second channel of the AWG, with delay times of 5 μs and 7 μs and is used to simulate the response of the sensor after a hole has tunnelled into the QD. This second waveform was fed to the *IF* port of an RF mixer. A sinusoidal carrier signal of 100 MHz was generated from the UHFLI *out 1* port and fed to the *LO* port of the mixer in order to imitate the reflectometry signal. The result of the multiplication of these two signals, was fed to the UHFLI *input 2* from the mixer *RF* port and measured with its scope (see Figure 6.13). The scope

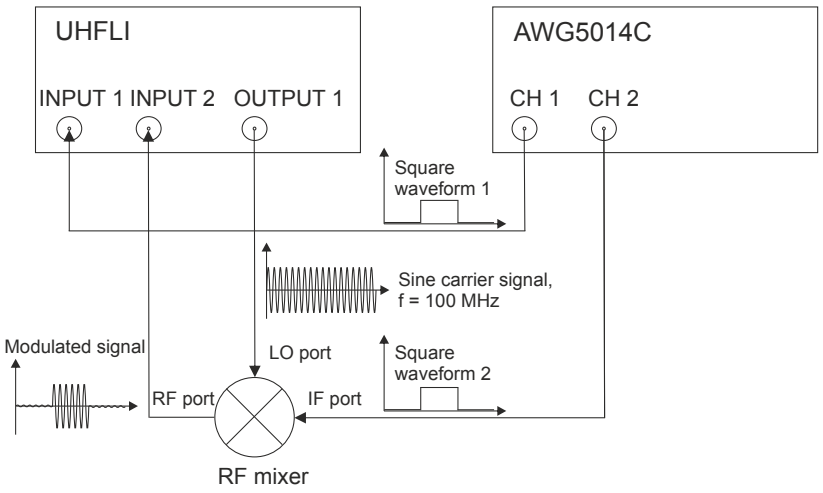

Figure 6.13: Schematic showing the setup of the simulated experiment

sampling rate was set to 900 MHz. To observe the influence of the UHFLI demodulator, the signal was fed through it with a low pass filter of 20 kHz (4th order) (Figure 6.14 (c) for the delay time of of 5 μs and Figure 6.14 (d) for the delay time of of 7 μs), as it was the case in the tunnelling times experiments. The threshold for the 'tunnel time measurement' for this simulation was set to 100 mV, a value where the demodulated signal has already started to increase. Comparing Figures 6.14 (c) and (d), we can see that an additional delay of 15 μs , originating from the slow rise time, is added for both 5 μs and 7 μs tunnel event equally, proving that the filter behaviour is constant and simply adds a constant offset in the measurement. However, due to the fact that the pulse duration, marked as L, in the tunnelling time experiments described in the previous section, is more than 30 times the rise time, all tunnelling events are observed. The amplitudes of all measurement simulations shown here are 5-6 orders of magnitude higher than in the real experiment, because the frequency mixer (Mini Circuits ZX05-1L+) used in the simulations operates properly only for certain input voltage ranges.

We have repeated the same simulation for 30 kHz, 50 kHz and 100 kHz low pass filter bandwidths and the final difference between the two signals simulating the tunnelling events was always 2 μs (see Figures 6.15, 6.16), as it would be for an infinite bandwidth setup.

Summarizing, the low-pass filter bandwidth does not influence our measurement, since we measure only the relative delay. The consequence of measuring with a smaller bandwidth is just a shift of the whole histogram on the x-axis (Figure 6.9). The shift of the fitted histograms is inversely proportional to the low-pass filter bandwidth: the higher the bandwidth, the closer to zero time is the histogram. The histograms shift to smaller delay times for higher bandwidth but the extracted tunnelling times are the same.

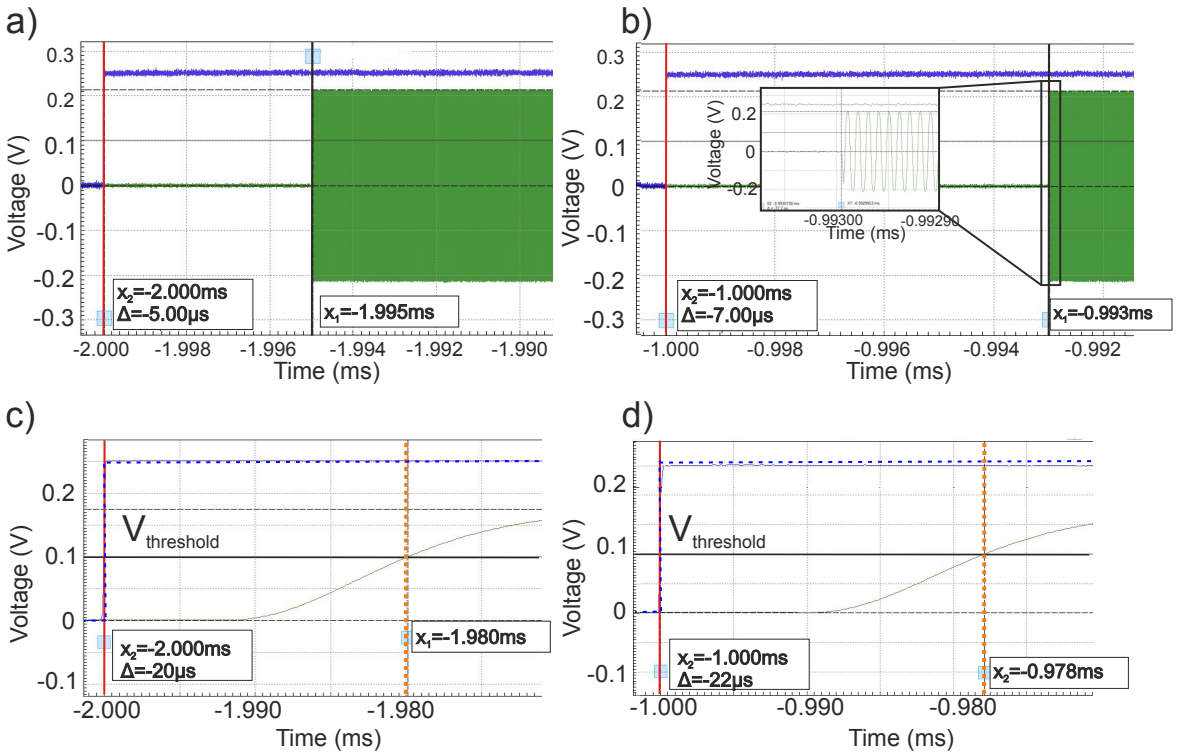

Figure 6.14: Measurements of the simulated experiment proving the validity of our experimental approach. (a) In blue the square waveform corresponding to the pulse for loading a hole is shown (square waveform 1 in Figure 6.13). The beginning of the pulse is denoted with the red vertical line. The second square waveform (square waveform 2 in Figure 6.13), multiplied with a 100 MHz sinusoidal signal, simulating the tunnelling event is shown in green. The high level of this second waveform is delayed for 5 μs (denoted with the black vertical line) simulating the time it takes for a hole to tunnel into the QD after the waveform 1 (shown in blue) has been applied. (b) Similar to (a) but here, the second waveform is delayed for 7 μs. In the inset a zoom-in of the 'reflectometry carrier signal' of 100 MHz modulated with the square waveform, is shown. (c) - (d) Demodulated signal measured after the low pass filter of 20 kHz (4th order), simulating tunnel events which take place after delay times of 5 μs and 7 μs, respectively. Red vertical lines denote the beginning of the square waveform 1 (blue) and the vertical dashed orange lines the time when the demodulated signal (green) has passed the chosen threshold. The simulation reveals that the slow rise time adds and additional delay time of 15 μs for both tunnel events.

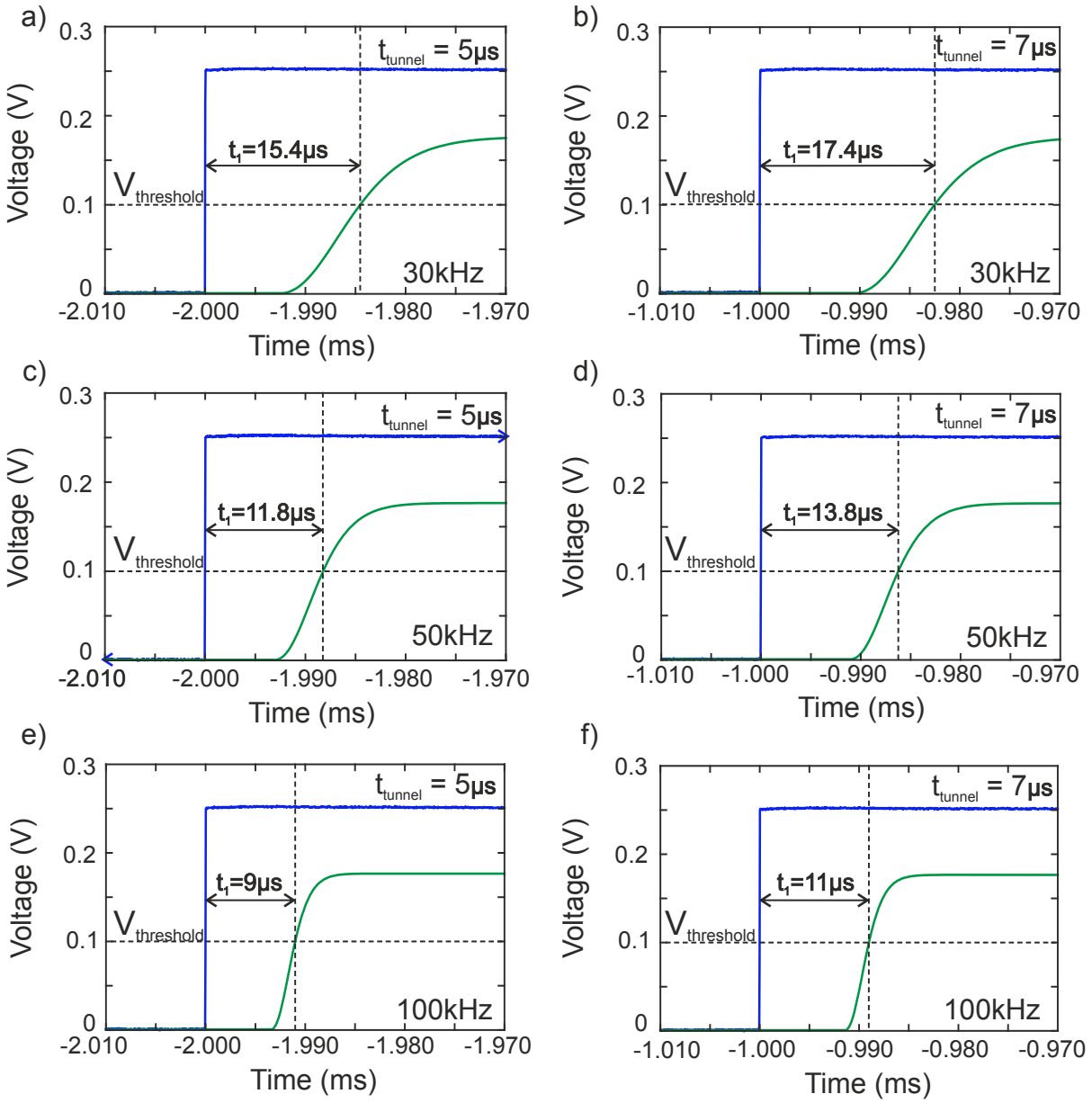

Figure 6.15: Simulated total delay times (tunnelling time + rise time of the low pass filter) for (a)-(b) 30 kHz, (c)-(d) 50 kHz and (e)-(f) 100 kHz bandwidths, for two tunnelling events, 5 μs (left column) and 7 μs (right column). The square waveform corresponding to the pulse for loading/unloading the hole is shown in blue and the demodulated signal simulating the tunnel events is shown in green. The difference between the two signals simulating the tunnelling events of 5 μs and 7 μs is always 2 μs.

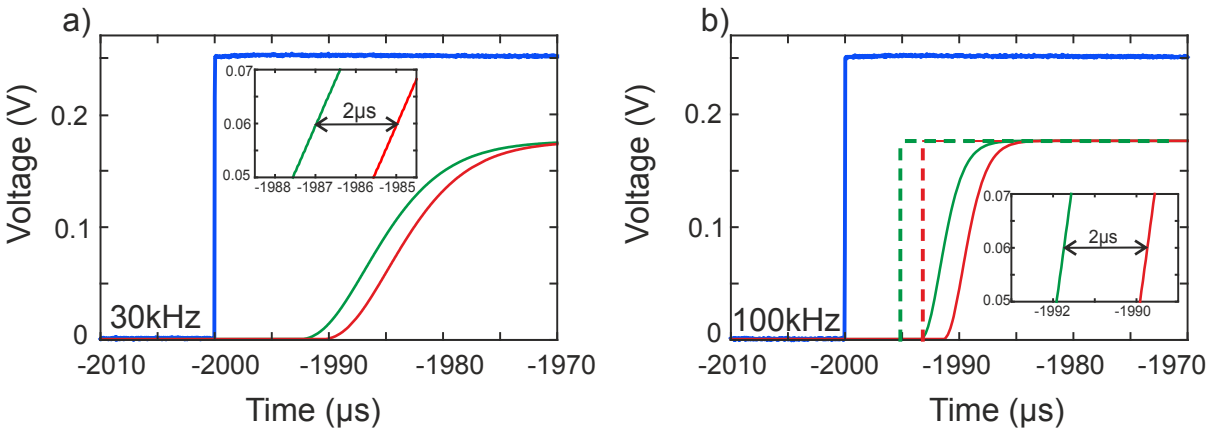

Figure 6.16: (a)-(b) Summary of the results of the simulated experiment for bandwidths of 30 kHz and 100 kHz, respectively. The blue solid line represents the applied pulse for loading/unloading the hole, the green and red solid lines demodulated signal simulating the tunnelling events and the green and red dashed lines on (b) represent the case when the tunnelling event would take place if the bandwidth would have been infinite. In the insets the constant difference between the two simulated tunnelling events is shown.

Effect of the small bandwidth on the peak heights

While measuring with lower bandwidths does not affect the extraction of the tunnelling times, it does limit us in experiments such as those shown in Figure 6.6 (e) and Figure 6.6 (f). Due to the low bandwidth, peaks in Figure 6.6 (e), (f) are not always reaching the maximum reflected amplitude and have unequal heights. In order to elucidate this we made another simple simulation of our experiment. The setup is basically the same as shown in Figure 6.13.

A square waveform that simulates the reflectometry response of the sensor to a hole tunnelling event was generated and sent out from the AWG (blue trace in Figure 6.17). It was measured with the UHFLI scope. In order to achieve acceptable signal to noise ratio we needed to restrict the bandwidth, though it should represent the 'infinite' bandwidth case. The green trace in Figure 6.17 shows the response of UHFLI's demodulator to such a tunnel event, taken with a low pass filter bandwidth of 20 kHz (4th order), like in our measurement. A reduction of the waveform 1 width (faster tunnelling event) results in a decrease of the demodulated waveform amplitude once the width gets shorter than the rise time of the demodulated waveform. The faster a tunnelling event the smaller the peak.

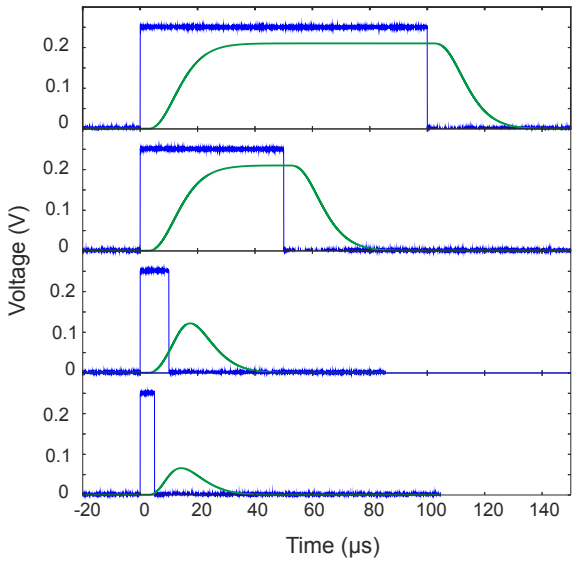

Figure 6.17: Measurement simulation intended to explain the difference in tunnelling peak heights. The blue square pulse simulates the tunnelling events recorded with an infinite bandwidth setup. Green traces are tunnelling events recorded with the bandwidth of 20 kHz (4th order) like in the measurement. The duration of the blue square pulse simulating the tunnelling event is 100 μs, 50 μs, 10 μs and 5 μs, from top to bottom.

7 Single-shot readout of hole spins in Ge

For spin readout measurements, the same type of device and reflectometry-based readout setup described in Chapter 6 is used (Figure 6.2). The difference is that here the fast gate and the input reflectometry lines were attenuated by 27 dB and 42 dB, respectively, and that the matching circuit consisted of an 820 nH inductor and a varactor which was biased with 3 V. The PCB details and manufacturer numbers are given in Appendix B, Table B.2.

In the presence of an external magnetic field, single-hole tunnelling events presented in Chapter 6 become spin selective. In order to detect the spin selectivity, the Zeeman splitting, $E_Z = g\mu_B B$ must be larger than the width of the Fermi distribution of the SHT states.

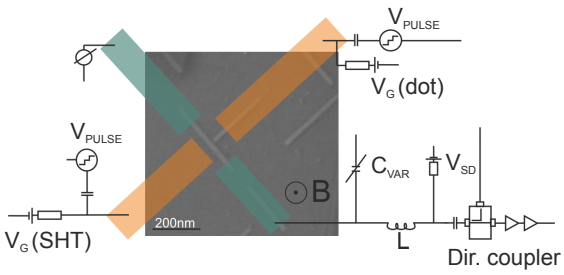

Figure 7.1: Device and setup scheme for the spin readout experiment

7.1 Spin readout sequence

For the spin readout measurement we used the already well established three-stage pulsing sequence implemented by Elzerman et al. [79] to do spin-to-charge conversion. The spin-to-charge conversion used here is based on the energy difference between the two spin states. For holes in Ge, the ground state is occupied by a spin-down hole, and the excited state by a spin-up hole [81].

Parts of this Chapter are uploaded to arXiv.org

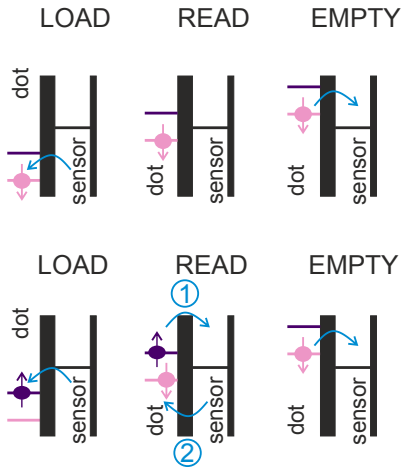

Figure 7.2: Spin readout protocol. For easier understanding, in this chapter the electron convention is used in the diagrams showing the alignment of electrochemical potentials. The upper (lower) panel shows the case when a spin-down (up) is loaded.

Spin readout sequence for a QD coupled to the SHT

In a first stage (*load*), the hole electrochemical potentials of the QD for both spin-up ($\mu_\uparrow$) and spin-down ($\mu_\downarrow$) are well below the charge sensor Fermi level (μ_{SHT}): $\mu_\uparrow, \mu_\downarrow < \mu_{SHT}$. A hole with an unknown spin will be loaded from the sensor into the dot (Figure 7.2, 'load' column). The second stage is a *read* stage. $\mu_\uparrow$ and $\mu_\downarrow$ are brought in a configuration where $\mu_\uparrow$ is above and $\mu_\downarrow$ below μ_{SHT}: $\mu_\downarrow < \mu_{SHT} < \mu_\uparrow$. Depending on the spin of the loaded hole, one distinguishes between two cases, depicted in Figure 7.2, 'read' column. When a spin-down hole is loaded, it stays in the QD since in the read stage $\mu_\downarrow$ is below μ_{SHT}. When a spin-up hole is loaded, it will tunnel to the SHT, because $\mu_\uparrow > \mu_{SHT}$ (labelled with number 1 in Figure 7.2, lower panel). After that, the QD gets refilled with a spin-down hole ($\mu_\downarrow < \mu_{SHT}$, Figure 7.2, number 2 in the lower panel). Finally, in the third *empty* stage, $\mu_\uparrow, \mu_\downarrow > \mu_{SHT}$; the spin-down hole will leave the QD and the new sequence can begin.

The above described spin readout sequence will work only if the energy spacing (ΔE) in the SHT is much smaller than E_Z and comparable to $k_B T$, because we need the sharp Fermi distribution in the SHT [76]. In other words, the density of states in the SHT should be continuous on the energy scale set by E_Z. This can be achieved my making the gap between the source and the drain electrodes of the SHT large enough. In our experiments we have neither observed the existence of excited states in the SHT nor asymmetric spin signature which would be characteristic for an SHT with discrete states [82]. Therefore, we have concluded that our SHT fulfills these requirements.

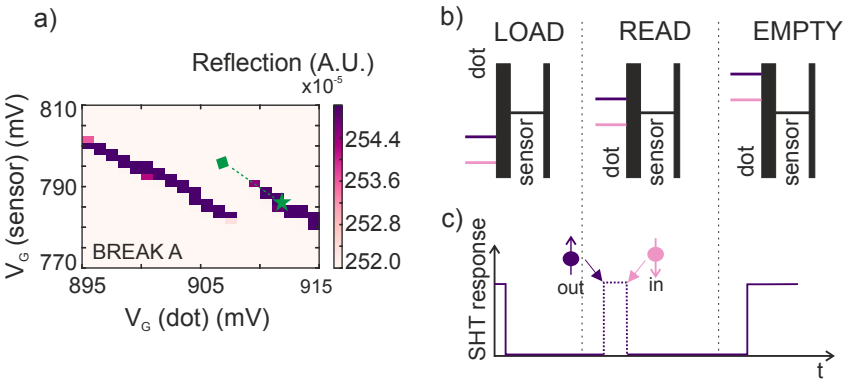

Figure 7.3: (a) Zoom-in of a stability diagram obtained by sweeping the gate of the QD versus the gate of the charge sensor, at a magnetic field of 1100 mT, where the pulsing sequence was applied. The load (empty) position is labelled with the green star (diamond). (b) Schematics showing the electrochemical potentials of the QD and the charge sensor during different stages of the pulsing sequence used for the single-shot spin readout. The lower electrochemical potential corresponds to a spin-down state. For simplicity, the electron convention is used in the diagrams showing the alignment of electrochemical potentials. (c) Expected response of the SHT when the sequence is applied along the upper part of the Coulomb peak break and a spin-up hole is loaded.

Expected charge sensor response

The experiments described in this Chapter are performed along the upper part of the charge sensor's Coulomb peak break (see Figure 7.3 (a), green dashed line). Again the diagonal pulsing is applied, as described in Section 6.2.1. A hole is loaded in the dot with applying a negative voltage pulse to the QD gate. Our charge sensor is therefore calibrated in such a way that when the QD is loaded, the reflected amplitude (RA) shows its minimum, when it is emptied, maximum. The spin readout protocol and expected charge sensor response for our device are schematically depicted in Figures 7.3 (b) and (c), respectively. We start the pulsing sequence by positioning ourselves on the upper part of a Coulomb peak (green star in Figure 7.3 (a). This corresponds to the *empty* status of the QD and it is a reference point for the applied voltage pulses. The SHT shows maximum RA. With a negative voltage pulse applied on the QD gate (typically few mV), a hole is loaded in the QD (green diamond in Figure 7.3 (a)). The electrochemical potentials are brought in the read configuration by the second stage voltage pulse, less negative than the one used for emptying the QD. The procedure how to determine the correct amplitude to bring the electrochemical potentials in the desired configuration ($\mu_{\downarrow} < \mu_{SHT} < \mu_{\uparrow}$) is described in paragraph 7.1.1. In case a spin-down hole is loaded, the SHT RA stays at its minimum during the read stage. However, when a spin-up hole is loaded it can tunnel out of the QD. As a consequence the SHT RA obtains its maximum value until it switches back to the minimum value when the QD gets refilled with a spin-down hole. In the last stage the QD is emptied: both $\mu_{\downarrow}$ and $\mu_{\uparrow}$ are brought above μ_{SHT} and the SHT again shows the maximum RA. The amplitude of the applied pulse on the QD gate is zero at the reference point (position of the green star in Figure 7.3 (a)).

7.1.1 Spin signature and calibration of the read level

For determining the correct position of the read level for which spin dependent tunnelling is occurring, a similar three-stage sequence was applied (Figure 7.4 (a)), with the difference that the amplitude of the read stage was varied. The position of the reference point ($V_{\mathrm{pulse}} = 0\,\mathrm{mV}$ in Figure 7.4 (a)) for voltage pulses is still at the position of the green star (Figure 7.3 (a)). This experiment is equivalent to the one for observing single-hole tunnelling events, described in Section 6.2.2, only now a magnetic field is applied.

From a single-shot read level calibration measurement (Figure 7.4 (b)) different RA responses of the SHT are shown depending on the position of the read level. When the read level is set too low (Figure 7.4 (d), no hole can leave the QD during the read stage. This is the case when $\mu_{\uparrow}, \mu_{\downarrow} < \mu_{SHT}$, equivalent to the load stage. The amplitude of the voltage pulse applied to the QD gate for this case is labelled with the red vertical line in Figure 7.4 (b). The SHT shows minimum RA in the read stage. When the read level is set too high (Figure 7.4 (h)), the configuration of electrochemical potentials is equivalent to the empty stage ($\mu_{\uparrow}, \mu_{\downarrow} > \mu_{SHT}$) and the hole will always tunnel out during the read stage. The SHT shows maximum RA in the read stage. The applied voltage pulse on the QD gate is close to 0 mV (blue vertical line in Figure 7.4 (b)). The SHT response for the correct position of the read level ($\mu_{\downarrow} < \mu_{SHT} < \mu_{\uparrow}$) is shown in Figures 7.4 (e) and (f). The amplitude of the voltage pulse applied to the QD gate is labelled with the green vertical line in Figure 7.4 (b). Figure 7.4 (e) shows the case when the spin-up was loaded and in the SHT response we see a peak. Figure 7.4 (f) shows the case when the spin-down was loaded and the SHT shows minimum RA in the read stage. One more configuration of electrochemical potentials can be observed: the case when $\mu_{\downarrow} \approx \mu_{SHT}$. We observe a random telegraph signal in the SHT RA in the read stage, showing the continuous exchange of holes between the QD and the SHT (Figure 7.4 (g)). The amplitude of the voltage pulse applied to the QD gate for this case is labelled with the yellow vertical line in Figure 7.4 (b).

Averaging about 200 of such single-shot measurements reveals the spin signature (Figure 7.4 (c)) as a purple tail at the beginning of the read stage. One can choose the amplitude of the second stage of the pulse anywhere in the range labelled with the double black line in Figure 7.4 (c). Of course, the higher the magnetic field, the bigger the range one can choose, since the Zeeman splitting is larger. Consequently, in higher magnetic fields one is much less sensitive in choosing the correct position of the read level, as well as to the sometimes unavoidable drifts in the measurement.

The lowest out-of-plane magnetic field for this Coulomb peak break (shown in Figure 7.3, labelled with A in the text), for which the spin signature was clearly observed was 500 mT. Due to the thermal broadening one could not see it for lower magnetic fields, at the same Coulomb peak break. However, if a QD confines different number of holes, their g-factor, and therefore the Zeeman splitting, can be

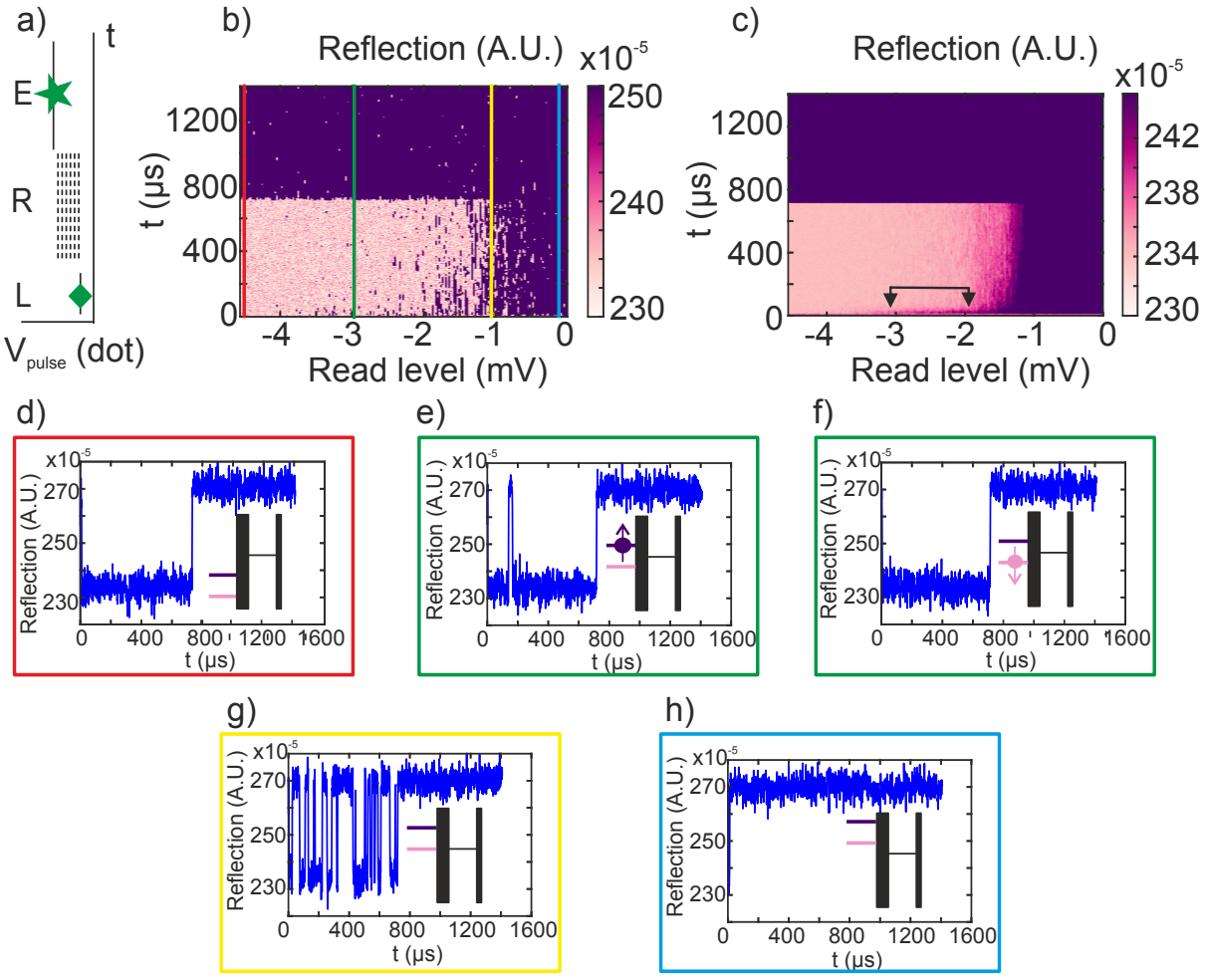

Figure 7.4: Single-shot spin readout and calibration of the read level for the break A. (a) Three-stage pulsing sequence. The duration of the load stage is 8 μs and that of the read and empty stages 700 μs. (b) Single-shot measurement of the reflection amplitude as a function of the voltage applied to the QD gate during the read stage, taken at the magnetic field B = 1100 mT, with a detection bandwidth of 200 kHz. The applied V_{SD} was 130 μs. The load stage is hard to resolve, as its duration is much shorter than the duration of the read and empty stages. (c) Reflection amplitude, averaged over 197 single-shot traces as a function of the voltage applied on the QD gate during the read stage, taken at the magnetic field B = 1100 mT. The double black arrow indicates the region where we see the spin signature. (d)-(h) Examples of single-shot traces; the schematics in the insets elucidate the alignment of the electrochemical potentials at the positions indicated by vertical lines in (b). (d) The read level is set too low: $\mu_\uparrow, \mu_\downarrow < \mu_{SHT}$, no hole can leave the QD during the read stage. (e) Correct position of the read level: $\mu_\downarrow < \mu_{SHT} < \mu_\uparrow$. Single-shot trace for the case of loading a spin-up hole. (f) Correct position of the read level: $\mu_\downarrow < \mu_{SHT} < \mu_\uparrow$. Single-shot trace for the case of loading a spin-down hole. (g) $\mu_\downarrow \approx \mu_{SHT}$. Random telegraph signal showing the continuous exchange of holes between the QD and the SHT. (h) The read level is set too high: $\mu_\uparrow, \mu_\downarrow > \mu_{SHT}$: the hole can always tunnel out during the read stage.

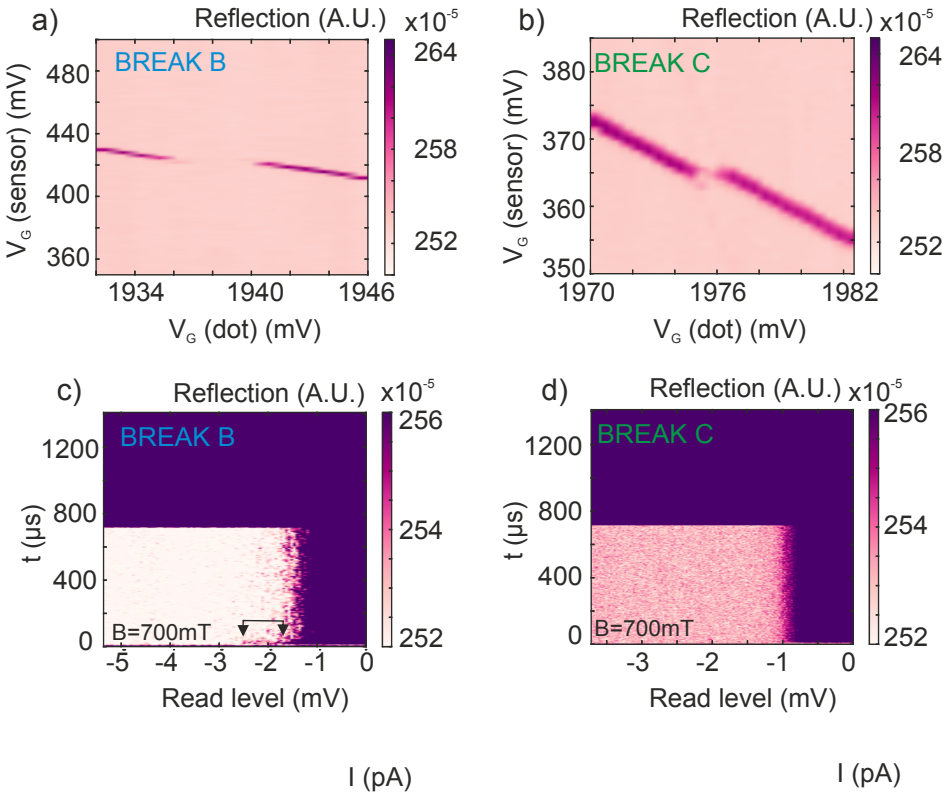

Figure 7.5: (a)-(b) Stability diagrams taken for more positive QD gate voltages, where the QD confines less holes, revealing neighbouring Coulomb peak breaks (B and C). (c) Reflection amplitude, averaged over 23 single-shot traces as a function of the voltage applied on the QD gate during the read stage at the break B (shown in (a)). V_{SD} was 130 μs. (d) Reflection amplitude, averaged over 23 single-shot traces as a function of the voltage applied on the QD gate during the read stage at the break C (indicated in (b)). Applied V_{SD} was 100 μs. For this break the spin signature is not observed. All measurements are taken at B = 700 mT and with a detection bandwidth of 100 kHz.

different [33], and the spin signature can be observed even for lower magnetic fields. This was the case for another Coulomb peak break (break B, Figure 7.5 (a), (c)), which confines roughly 10-20 holes less than at the position of break A. The spin signature can be observed already for 400 mT.

For a QD confining an even number of holes, no Zeeman splitting is taking place and thus the spin signature cannot be observed. We measured a break C, next to the break B, and indeed could not see the spin signature (Figure 7.5 (b), (d)).

In-plane magnetic field

The same type of measurement was repeated for the in-plane magnetic field, for the break A. The spin signature was not observed up to 9 T, the maximum field we could apply. We attribute this to the fact that for in-plane magnetic fields the hole g-factors (and therefore Zeeman splittings) can be rather

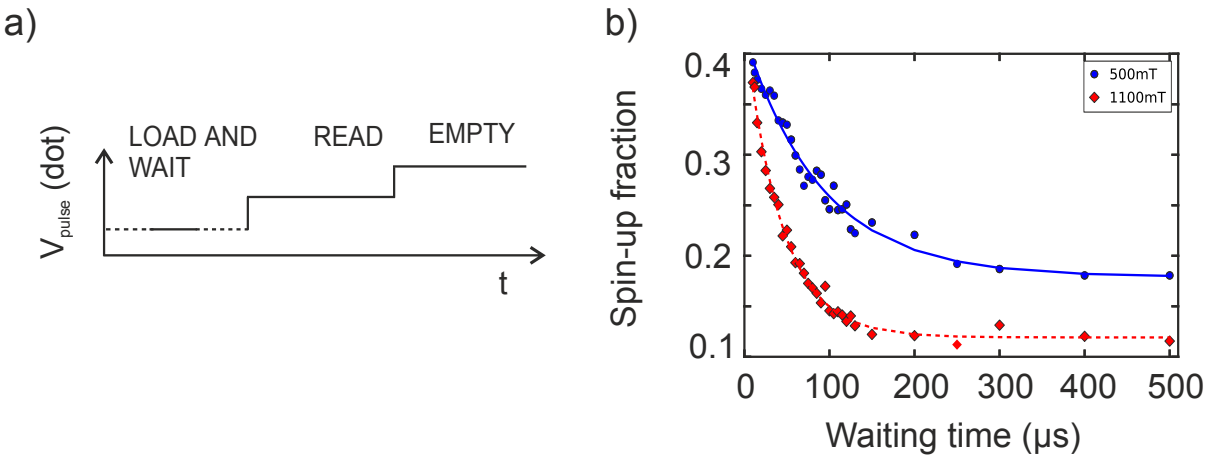

Figure 7.6: (a) Three stage pulsing sequence for measuring the spin relaxation time. The duration of both the read and the empty stage is 700 μs and the duration of the load stage was varied from 10 μs to 500 μs. (b) Exponential decay of the spin-up fractions versus the waiting time for B = 500 mT and B = 1100 mT, obtained by the single-shot analysis. The values were extracted for a normalized threshold value equal to 0.70, where threshold = 1 corresponds to the average maximum SHT RA and threshold = 0 to the average minimum SHT RA.

small [33].

7.2 Relaxation time measurements

Once the correct position of the read level is determined, the sequence for the spin readout measurement can be applied (Figure 7.6 (a)). In order to extract the hole spin relaxation time, the duration of the first, load stage of the pulse, is varied, while the durations of the read and empty stages are kept constant. The probability of observing a spin-up hole decreases exponentially with the waiting time. We varied the waiting times from 10 μs to 500 μs. Shorter waiting times were not taken into account, since the probability of loading a hole into the QD is not very high.

Single-shot analysis

Figure 7.6(b) shows the exponential decays of the spin-up fractions versus the waiting time for two different out-of-plane magnetic fields, B = 500 mT and B = 1100 mT. The extracted hole spin relaxation times for these fields are T_1 of (86 ± 6) μs and (32 ± 2) μs, respectively.

The spin-up fractions were determined by analysing around 2000 single-shot traces. An example of a single-shot trace is shown in Figure 7.7, for a loading time of 10 μs and a magnetic field of 500 mT. At the beginning the QD is in the empty stage and the SHT RA is at maximum. The beginning of the load stage

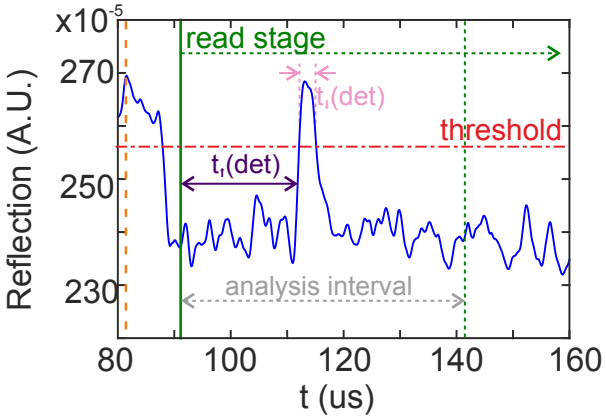

Figure 7.7: Example of a single-shot trace for a loading time of 10 us and a magnetic field of 500 mT. Labels indicating the beginning of the load stage (dashed orange line), the beginning of the read stage (from the the vertical solid greed line), the analysis interval (grey double arrow) and the threshold (dot-dashed red line) are shown. The detection time of a spin-up hole tunnelling event is labelled with the purple double arrow and the time needed for a spin-down hole to tunnel back in the QD with the pink arrows.

is labelled with the vertical dashed orange line in Figure 7.7. The moment when the levels of the dot are pulsed to the read stage is labelled with the vertical solid greed line in Figure 7.7. The spin is interpreted as a spin-up if the SHT shows RA higher than the chosen threshold, within the analysis interval, which is indicated with a horizontal dot-dashed red line in Figure 7.7. For the analysis we considered the interval of 50 μs (grey double arrow from the green solid to the green dashed line in Figure 7.7). The reason for this choice was that for tunnelling times of about 10μs, the number of counts for spin-up tunnelling-out events is less than 1% after 50μs.

The analysis was done for different normalized thresholds, where threshold = 1 corresponds to the average maximum SHT RA and threshold = 0 to the average minimum SHT RA. The hole spin relaxation times reported above were extracted for a threshold value equal to 0.70. The dependence of the result on a chosen threshold is discussed in Section 7.3.

The measurements were repeated for different magnetic fields, both for breaks A and B. The results are shown in Figure 7.8 (a). As expected, the spin relaxation rate T_1^{-1} increases when increasing the magnetic field B. The magnetic field dependence of T_1^{-1} does not follow the B^5 curve which has been shown for electrons in GaAs and Si [23, 77, 80]. Plotting the results in the log-log scale (Figure 7.8 (b)) reveals a $B^{1.5}$ (break A) and a $B^{1.4}$ (break B) dependence of the spin relaxation rate, which is deviating from what theory predicted for Ge/Si core/shell nanowires [83]. The reason for this deviation is not yet clear. However, in this rather small range of magnetic fields where the experiment was performed, several functions could be in agreement with the data (see Figure 7.8 (c)). Therefore, values at higher magnetic fields are needed to extract the correct magnetic field dependence, but for larger magnetic fields the relaxation times become very short.

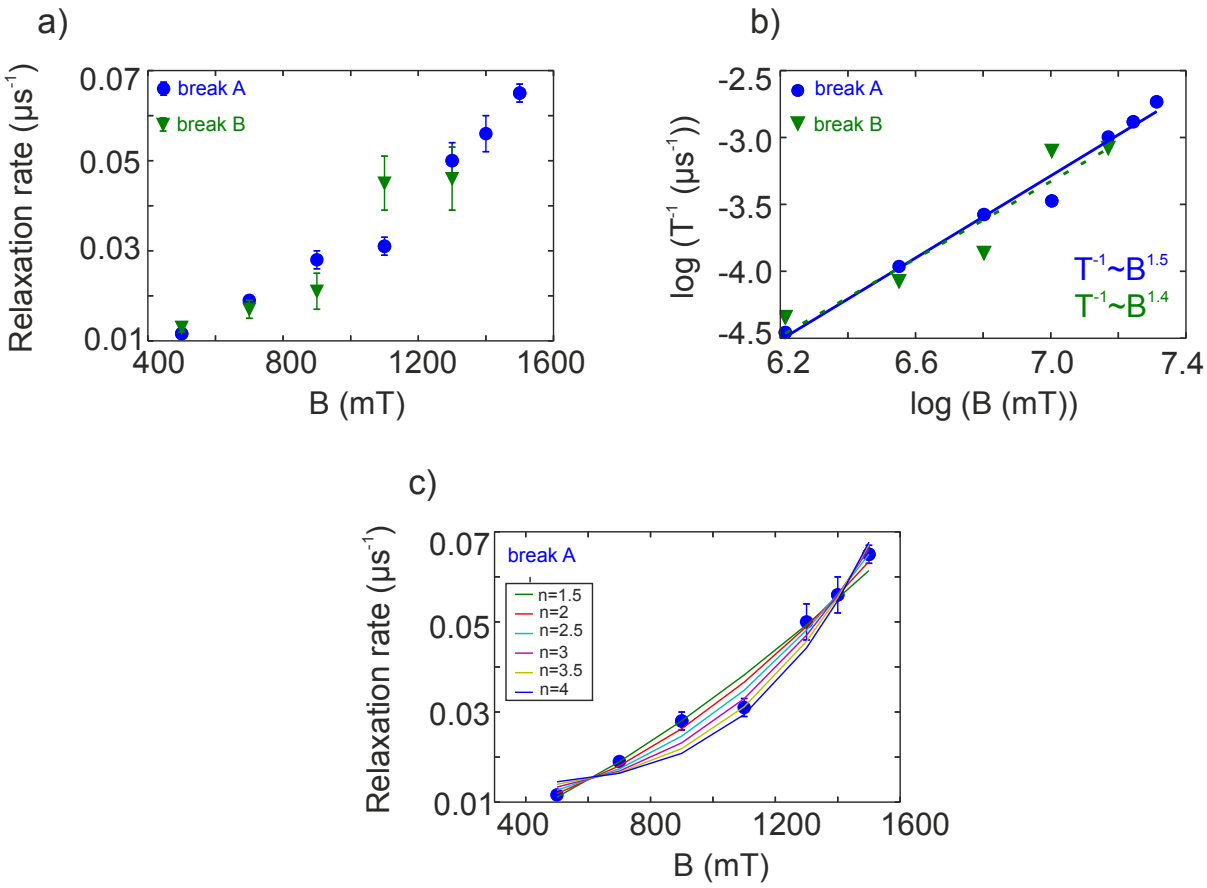

Figure 7.8: (a) Magnetic field dependence of the hole spin relaxation rate T_1^{-1} for the break A (blue circles) and break B (green triangles). (b) Log-log plot of the spin relaxation rate vs magnetic field for the break A (blue circles) and break B (green triangles), together with the linear fits (break A: blue solid line, break B: green dashed line). The extracted slope of 1.5 ± 0.1 (1.4 ± 0.3) for the break A (break B) breaks gives the spin relaxation rate dependence on the magnetic field. (c) Spin relaxation rates versus magnetic field plotted together with a function $aB^n + c$, for different values of n, for the break A.

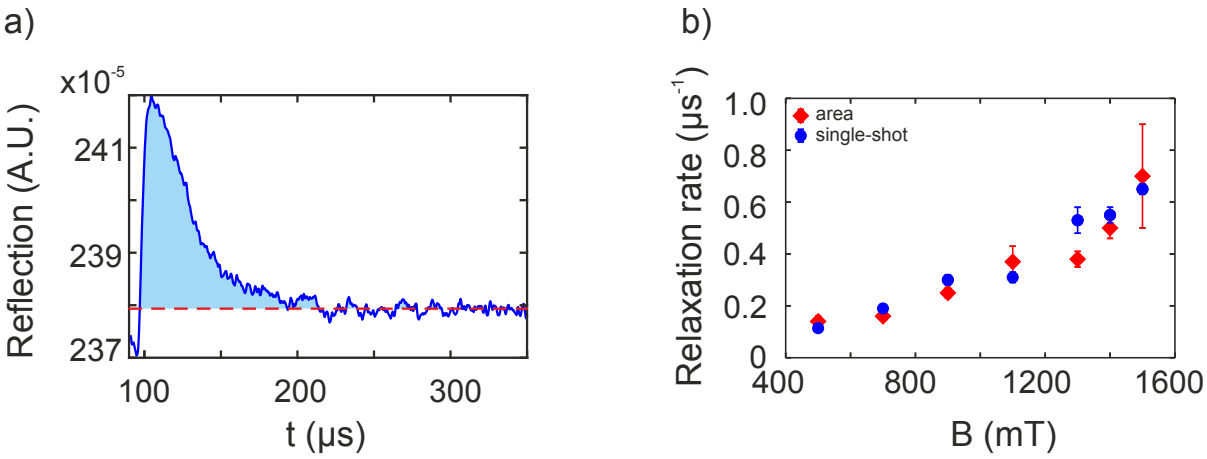

Figure 7.9: (a) Average of around 2000 single-shot traces for a loading time of 20 μs and a magnetic field of 700 mT. The integrated RA is shown in light blue. The red dashed line indicates the position where the RA saturates and it is taken as zero. (b) Magnetic field dependence of the hole spin relaxation rate T_1^{-1} for the single-shot (blue circles) and the integrated average (red diamonds) analysis.

Averaged analysis

The spin relaxation time cannot be extracted only from a single-shot analysis but also from the average value of the single-shot traces. In this way also the data with low SNR can be treated, and/or the results of the single-shot analysis can be verified.

In this analysis, for each loading time we integrate the averaged charge sensor RA (light blue area in Figure 7.9 (a)) during the read phase of around 2000 single-shot traces. The red dashed line in Figure 7.9 (a) indicates the position where the RA saturates and it is taken as a zero. Since the RA saturates, not the whole read interval was considered in the analysis. The integrated values follow as well an exponential decay as the loading time is increasing and the obtained relaxation times are in good agreement with those obtained from the single-shot analysis (Figure 7.9 (b)).

7.2.1 Deterministic loading of a spin-down state

One of the DiVincenzo criteria is to be able to deterministically initialize the quantum state. It is shown below that it is possible to deterministically load the spin-down state for an arbitrary magnetic field, and read it out accordingly. If already during the load stage the electrochemical potentials are in the configuration that $\mu_\downarrow < \mu_{SHT} < \mu_\uparrow$, only the spin-down hole can be loaded. In order to prove that, a new pulsing sequence is applied. It consists of four stages, load, plunge, read and empty. The schematic of the sequence is shown in Figure 7.10 (a). This time, the amplitude of the load stage is varied. We start with the pulse amplitude equal to the reference point (0 mV), corresponding to the case when

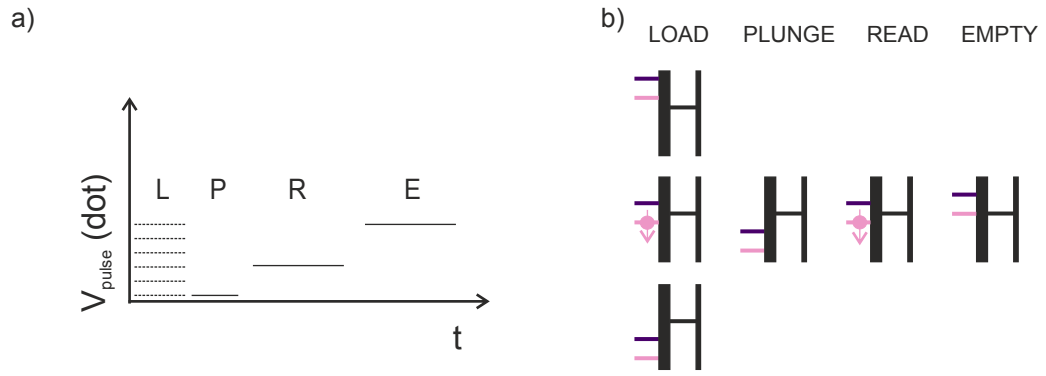

Figure 7.10: (a) Four stage pulsing sequence for proving the deterministic loading of the spin-down state. The duration of the load and the plunge stages is 10 μs and the duration of the read and the empty stages is 700 μs. (b) Diagrams showing the alignment of electrochemical potentials in the sequence for deterministic loading of the spin-down state. Again, the electron convention is used.

$\mu_\uparrow, \mu_\downarrow > \mu_{SHT}$. No hole can be loaded to the QD. As we start to apply a more negative pulse, the electrochemical potentials of the QD approach the condition when $\mu_\downarrow = \mu_{SHT}$. A hole with a spin-down will be thus deterministically loaded. With more negative load stage amplitudes, again both spin-up or a spin-down hole can be loaded ($\mu_\uparrow, \mu_\downarrow < \mu_{SHT}$). This is schematically shown in Figure 7.10 (b), first column. As before, the spin state is read out in the read stage, and finally the QD is emptied with the last stage. The additional, plunge stage, is added in order to load a hole before the read stage, if a hole has not been loaded during the load stage (cases when $\mu_\uparrow, \mu_\downarrow > \mu_{SHT}$. This ensures the unique interpretation of the SHT RA.

It is important that the duration of the load and the plunge stages is shorter than the hole spin relaxation time, but still long enough that a hole can tunnel. We decided to set the duration of the load and the plunge stages to 10 μs. It is not an ideal compromise since the hole tunnelling times are comparable with the duration of the stages, which might thus result in unsuccessful loading.

Zeeman splitting measurement

The voltage range for which only the spin-down state is loaded corresponds to the Zeeman splitting:

$$E_Z = g\mu_B B. \tag{7.1}$$

Figure 7.11 (a) shows a zoom-in into the beginning of the read stage of a four-stage pulse sequence, for a magnetic field of 500 mT, a value where the qubit would actually operate. We indeed see that for

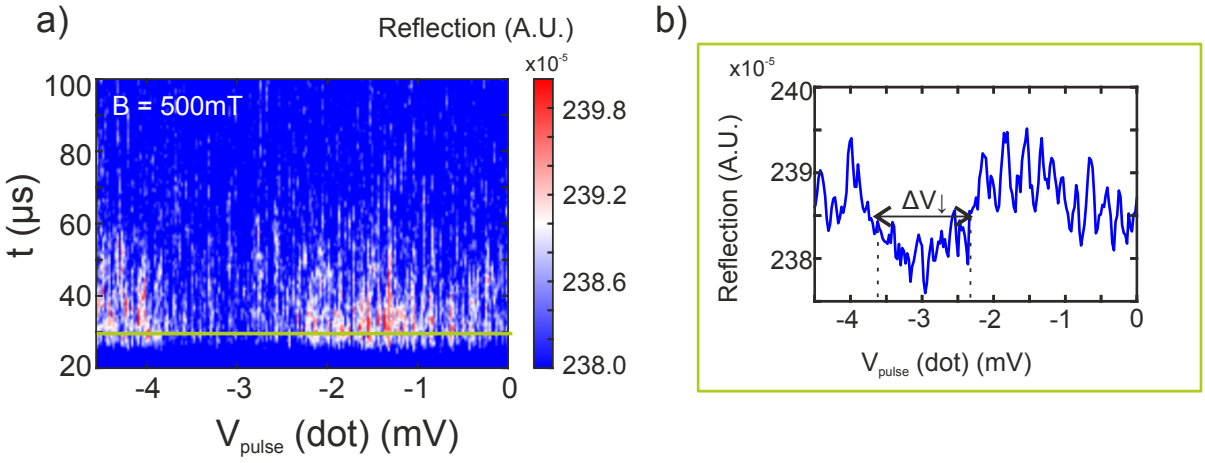

Figure 7.11: (a) Zoom into the first 80 μs of the read stage of a four-stage pulse sequence, for a magnetic field of 500 mT. The duration of the load and plunge stages was 10 μs, while that of the read and empty 700 μs. (b) Horizontal line cut along the solid green line in b), after smoothing the data with a Savitzky-Golay filter. For the voltage range for which just a spin-down hole can be loaded ($\Delta V_{\downarrow}$), the RA shows a minimum during the read stage (black double arrow).

a certain voltage range, the SHT always shows the minimum RA, due to the fact that a spin-down hole has been deterministically loaded. From the horizontal line cut at the beginning of the read stage we can extract this voltage range. In order to smooth the noisy data, we used a Savitzky-Golay filter (third order polynomial, for a window size =7).

Determining the lever arm

In order to obtain the Zeeman splitting, the voltage range $\Delta V_{\downarrow}$ for which we load only the spin the down state has to be multiplied with the lever arm α:

$$E_z = \alpha \Delta V_{\downarrow}. \tag{7.2}$$

When the value of the g-factor is known, it is easy to calculate the lever arm from relations 7.2 and 7.1. However, the hole g-factor is highly anisotropic and it greatly depends on the number of confined holes. The usual method of extracting the lever arm from a bias spectroscopy measurement can't be applied here, since our QD has no source and drain electrodes.

In similar systems [23, 82] the lever arm was extracted by mapping the occupation probability in the reservoir. In this method the SHT current is measured along a Coulomb peak break (black dashed line in Figure 7.12 (b)), for different bath temperatures T_{bath}. Due to the Fermi distribution of the states in the SHT, this transition is not a step function. The reason is the smearing out of the Fermi distribution at finite

temperatures, as some holes begin to be thermally excited to energy levels above the electrochemical potential. The width of the transition is proportional to the width of the Fermi distribution of the hole states in the SHT (7.12 (c)). The measured current can be fit to the function

$$< I_{\mathrm{SHT}} >= \frac{a}{1 + exp\left(\frac{eV_{\mathrm{eff}} - b}{c}\right)} + d, \tag{7.3}$$

where V_{eff} is the voltage of the applied diagonal pulse ($V_{\mathrm{eff}} = \sqrt{\Delta V_{\mathrm{G}}^2(\mathrm{dot}) + \Delta V_{\mathrm{G}}^2(\mathrm{sensor})}$) and a,b,c and d are fitting parameters. The fitting parameter c has units of energy and it is equal to

$$c = \alpha T_{\mathrm{bath}} k_B, \tag{7.4}$$

where k_B is Boltzmann constant, T_{bath} is the bath temperature of the dilution refrigerator and α is the lever arm. Repeating this fit for different bath temperatures gives the c/k_B dependence on T_{bath}/α. α can therefore be extracted from the slope of a linear fit, for temperature values where the bath temperature determines the hole temperature. For bath temperatures lower than the effective hole temperature the c/k_B values saturate.

We have tried to extract the lever arm with this method. At different temperatures we slowly moved along the Coulomb peak break (see Figure 7.12 (a), (b)), integrating the current value at each voltage step for 200 ms (several orders of magnitude longer than the hole tunnelling time). This experiment actually corresponds to the one described in Section 6.2.3, with the difference that here we were unloading a hole (the QD gate voltage was increasing). Despite the rather long averaging, the measurements were very noisy for higher temperatures, making the fit very challenging. To overcome this, each line trace was smoothed with the Savitzky-Golay filter (first order polynomial, for a window size =3) (see Figure 7.12 (c)). The filtering caused additional broadening of lines, making the method unreliable. Another problem we had is that the line traces look quite different when taken for slightly different V_{eff}, giving unequal c/k_B values for the same temperature. For one such set of line traces we plotted the c/k_B dependence on the T_{bath}/α (Figure 7.12 (d)). The values indeed saturate at lower temperatures (allowing a rough estimation of the effective hole temperature), but the part which should show a linear dependence has too large errors for a reliable fit.

7.3 Spin readout fidelities

To evaluate the qubit quality, it is important to estimate how accurate the spin readout mechanism is. The probability that in each single response of the SHT the spin state is assigned correctly is called

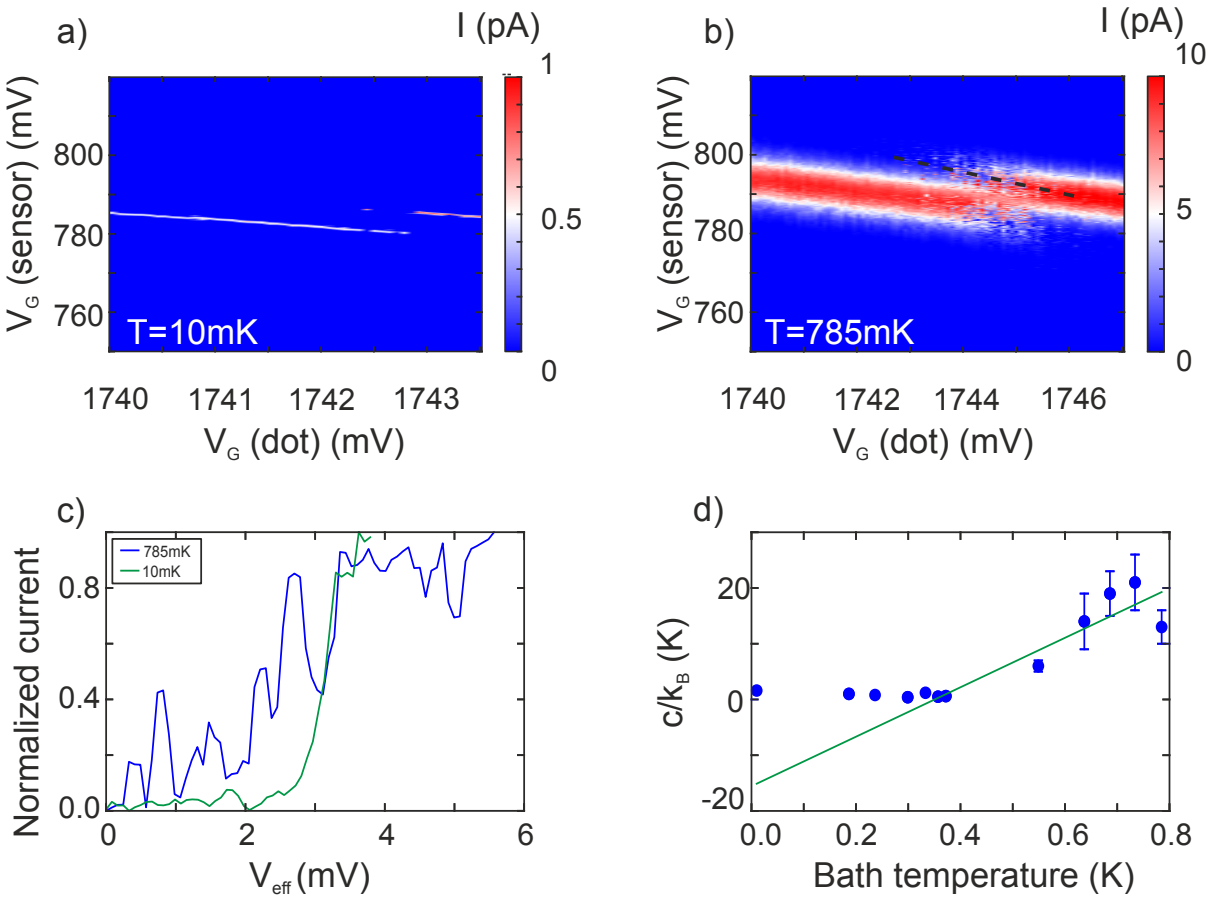

Figure 7.12: (a) Stability diagram taken at a temperature of 10 mK. (b) Stability diagram taken at a temperature of 785 mK. The black dashed line indicates where the line trace is taken. (c) Line traces after the smoothing filter was applied, for temperatures of 10 mK (green) and 785 mK (blue) (d) c/k_B dependence on the T_{bath}/α, for one set of line traces. The linear fit is shown in green. The standard deviation much larger than the value of α.

the readout fidelity. The readout fidelity will depend on both spin-to-charge conversion and charge readout fidelity. To estimate the former, we followed the procedure introduced by Elzerman et al. [79]. To estimate the latter, we followed the one introduced by Morello et al. [23]. Finally, for extracting the total fidelity we combined both.

7.3.1 Spin-to-charge conversion fidelity

The accuracy of the single-shot spin-to-charge conversion analysis greatly depends on the chosen threshold (horizontal dot-dashed red line in Figure 7.7). We performed the analysis for break A, for different values of the normalized threshold. Threshold = 1 corresponds to the average maximum SHT RA and threshold = 0 to the average minimum SHT RA, for certain magnetic field. There are two scenarios which can lead to a wrong spin-to-charge conversion and, consequently, wrong spin readout:

- The SHT RA signal exceeds the threshold even in the case of loading a spin-down hole
- The SHT RA signal stays below the threshold even in the case of loading a spin-up hole

The SHT signal exceeds the threshold even in the case of loading a spin-down hole

The probability that the SHT signal exceeds the threshold even if a spin-down hole was loaded is characterized with the parameter α. Thermally activated tunnelling processes and electrical noise contribute to it. α can be easily determined from the saturation value of the exponential fit of the spin-up fractions versus the waiting time. The probability of a wrong interpretation decreases with increasing the threshold value. We can define a spin-to-charge conversion fidelity for a spin-down as 1-α.

The SHT signal stays below the threshold even in the case of loading a spin-up hole

A spin-up hole can relax before it tunnels out. In that case, the SHT signal stays below the threshold even if a spin-up hole was loaded. The probability that this event happens is characterized with the parameter β and :

$$\beta = \frac{1}{1 + T_1 \Gamma_\uparrow}, \tag{7.5}$$

where $\Gamma_\uparrow$ is the spin-up tunnel rate. The spin-up tunnel rate $\Gamma_\uparrow$ can be calculated from the spin-up decay rate, which is equal to $(\Gamma_\uparrow + T_1^{-1})$. The spin-up decay rate is obtained from the fit to the histogram representing the detection times of the spin-up hole. The detection time $t_\uparrow$(det) is the time from the beginning of the read stage to the moment when the spin-up is detected (labelled with the purple double arrow in Figure 7.7). The fit to the histogram of the detection times for a magnetic field of 500 mT and the threshold = 0.70 is shown in Figure 7.14 (a). As a remark, both T_1^{-1} and $t_\uparrow$(det) are threshold dependent. We can define a spin-to-charge conversion fidelity for a spin-up as 1-β.

The spin-to-charge conversion fidelity for the spin-down hole (1-α) is 0.833 ± 0.005 while for the spin-up hole (1-β) it is 0.907 ± 0.007, giving a maximum spin-to-charge conversion visibility (1- α - β) of 0.740 ± 0.009 for the normalized threshold of 0.7 (Figure 7.13 (a)).

In order to get a better understanding into the factors limiting the spin-to-charge conversion fidelities for holes, the dependence of α and β on the magnetic field was investigated (Figure 7.13 (b)). While α tends to decrease for larger magnetic fields, β shows the opposite behaviour. This leads to a maximum total spin-to-charge conversion visibility of 0.81 ± 0.01 at 700 mT (Figure 7.13 (c)). α implies mainly a

failure of the spin-down hole to remain in the QD. The tunnel-out time of the spin-down state and thus 1-α depends on the ratio of the magnetic field and the effective hole temperature (EHT) [77]. One solution for increasing 1-α is to increase the magnetic field. However, larger magnetic fields imply short spin relaxation times and large qubit operation frequencies. The optimal solution is to keep the magnetic field at low values and decrease the effective hole temperature. Since the reported experiment was performed at an EET of about 300-400 mK (Figure 7.12 (d)), fidelities 1-α higher than 0.95 should be feasible at magnetic fields of about 200 mT for an EHT of 100 mK.

We now turn our attention to β. As $\Gamma_{\uparrow}$ is rather insensitive to the magnetic field (Figure 7.13 (d)) , the increase of β originates from the drastically reduced spin relaxation times. Taking into account the predicted $B^{3/2}$ dependence of the spin relaxation rate, relaxation times exceeding 0.3 ms should be feasible at 200 mT. This is in line with the values reported for core-shell wires at low magnetic fields [30]. Such longer spin relaxation times will allow 1-β to exceed 0.95. From the above discussion it becomes clear that the main difference of hole spins compared to electron spins lays in β. While α for electron spins is as well limited by the magnetic field value [77], this is not the case for β. For electron spins the spin relaxation time is in the order of seconds even at fields exceeding 1 T [23, 77], which in combination with the short tunnelling times makes β rather insensitive to the value of the magnetic field.

7.3.2 Charge readout fidelity

After the spin-to-charge conversion process, the charge is read out with the SHT. If the measurement bandwidth is too low, the resulting RA square response (Figure 7.3 (b)) cannot be detected (see Figure 6.17), leading to the wrong interpretation of a spin state. This can be quantified with the fidelity of the charge readout mechanism, which we estimated following the method introduced by Morello et al [23]. In essence, we performed a simulation which resulted in a bimodal distribution of the RA peaks. This bimodal distribution was then compared to the experimental data and it allowed the extraction of the spin-up and spin-down charge readout fidelity as will be seen below. This simulation was performed by J. Milem, a first year student of the group.

The model consisted of the following steps:

(i) Randomly assign a spin state

If the spin is in the excited state (spin-up), generate a pulse with a height which corresponds to the experimental RA. Its width was determined by the experimentally extracted tunneling times: the tunnelling-out time of a spin-up hole ($t_{\uparrow,out}$) and the tunnelling-in time of a spin-down hole ($t_{\downarrow,in}$) [23]. The former can be extracted from the fit to the histogram (Figure 7.14 (a)) representing the detection times of the spin-up hole ($t_{\uparrow}$(det) in Figure 7.7), where $t_{\uparrow}$(det) is equal to $1/\Gamma_{\uparrow}$ +

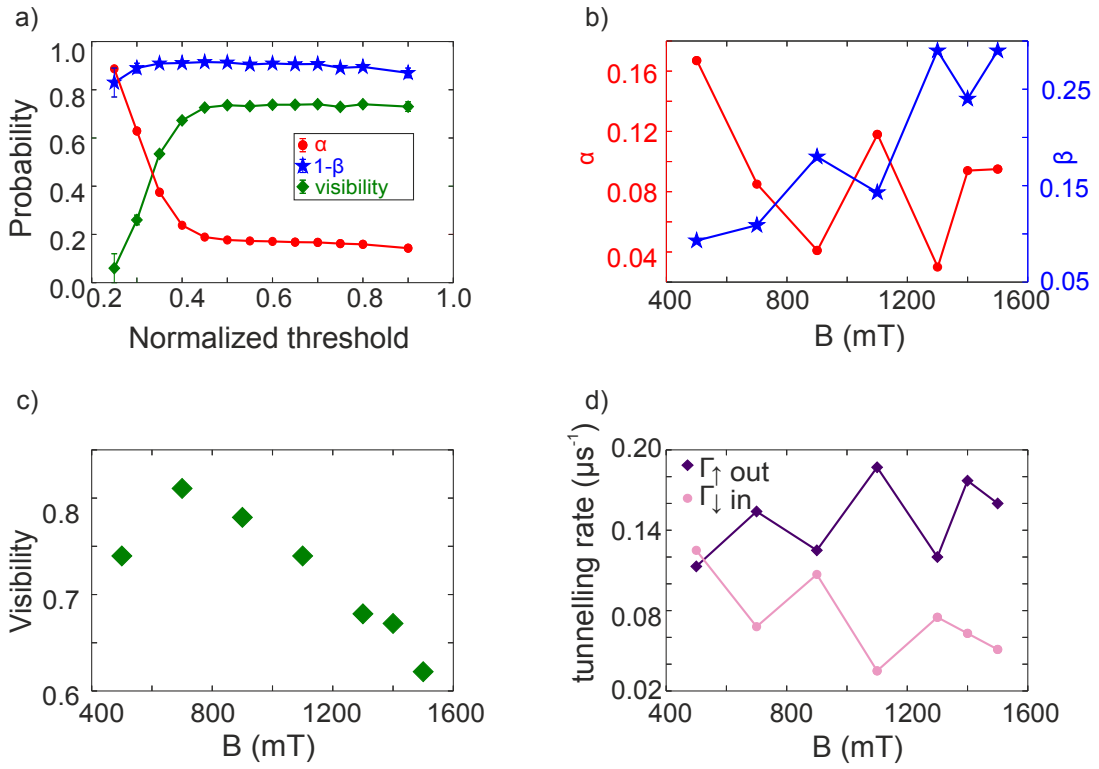

Figure 7.13: (a) Spin-to-charge conversion fidelity: Dependence of α, 1-β and the visibility on the normalized threshold, at B = 500 mT. (b) Magnetic field dependence of α (red dots) and β (blue stars) parameters, extracted for the threshold which gives the maximum spin-to-charge conversion visibility. (c) Magnetic field dependence of the spin-to-charge visibility. (d) Magnetic field dependence of the spin-up tunnelling-out rates (purple diamonds) and the spin-down tunnelling-in rates (pink circles).

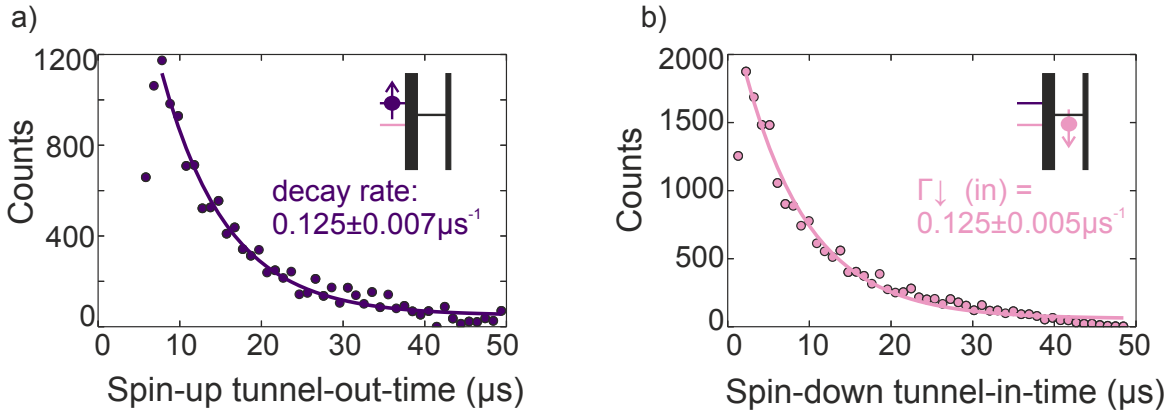

Figure 7.14: (a) Histogram and exponential fit of the detection times for spin-up holes. (b) Histogram and exponential fit of the tunnelling-in times for spin-down holes.

T_1^{-1}). The exponential fit gives a decay rate $t_\uparrow(\mathrm{det})^{-1}$ equal to $(0.125 \pm 0.007)\,\mu s^{-1}$, which gives us finally $\Gamma_{\uparrow,out} = (0.113 \pm 0.007)\,\mu s^{-1}$. $\Gamma_{\downarrow,in}$ is extracted from the fit to the histogram (Figure 7.14 (b)) representing the peak widths ($t_\downarrow$(det) in Figure 7.7): $\Gamma_{\downarrow,in} = (0.125 \pm 0.005)\,\mu s^{-1}$. All values

are extracted for the normalized threshold = 0.70.

After the pulse was generated, Gaussian noise was added to this trace with the noise amplitude being a free parameter.

If the spin is in the ground state (spin-down), no pulse is generated; only Gaussian noise is added to the trace.

(ii) Application of a numerical filter of 4th order to the above trace.

(iii) Extraction of the peak value of the reflection amplitude. This value was then added to an array which was corresponding either to a spin-down or spin-up state.

(iv) Steps (i)-(iii) were repeated for 100000 times.

(v) From each array a histogram was created. Before a weighting function for each of the two arrays was generated in order to normalize the data (for each array the total probability should be one).

(vi) An optimal Gaussian function was found for each of the two calculated histograms, giving the spin-up ($N_{\uparrow}$) and the spin-down probabilities ($N_{\downarrow}$).

In order to be able to compare the two simulated Gaussian functions with the experimental data, a histogram of the experimental reflection amplitude peak values was plotted. Also here the data were normalized. Two optimized Gaussian functions were fitted to the bimodal experimental distribution. Those were then compared to the two Gaussian functions obtained from the model (Figure 7.15 (a)). The charge readout fidelities as a function of the threshold value shown in Figure 7.15 (b) can be extracted from

$$\begin{aligned} F_{\downarrow} &= 1 - \int_{threshold}^{\inf} N_{\downarrow}(RA)dRA \\ F_{\uparrow} &= 1 - \int_{-\inf}^{threshold} N_{\uparrow}(RA)dRA, \end{aligned} \tag{7.6}$$

where $F_{\downarrow}$ is the charge readout fidelity for a spin-down state and $F_{\uparrow}$ is a charge readout fidelity for a spin-up state. The fidelity of each spin state is limited by the total number of counts which have leaked into the opposite spin Gaussian distribution.

Ultimately, the total readout fidelity is given by

$$\begin{aligned} F_{\downarrow tot} &= (1-\alpha)F_{\downarrow} \\ F_{\uparrow tot} &= (1-\beta)F_{\uparrow}, \end{aligned} \tag{7.7}$$

for a spin-down and a spin-up state, respectively.

The maximal visibility of $F_{\downarrow tot}+F_{\uparrow tot}-1$ = 0.691$\pm$0.008 is obtained for a threshold of 0.70, giving measurement fidelities for spin-down of 0.801$\pm$0.005 and 0.889$\pm$0.007 for a spin-up state (Figure 7.16).

For the same threshold, the charge readout visibility $F_{\downarrow} + F_{\uparrow} - 1$ (Figure 7.15 (b)) is equal to 0.942. This result indicates that the limitation in our experiments comes from the spin-to-charge conversion, and not from the charge readout. There are two main processes which can limit the fidelity of the spin-to-charge conversion: i) the excited spin state relaxes before tunnelling out and ii) the ground spin state tunnels out of the QD due to thermal broadening of the Fermi distribution in the SHT. Compared to the experiments reported for electrons in Si the first process is clearly more pronounced for the hole spins as the ratio between T_1 and $t_{\uparrow,out}$ is significantly lower. In addition, as has been shown before, as the effective hole temperature in the experiment was relatively high the second limitation can be easily improved by improving the filtering in the dilution refrigerator.

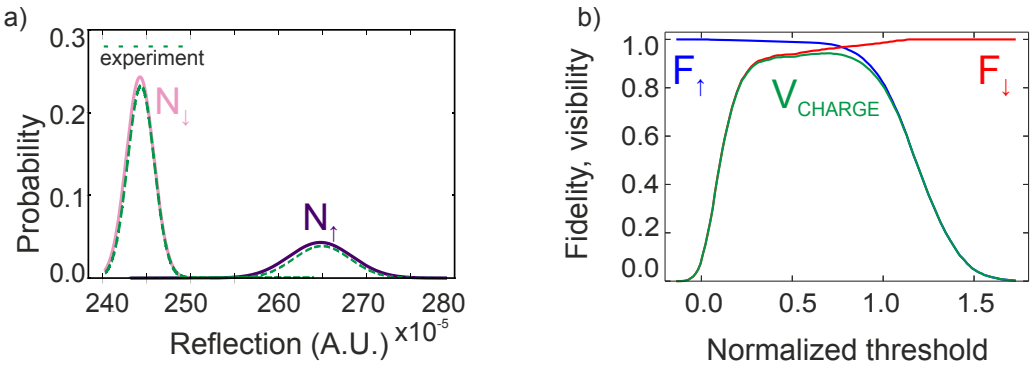

Figure 7.15: (a) Histogram of the maximum RA values (green dashed line) obtained from the experimental data for the 50μs analysis interval. The best fit simulated histograms for the spin-up (purple) and spin-down (pink) states have been superimposed. (b) Calculated spin-up (blue line), spin-down (red line) fidelities and the charge readout visibility (green line). The normalized threshold is exceeding 1.0 as there are RA values exceeding the average maximum value.

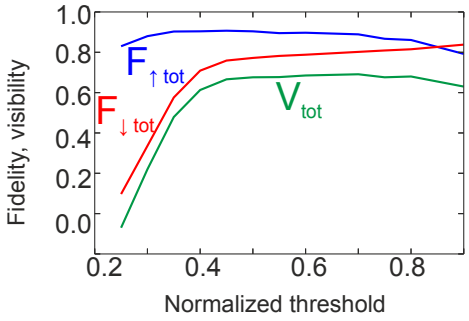

Figure 7.16: Total readout spin-down fidelity ($F_{\downarrow tot}$ = (1-α)*$F_{\downarrow}$, red), spin-up ($F_{\uparrow tot}$ = (1-β)*$F_{\uparrow}$, blue) fidelity and the total readout visibility ($F_{\downarrow tot} + F_{\uparrow tot} - 1$, green).

7.3.3 Peculiarities in the experiment

During the read stage in the spin readout protocol, the RA square signal (see Figure 7.3 (c)) corresponding to the initially loaded spin-up hole should appear only once. When the spin-up hole gets replaced with the spin-down hole (see Figure 7.2), the SHT should always show minimum RA. However, sometimes we see additional signals, which are referred here as *multi-blips*, shown also in other works [84]. Further tunnel events may occur due to the finite temperature, although we are not sure that this is the only mechanism responsible for the multi-blips. Figure 7.17 shows multi-blips in the read stage at B = 500 mT.

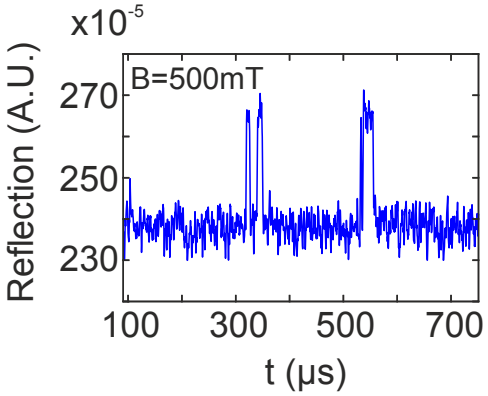

Figure 7.17: Example of multi-blip events occurring in the read stage.

The existence of multi-blips can affect the data analysis. Therefore, it is important to choose the right duration of the read interval for the analysis. Figure 7.18 shows how T_1 and parameter α change when the read interval is too long. It can be seen that multi-blips do not affect much the extracted relaxation time (Figure 7.18 (a)). In our main data analysis we already took care of that by taking the read interval such that majority of the tunnel-out events had happened (50 μs). However, parameter α is strongly affected, as can be seen in Figure 7.18 (b). In addition, for long read intervals, α decreases with magnetic field. This indicates that the temperature broadening of the SHT levels influences multi-blips, as for higher magnetic fields the spin-up and down states in the QD are further apart and thus less influenced by thermal broadening.

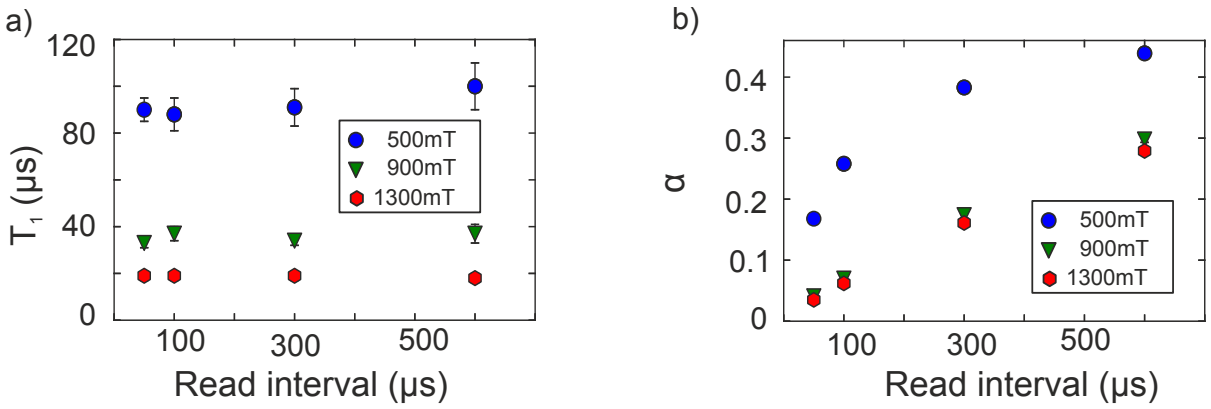

Figure 7.18: (a) Hole spin relaxation times extracted for different read intervals and for three different magnetic fields. (b) Parameter α extracted for different read intervals and for three different magnetic fields.

8 Conclusion and outlook

During this Thesis we established a reproducible recipe for fabricating SHTs both for dome islands and hut wires. We used the fact that hut wires grow in only two crystallographic orientations, perpendicular to each other, in order to create a device out of a T-like structure. A QD formed in one HW can act as a spin qubit and it can be tuned with a gate electrode. Out of the second HW we fabricated a complete SHT. Such a structure allowed the realization of a charge sensor, which was electrostatically and tunnel coupled to the QD, with a charge transfer signal as high as 0.3 e. Such charge transfer signals were thus observable even at 1.5 K.

Since our initial goal was to extract the hole spin relaxation time, we wanted to verify that we are able to do so with our device and setup. Due to the strong spin-orbit coupling in Ge, which in general leads to shorter relaxation times, we integrated the charge sensor into a radio-frequency reflectometry setup. We were able to perform single-shot reflectometry measurements and observe single-hole tunnelling events. We extracted the hole tunnelling times, which were found to be shorter than 10 μs. This result paved the way towards spin readout measurements, since we had all necessary ingredients: charge sensing, high bandwidth setup and short enough tunnelling times.

Afterwards we demonstrated for the first time single-shot spin readout measurements for holes. We extracted hole spin relaxation times of about 90 μs at 500 mT, with a readout visibility of 70%.

As expected, the observed the spin relaxation rate increased with increasing magnetic field. However, the magnetic field dependence differed from the one observed for electrons in GaAs and Si. The strain in the valence band leads to a hole-phonon Hamiltonian which depends both on the spin and the phonons, responsible for the spin relaxation. This is different from the conduction band where the electron-phonon interaction does not depend on the spin.

The results reported in this thesis constitute a first important step towards the realization of more complex qubit devices in Ge hole QDs.

Future work

The measurements on the Ge HWs devices presented in this thesis were first demonstrations of relaxation experiments in such systems. That means that many things can be further optimized and studied in more detail. Besides that, we are still lacking the recipe for electrically cleaner devices. Such would allow, for instance, systematic investigations of how the relaxation time varies with the number of confined holes.

To give a long-term outlook, I will turn back to DiVicenzo's criteria. One of them is related to a readout mechanism with high fidelity. We could obtain higher hole spin readout fidelities by lowering the effective hole temperature, since we still have room for improvement of our setup. A lower hole effective temperature would allow us to do the spin readout at lower magnetic fields, implying also longer T_1. In addition, for such fields qubit operations could be performed with frequencies, lower than 20 GHz.

There is still a long way to go to couple such qubits at a distance. However, operation of qubits at lower magnetic fields would also allow coupling via superconducting resonators.

Finally, Ge hut wires are good candidates for realizing scalable architectures. They can be grown on prepatterned substrates and first devices have already been measured in our group.

All ingredients for a scalable, reliable and fast qubit system are here, waiting to be implemented.

Bibliography

[1] N. D. Mermin, *Quantum computer science*. Cambridge University Press, 2007. (Cited on page 1)

[2] M. A. Nielsen and I. L. Chuang, *Quantum computation and quantum information*. Cambridge University Press, 10th edition ed., 2010. (Cited on page 1)

[3] "http://www.research.ibm.com/ibm-q/learn/quantum-computing-applications/." Accessed April 2018. (Cited on page 1)

[4] "https://www.microsoft.com/en-us/research/wp-content/uploads/2015/03/matthias-troyer-quantum-applications.pdf." Accessed April 2018. (Cited on page 1)

[5] J. L. O. O'Brien, A. Furusawa, and Vučković, "Photonic quantum technologies," *Nature Photonics*, vol. 3, pp. 687–695, 2009. (Cited on page 1)

[6] R. Blatt and D. Wineland, "Entangled states of trapped atomic ions," *Nature*, vol. 453, pp. 1008–1015, 2008. (Cited on page 2)

[7] C. Monroe and J. Kim, "Scaling the ion trap quantum processor," *Science*, vol. 339, pp. 1164–1169, 2013. (Cited on page 2)

[8] G. Wendin, "Quantum information processing with superconducting circuits: a review," *Rep. Prog. Phys*, vol. 80, no. 106001, 2017. (Cited on page 2)

[9] D. Loss and D. P. DiVincenzo, "Quantum computation with quantum dots," *Phys. Rev. A*, vol. 57, p. 120, Jan. 1998. (Cited on pages 2 and 3)

[10] D. P. DiVincenzo, "The physical implementation of quantum computation," *Fortschr. Phys.*, vol. 48, pp. 771–783, 2000. (Cited on page 2)

[11] P. W. Shor, "Scheme for reducing decoherence in quantum computer memory," *Phys. Rev. A*, vol. 52, p. R2493(R), 1995. (Cited on page 2)

[12] A. M. Steane, "Error correcting codes in quantum theory," *Phys. Rev. Lett.*, vol. 77, p. 793, 1996. (Cited on page 2)

[13] F. H. L. Koppens, C. Buizert, K. J. Tielrooij, I. T. Vink, K. C. Nowack, T. Meunier, L. P. Kouwenhoven, and L. M. K. Vandersypen, “Driven coherent oscillations of a single electron spin in a quantum dot,” *Nature*, vol. 442, pp. 766–771, 2006. (Cited on page 2)

[14] J. Petta, A. Johnson, J. Taylor, E. Laird, A. Yacoby, M. Lukin, C. Marcus, M. Hanson, and A. Gossard, “Coherent manipulation of coupled electron spins in semiconductor quantum dots,” *Science*, vol. 309, pp. 2180–2184, 2005. (Cited on page 2)

[15] J. Medford, J. Beil, J. M. Taylor, S. D. Bartlett, A. C. Doherty, E. I. Rashba, D. P. DiVincenzo, H. Lu, A. C. Gossard, and C. M. Marcus, “Self-consistent measurement and state tomography of an exchange-only spin qubit,” *Nature Nanotechnology*, vol. 8, pp. 654–659, 2013. (Cited on page 2)

[16] M. V. Gurudev Dutt, L. Childress, L. Jiang, E. Togan, J. Maze, F. Jelezko, A. S. Zibrov, P. R. Hemmer, and M. D. Lukin, “Quantum register based on individual electronic and nuclear spin qubits in diamond,” *Science*, vol. 316, pp. 1312–1316, 2007. (Cited on page 2)

[17] G. D. Fuchs, G. Burkard, P. V. Klimov, and D. D. Awschalom, “A quantum memory intrinsic to single nitrogenâĂŞvacancy centres in diamond,” *Nature Physics*, vol. 7, pp. 789–793, 2011. (Cited on page 2)

[18] L. Robledo, L. Childress, H. Bernien, B. Hensen, P. F. A. Alkemade, and R. Hanson, “High-fidelity projective read-out of a solid-state spin quantum register,” *Nature*, vol. 477, pp. 574–578, 2011. (Cited on page 2)

[19] B. E. Kane, “A silicon-based nuclear spin quantum computer,” *Nature*, vol. 393, pp. 133–137, 1998. (Cited on page 2)

[20] J. T. Muhonen, J. P. Dehollain, A. Laucht, F. E. Hudson, R. Kalra, T. Sekiguchi, K. M. Itoh, D. N. Jamieson, J. C. McCallum, A. S. Dzurak, and A. Morello, “Storing quantum information for 30 seconds in a nanoelectronic device,” *Nature Nanotechnology*, vol. 9, pp. 986–991, 2014. (Cited on page 2)

[21] A. Laucht, R. Kalra, S. Simmons, J. P. Dehollain, J. T. Muhonen, F. A. Mohiyaddin, S. Freer, F. E. Hudson, K. M. Itoh, D. N. Jamieson, J. C. McCallum, A. S. Dzurak, and A. Morello, “A dressed spin qubit in silicon,” *Nature Nanotechnology*, vol. 12, pp. 61–66, 2017. (Cited on page 2)

[22] P. Becker, H. J. Pohl, H. Riemann, and N. Abrosimov, “Enrichment of silicon for a better kilogram,” *Physica Status Solidi A*, vol. 207, pp. 49–66, 2010. (Cited on page 2)

[23] A. Morello, J. J. Pla, F. A. Zwanenburg, K. W. Chan, K. Y. Tan, H. Huebl, M. Möttönen, C. D. Nugroho, C. Yang, J. A. van Donkelaar, A. D. C. Alves, D. N. Jamieson, C. C. Escott, L. C. L.

Hollenberg, R. G. Clark, and A. S. Dzurak, “Single-shot readout of an electron spin in silicon,” *Nature*, vol. 467, pp. 687–691, 2010. (Cited on pages 2, 3, 38, 41, 66, 70, 72, and 74)

[24] B. M. Maune, M. G. Borselli, B. Huang, T. D. Ladd, P. W. Deelman, K. S. Holabird, A. A. Kiselev, I. Alvarado-Rodriguez, R. S. Ross, A. E. Schmitz, M. Sokolich, C. A. Watson, M. F. Gyure, and A. T. Hunter, “Coherent singlet-triplet oscillations in a silicon-based double quantum dot,” *Nature*, vol. 481, pp. 344–347, 2012. (Cited on page 2)

[25] C. B. Simmons, J. Prance, B. Van Bael, T. Koh, Z. Shi, D. Savage, M. Lagally, R. Joynt, M. Friesen, S. Coppersmith, and M. Eriksson, “Tunable spin loading and t_1 of a silicon spin qubit measured by single-shot readout,” *Phys. Rev. Lett.*, vol. 106, p. 156804, Apr. 2011. (Cited on page 2)

[26] J. Yoneda, K. Takeda, T. Otsuka, T. Nakajima, M. R. Delbecq, G. Allison, T. Honda, T. Kodera, S. Oda, Y. Hoshi, N. Usami, K. M. Itoh, and S. Tarucha, “A quantum-dot spin qubit with coherence limited by charge noise and fidelity higher than 99.9pp. 102–106, 2018. (Cited on page 3)

[27] X.-J. Hao, T. Tu, G. Cao, C. Zhou, H.-O. Li, G.-C. Guo, W. Y. Fung, Z. Ji, G.-P. Guo, and W. Lu, “Strong and tunable spin-orbit coupling of one-dimensional holes in ge/si core/shell nanowires,” *Nano Lett.*, vol. 10, pp. 2956–2960, 2010. (Cited on page 3)

[28] A. P. Higginbotham, F. Kuemmeth, T. W. Larsen, M. Fitzpatrick, J. Yao, H. Yan, C. M. Lieber, and C. M. Marcus, “Antilocalization of coulomb blockade in ge/si nanowire,” *Phys. Rev. Lett.*, vol. 112, p. 216806, 2014. (Cited on page 3)

[29] C. Kloeffel, M. J. Rančić, and D. Loss, “Direct rashba spin-orbit interaction in si and ge nanowires with different growth directions,” *Preprint at https://arxiv.org/pdf/1712.03476.pdf*, 2017. (Cited on page 3)

[30] Y. Hu, F. Kuemmeth, C. M. Lieber, and C. M. Marcus, “Hole spin relaxation in ge-si core-shell nanowire qubits,” *Nature Nanotechnology*, vol. 7, pp. 47–50, 2012. (Cited on pages 3 and 74)

[31] A. P. Higginbotham, T. W. Larsen, J. Yao, H. Yan, C. M. Lieber, C. M. Marcus, and F. Kuemmeth, “Hole spin coherence in a ge/si heterostructure nanowire,” *Nano Lett.*, vol. 14, pp. 3582–3586, 2014. (Cited on page 3)

[32] R. Maurand, X. Jehl, D. Kotekar-Patil, A. Corna, H. Bohuslavskyi, R. Laviéville, L. Hutin, S. Barraud, M. Vinet, M. Sanquer, and S. De Franceschi, “A cmos silicon spin qubit,” *Nature Comm.*, vol. 7, p. 13575, 2016. (Cited on page 3)

[33] H. Watzinger, C. Kloeffel, L. Vukušić, M. Rossel, V. Sessi, J. Kukučka, R. Kirchschlager, E. Lausecker, A. Truhlar, M. Glaser, A. Rastelli, A. Fuhrer, D. Loss, and G. Katsaros, “Heavy-hole states

in germanium hut wires," *Nano Lett.*, vol. 16, pp. 6879–6885, 2016. (Cited on pages 3, 5, 11, 64, and 65)

[34] J. Fischer, W. A. Coish, D. V. Bulaev, and D. Loss, "Spin decoherence of a heavy hole coupled to nuclear spins in a quantum dot," *Phys. Rev. B*, vol. 78, p. 155329, 2008. (Cited on pages 3 and 10)

[35] J. J. Zhang, G. Katsaros, F. Montalenti, D. Scopece, R. O. Rezaev, C. Mickel, B. Rellinghaus, L. Miglio, S. De Franceschi, A. Rastelli, and O. G. Schmidt, "Monolithic growth of ultrathin ge nanowires on si(001)," *Phys. Rev. Lett.*, vol. 109, p. 085502, 2012. (Cited on pages 3 and 5)

[36] H. Watzinger, J. Kukučka, L. Vukušić, F. Gao, T. Wang, F. Schäffler, J. J. Zhang, and G. Katsaros, "Ge hole spin qubit," *Preprint at https://arxiv.org/pdf/1802.00395.pdf*, 2018. (Cited on page 3)

[37] M. Veldhorst, C. H. Yang, J. C. C. Hwang, W. Huang, J. P. Dehollain, J. T. Muhonen, S. Simmons, A. Laucht, F. E. Hudson, K. M. Itoh, A. Morello, and A. S. Dzurak, "A two-qubit logic gate in silicon," *Nature*, vol. 526, pp. 410–414, 2015. (Cited on page 3)

[38] D. M. Zajac, A. J. Sigillito, M. Russ, F. Borjans, J. M. Taylor, G. Burkard, and J. R. Petta, "Resonantly driven cnot gate for electron spins," *Science*, vol. 359, no. 6374, pp. 439–442, 2018. (Cited on page 3)

[39] T. F. Watson, S. G. J. Philips, E. Kawakami, D. R. Ward, P. Scarlino, M. Veldhorst, D. E. Savage, M. G. Lagally, M. Friesen, S. N. Coppersmith, M. A. Eriksson, and L. M. K. Vandersypen, "A programmable two/qubit quantum processor in silicon," *Nature*, 2018. (Cited on page 3)

[40] N. Samkharadze, G. Zheng, N. Kalhor, D. Brousse, A. Sammak, U. C. Mendes, A. Blais, G. Scappucci, and L. M. K. Vandersypen, "Strong spin-photon coupling in silicon," *Science*, vol. 25, 2018. (Cited on page 3)

[41] X. Mi, M. Benito, S. Putz, D. M. Zajac, J. M. Taylor, G. Burkard, and J. R. Petta, "A coherent spin-photon interface in silicon," *Nature*, vol. 555, pp. 599–603, 2018. (Cited on page 3)

[42] J. Stangl, V. Holý, and G. Bauer, "Structural properties of self-organized semiconductor nanostructures," *Rev. Mod. Phys.*, vol. 76, pp. 725–783, 2004. (Cited on page 5)

[43] A. Rastelli, *Structural evolution of nanoscopic islands of Ge and SiGe on Si(001)*. PhD thesis, Universitá degli Studi di Pavia, Dipartimento di Fisica A. Volta, 2002. (Cited on page 5)

[44] H. Watzinger, M. Glaser, J. J. Zhang, I. Daruka, and F. Schäffler, "Influence of composition and substrate miscut on the evolution of $\{105\}$ - terminated in-plane si$_{\{1-x\}}$ ge$_x$ quantum wires on si(001)," *APL Mater.*, vol. 2, p. 076102, 2014. (Cited on page 5)

[45] J. Xiang, W. Lu, Y. Hu, Y. Wu, H. Yan, and C. M. Lieber, "Ge/si nanowire heterostructure as high-performance field-effect transistor," *Nature*, vol. 441, pp. 489–493, 2006. (Cited on page 6)

[46] O. G. Schmidt, ed., *Lateral alignment of epitaxial quantum dots*. Springer, 2007. (Cited on page 6)

[47] Z. Zhong and G. Bauer, "Site-controlled and size-homogeneous ge iisland on prepatterned si (001) substrates," *Appl. Phys. Lett.*, vol. 84, p. 1922, 2004. (Cited on page 6)

[48] J. J. Zhang, M. Stoffel, A. Rastelli, O. G. Schmidt, V. Jovanović, L. K. Nanver, and G. Bauer, "Sige growth on patterned si(001) substrates: surface evolution and evidence of modified island coarsening," *Appl. Phys. Lett.*, vol. 91, p. 173115, 2007. (Cited on page 6)

[49] A. I. Yakimov, A. V. Dvurechenskii, A. I. Nikiforov, A. A. Bloshkin, A. V. Nenashev, and V. A. Volodin, "Electronic states in ge/si quantum dots with type-ii band alignment initiated by space-charge spectroscopy," *Phys. Rev. B*, vol. 73, p. 115333, 2006. (Cited on page 7)

[50] J. H. Davies, *The physics of low-dimensional semiconductors*. Cambridge University Press, 1998. (Cited on page 8)

[51] P. Y. Yu and M. Cardona, *Fundamentals of semiconductors*. Springer, 4th edition ed., 2010. (Cited on pages 8 and 9)

[52] C. P. Slichter, *Principles of magnetic resonance*. Springer, 1989. (Cited on page 9)

[53] R. Winkler, *Spin-Orbit Coupling Effects in Two-Dimensional Electron and Hole Systems*. Springer, 2003. (Cited on page 9)

[54] A. V. Khaetskii and Y. V. Nazarov, "Spin-flip transitions between zeeman sublevels in semiconductor quantum dots," *Phys. Rev. B*, vol. 64, p. 125316, 2001. (Cited on page 9)

[55] V. N. Golovach, M. Borhani, and D. Loss, "Electric-dipole-induced spin resonance in quantum dots," *Phys, Rev. B*, vol. 74, p. 165319, 2006. (Cited on page 9)

[56] C. Kloeffel, M. Trif, and D. Loss, "Strong spin-orbit interaction and helical hole states in ge/si nanowires," *Phys. Rev. B*, vol. 84, p. 195314, 2011. (Cited on page 9)

[57] E. A. Chekhovich, M. N. Makhonin, A. I. Tartakovskii, A. Yacoby, H. Bluhm, K. C. Nowack, and L. M. K. Vandersypen, "Nuclear spin effects in semiconductor quantum dots," *Nature Materials*, vol. 12, pp. 494–504, 2013. (Cited on page 10)

[58] C. Testelin, F. Bernadot, B. Eble, and M. Chamarro, "Hole-spin dephasing time associated with hyperfine interaction in quantum dots," *Phys, Rev. B*, vol. 79, p. 195440, 2009. (Cited on page 10)

[59] S. Sapmaz, P. Jarillo-Herrero, L. P. Kouwenhoven, and H. S. J. van der Zant, "Quantum dots in carbon nanotubes," *Semicond. Sci. Technol.*, vol. 21, p. S52, 2006. (Cited on page 13)

[60] L. P. Kouwenhoven, D. G. Austing, and S. Tarucha, "Few-electron quantum dots," *Rep. Prog. Phys.*, vol. 64, p. 701, 2001. (Cited on page 13)

[61] T. Ihn, *Semiconductor nanostructures*. Oxford University Press, 2010. (Cited on pages 14 and 19)

[62] F. A. Zwanenburg, A. S. Dzurak, A. Morello, M. Y. Simmons, L. C. L. Hollenberg, G. Klimeck, S. Rogge, S. N. Coppersmith, and M. A. Eriksson, "Silicon quantum electronics," *Rev. Mod. Phys.*, vol. 85, pp. 961–1019, 2013. (Cited on pages 15 and 16)

[63] S. De Franceschi, S. Sasaki, J. M. Elzerman, W. G. van der Wiel, S. Tarucha, and L. P. Kouwenhoven, "Electron cotunneling in a semiconductor quantum dot," *Phys. Rev. Lett.*, vol. 86, p. 878, 2001. (Cited on page 17)

[64] D. Goldhaber-Gordon, H. Shtrikman, D. Mahalu, D. Abusch-Magder, U. Meirav, and M. A. Kastner, "Kondo effect in a single-electron transistor," *Nature*, vol. 391, pp. 156–159, 1998. (Cited on pages 18 and 27)

[65] O. Klochan, A. P. Micolich, A. R. Hamilton, K. Trunov, D. Reuter, and A. D. Wieck, "Observation of the kondo effect in a spin-3/2 hole quantum dot," *Phys. Rev. Lett.*, vol. 107, p. 076805, 2011. (Cited on page 18)

[66] N. Ares, V. N. Golovach, G. Katsaros, M. Stoffel, F. Fournel, L. Glazman, O. G. Schmidt, and S. De Franceschi, "Nature of tunable hole g factors in quantum dots," *Phys. Rev. Lett*, vol. 110, p. 046602, Jan. 2013. (Cited on page 27)

[67] R. J. Schoelkopf, P. Wahlgren, A. A. Kozhevnikov, P. Delsing, and D. E. Prober, "The radio-frequency single-electron transistor (rf-set): a fast and ultrasensitive electrometer," *Science*, vol. 280, pp. 1238–1242, 1998. (Cited on pages 32 and 37)

[68] J. C. Frake, S. Kano, C. Ciccarelli, J. Griffiths, M. Sakamoto, T. Teranishi, Y. Majima, C. G. Smith, and M. R. Buitelaar, "Radio-frequency capacitance spectroscopy of metallic nanoparticles," *Scientific Reports*, vol. 5, no. 10858, 2015. (Cited on page 32)

[69] A. O. Orlov, P. Fay, G. L. Snider, X. Jehl, S. Barraud, and M. Sanquer, "Dual-port reflectometry technique: Charge identification in nanoscaled single-electron transistors," *IEEE Nanotechnology Magazine*, vol. 9, pp. 24–32, 2015. (Cited on page 32)

[70] N. Ares, F. J. Schupp, A. Mavalankar, G. Rogers, J. Griffiths, G. A. C. Jones, I. Farrer, D. A. Ritchie, C. G. Smith, A. Cottet, G. A. D. Briggs, and E. A. Laird, "Sensitive radio-frequency measurements

of a quantum dot by tuning to perfect impedance matching," *Phys. Rev. Applied*, vol. 5, p. 034011, 2016. (Cited on pages 32 and 33)

[71] B. J. van Wees, H. van Houten, C. W. J. Beenakker, J. G. Williamson, L. P. Kouwenhoven, D. van der Marel, and C. T. Foxon, "Quantized conductance of point contacts in a two-dimensional electron gas," *Phys. Rev. Lett.*, vol. 60, p. 848, 1988. (Cited on page 37)

[72] Y. Hu, H. O. H. Churchill, D. J. Reilly, J. Xiang, C. M. Lieber, and C. M. Marcus, "A ge/si heterostructure nanowire-based double quantum dot with integrated charge sensor," *Nature Nanotechnology*, vol. 2, pp. 622–625, 2007. (Cited on page 37)

[73] L. M. K. Vandersypen, J. M. Elzerman, R. N. Schouten, L. H. Willems van Beveren, R. Hanson, and L. P. Kouwenhoven, "Real-time detection of single-electron tunneling using a quantum point contact," *Appl. Phys. Lett.*, vol. 85, p. 4394, 2004. (Cited on page 37)

[74] D. J. Reilly, C. M. Marcus, M. P. Hanson, and A. C. Gossard, "Fast single-charge sensing with a rf quantum point contact," *Appl. Phys. Lett.*, vol. 91, p. 162101, 2007. (Cited on page 37)

[75] M. F. Gonzalez-Zalba, S. Barraud, A. J. Ferguson, and A. C. Betz, "Probing the limits of gate-based charge sensing," *Nature Comm.*, vol. 6, no. 6084, 2015. (Cited on page 37)

[76] A. Morello, C. C. Escott, H. Huebl, L. H. Willems van Beveren, L. C. L. Hollenberg, D. N. Jamieson, A. S. Dzurak, and R. G. Clark, "Architecture for high-sensitivity single-shot readout and control of the electron spin of individual donors in silicon," *Phys. Rev. B*, vol. 80, p. 081307, 2009. (Cited on pages 38, 39, and 60)

[77] H. Büch, S. Mahapatra, R. Rahman, A. Morello, and M. Y. Simmons, "Spin readout and addressability of phosphorus-donor clusters in silicon," *Nature Comm.*, vol. 4, no. 2017, 2013. (Cited on pages 38, 66, and 74)

[78] A. I. Yakimov, N. P. Stepina, A. V. Dvurechenskii, A. I. Nikiforov, and A. V. Nenashev, "Excitons in charge ge/si type-ii quantum dots," *Semicond. Sci. Technol.*, vol. 15, pp. 1125–1130, 2000. (Cited on page 38)

[79] J. M. Elzerman, R. Hanson, L. H. W. van Beveren, B. Witkamp, L. M. K. Vandersypen, and L. P. Kouwenhoven, "Single-shot read-out of an individual electron spin in a quantum dot," *Nature*, vol. 430, pp. 431–435, 2004. (Cited on pages 41, 59, and 72)

[80] R. Hanson, L. P. Kouwenhoven, J. R. Petta, S. Tarucha, and L. M. K. Vandersypen, "Spins in few-electron quantum dots," *Rev. Mod. Phys.*, vol. 79, pp. 1217–1265, 2007. (Cited on pages 42 and 66)

[81] L. M. Roth and B. Lax, “g factor of electrons in germanium,” *Phys. Rev. Lett.*, vol. 3, pp. 217–219, 1959. (Cited on page 59)

[82] H. Büch, *Readout and addressability of Si:P qubits with the prospect of scalability*. PhD thesis, UNSW, Australia,Faculty of Science, Schoold of Physics, 2014. (Cited on pages 60 and 70)

[83] F. Maier, C. Kloeffel, and D. Loss, “Tunable g factor and phonon-mediated hole spin relaxation in ge/si nanowire quantum dots,” *Phys. Rev. B*, vol. 87, p. 161305, 2013. (Cited on page 66)

[84] J. M. Elzerman, *Electron spin and charge in semiconductor quantum dots*. PhD thesis, TU Delft, the Netherlands, 2004. (Cited on page 78)

A Fabrication details

A.1 Fabrication of SHTs out of dome islands

A.1.1 Random approach

Step	Step description	Relevant parameters
1	Spin coating	Resist: S1815 Spinning time: 30 sec Spinning speed: 4000 rpm Acceleration speed: 2000 rpm/s Baking time: 20 min at 90°C
2	Optical lithography for alignment crosses and write field electrodes	Exposure time: 30 sec
3	Development	Chlorobenzene dip: 30 sec Developer MF-319 dip: 60 sec Stopper H_2O dip: 60 sec
4	Metal deposition, lift-off and cutting	Cr/Au (10/65) nm Lift-off: 20 min acetone at 55°C Cutting the samples into 5 mm x 5 mm pieces
5a	Spin coating (First layer)	Resist: AR-P 679.02(950K) Spinning time: 30 sec Spinning speed: 6000 rpm Acceleration speed: 2000 rpm/s Baking time: 5 min at 180°C

5b	Spin coating (Second layer)	Resist: AR-P 639.04(50K) Spinning time: 30 sec Spinning speed: 6000 rpm Acceleration speed: 2000 rpm/s Baking time: 5 min at 180°C
6	E-beam lithography for source and drain electrodes	Acceleration voltage 20 kV Beam current: $\sim$ 20 pA
7	Development	Developer AR-P 600-56 dip: 30 sec Stopper IPA dip: 60 sec
8	Metal deposition and lift-off	BOE dip: 10 sec Pt or Pd 20 nm Lift-off: 20 min acetone at 55°C
9	SEM imaging	Acceleration voltage: 5 kV
10	Drawing a design	Software: KLayout or CleWin
11	Spin coating	Resist: AR-P 679.04(950K) Spinning time: 30 sec Spinning speed: 6000 rpm Acceleration speed: 2000 rpm/s Baking time: 5 min at 180°C
12	E-beam lithography for source and drain connections	Acceleration voltage 20 kV Beam current: $\sim$ 60 pA
13	Development	Developer AR-P 600-56 dip: 30 sec Stopper IPA dip: 60 sec
14	Metal deposition and lift-off	Cr/Au (10/90) nm Lift-off: 20 min acetone at 55°C
15	Atomic layer deposition	Chamber temperature: 130°C Precursor (TMAH) temperature: 90°C H_2O pulse duration: 0.015 s TMAH pulse duration: 0.015 s Waiting time before pulses: 5 s Number of cycles: 60
16	Spin coating	Resist: AR-P 679.04(950K) Spinning time: 30 sec Spinning speed: 6000 rpm Acceleration speed: 2000 rpm/s Baking time: 5 min at 180°C

17	E-beam lithography for gate electrodes	Acceleration voltage 20 kV Beam current: $\sim$ 20 pA
18	Development	Developer AR-P 600-56 dip: 30 sec Stopper IPA dip: 60 sec
19	Metal deposition and lift-off	Ti/Pt (3/20) nm Lift-off: 20 min acetone at 55°C
20	Spin coating	Resist: AR-P 679.04(950K) Spinning time: 30 sec Spinning speed: 6000 rpm Acceleration speed: 2000 rpm/s Baking time: 5 min at 180°C
21	E-beam lithography for gate electrodes connections	Acceleration voltage 20 kV Beam current: $\sim$ 60 pA
22	Development	Developer AR-P 600-56 dip: 30 sec Stopper IPA dip: 60 sec
23	Metal deposition and lift-off	Cr/Au (10/90) nm Lift-off: 20 min acetone at 55°C

Table A.1: SHT fabrication steps and important parameters for the random approach. The first four steps are not performed every time. Steps 20-23 can be avoided if there is a RIE step performed before the step 4.

A.1.2 Direct approach

Step	Step description	Relevant parameters
1	Spin coating	Resist: AR-P 679.04(950K) Spinning time: 30 sec Spinning speed: 6000 rpm Acceleration speed: 2000 rpm/s Baking time: 5 min at 180°C
2	E-beam lithography for alignment markers	Acceleration voltage: 20 kV Beam current: $\sim$0.4 nA
3	Metal deposition, lift-off and cutting	Cr/Au (10/65) nm Lift-off: 20 min acetone at 55°C Cutting the samples into 5 mm x 5 mm pieces
4	SEM imaging	Acceleration voltage: 5 kV
5	Drawing a design	Software: eLine Plus

6a	Spin coating (First layer)	Resist: AR-P 679.02(950K) Spinning time: 30 sec Spinning speed: 6000 rpm Acceleration speed: 2000 rpm/s Baking time: 5 min at 180°C
6b	Spin coating (Second layer)	Resist: AR-P 639.04(50K) Spinning time: 30 sec Spinning speed: 6000 rpm Acceleration speed: 2000 rpm/s Baking time: 5 min at 180°C
7	E-beam lithography for source and drain	Acceleration voltage 20 kV Beam current (fine lines): ∼20 pA Beam current (Bonding pads extensions): ∼1.5 nA
8	Development	Developer AR-P 600-56 dip: 30 sec Stopper IPA dip: 60 sec
9	Metal deposition and lift-off	BOE dip: 10 sec Pt or Pd 20 nm Lift-off: 20 min acetone at 55°C
10	Atomic layer deposition	Chamber temperature: 130°C Precursor (TMAH) temperature: 90°C H_2O pulse duration: 0.015 s TMAH pulse duration: 0.015 s Waiting time before pulses: 5 s Number of cycles: 60
11	Spin coating	Resist: AR-P 679.04(950K) Spinning time: 30 sec Spinning speed: 6000 rpm Acceleration speed: 2000 rpm/s Baking time: 5 min at 180°C
12	E-beam lithography for gate electrodes	Acceleration voltage 20 kV Beam current (fine lines): ∼20 pA Beam current (Bonding pads extensions): ∼1.5 nA

13	Development	Developer AR-P 600-56 dip: 30 sec Stopper IPA dip: 60 sec
14	Metal deposition and lift-off	Ti/Pt (3/20) nm Lift-off: 20 min acetone at 55°C

Table A.2: SHT fabrication steps and important parameters for the direct approach. The first three steps are not performed every time.

A.2 Fabrication of coupled dots out of HWs

Step	Step description	Relevant parameters
1	Spin coating	Resist: AR-P 679.04(950K) Spinning time: 30 sec Spinning speed: 6000 rpm Acceleration speed: 2000 rpm/s Baking time: 5 min at 180°C
2	E-beam lithography for gate alignment markers	Acceleration voltage: 20 kV Beam current: $\sim$0.5 nA
3	Metal deposition, lift-off and cutting	Cr/Au (10/65) nm Lift-off: 20 min acetone at 55°C Cutting the samples into 5 mm x 5 mm pieces
4	SEM imaging	Acceleration voltage: 5 kV
5	Drawing a design	Software: eLine Plus
6a	Spin coating (First layer)	Resist: AR-P 679.02(950K) Spinning time: 30 sec Spinning speed: 6000 rpm Acceleration speed: 2000 rpm/s Baking time: 5 min at 180°C
6b	Spin coating (Second layer)	Resist: AR-P 639.04(50K) Spinning time: 30 sec Spinning speed: 6000 rpm Acceleration speed: 2000 rpm/s Baking time: 5 min at 180°C

7	E-beam lithography for source and drain	Acceleration voltage 20 kV Beam current (fine lines): ∼20 pA Beam current (Bonding pads extensions): ∼1.5 nA
8	Development	Developer AR-P 600-56 dip: 30 sec Stopper IPA dip: 60 sec
9	Metal deposition and lift-off	BOE dip: 10 sec Pd/Al (10/28) nm Lift-off: 20 min acetone at 55°C
10	Spin coating	Resist: AR-P 6200.09 Spinning time: 30 sec Spinning speed: 4000 rpm Acceleration speed: 2000 rpm/s Baking time: 5 min at 150°C
11	E-beam lithography for gate electrodes	Acceleration voltage 20 kV Beam current (fine lines): ∼20 pA Beam current (Bonding pads extensions): ∼0.4 nA
12	Development	Developer AR-P 600-549 dip: 60 sec Stopper IPA dip: 30 sec
13	Atomic layer deposition	Chamber temperature: 130°C Precursor (TMAH) temperature: 90°C H_2O pulse duration: 0.045 s Waiting time before pulses: 10 s TMAH pulse duration: 0.015 s Waiting time before pulses: 5 s Number of cycles: 60
14	Metal deposition and lift-off	Ti/Pd (10/15) nm Lift-off: 20 min acetone at 55°C

Table A.3: Charge sensing in hut wires fabrication steps. The first three steps are not performed every time.

B Electrical circuit components

B.1 Tunnelling times

This experiment was carried out in a *CF-CS81-1400-MAG* dilution refrigerator from Leiden Cryogenics. We used a CITLF3 cryogenic amplifier, a ZX60-P103LN+ room temperature amplifier and a DBTC-7-152LX+ directional coupler.

The PCB components are given in Table B.1.

B.2 Relaxation times

This experiment was carried out in a *LD-250 EO* dilution refrigerator from BlueFors Cryogenics. We used a CITLF2 cryogenic amplifier, a ZX60-33LN-S+ room temperature amplifier and a ZX30-9-4-S+ directional coupler.

The PCB components are given in Table B.2.

	Stand-alone DC lines	Reflectometry lines	Fast gate lines
RC filter	R = 10 kΩ (PNM0603E1002BST5) C = 10 nF (C0805X103J5GACAUTO)	-	-
Bias tee	-	R = 10 kΩ (PNM0603E1002BST5) C = 10 nF (C0805X103J5GACAUTO)	R = 1.8 MΩ (MMU01020C1804FB300) C = 10 nF (C0805X103J5GACAUTO)
LC tank circuit	-	L_1 = 820 nH (LQW2UASR82J00L) L_2 = 1200 nH (LQW2UAS1R2J00L) L_3 = 2200 nH (LQW2UAS2R2J00L) L_4 = 4700 nH (LQW2UAS4R7J00L) C: parasitic capacitance	-

Table B.1: Elements on the PCB board used in the tunnelling time experiment. The manufacturer numbers are given in brackets.

	Stand-alone DC lines	Reflectometry lines	Fast gate lines
RC filter	R = 10 kΩ (MMU01020C1002FB300) C = 10 nF (C0805X103J5GACAUTO)	-	-
Bias tee	-	R = 10 kΩ (MMU01020C1002FB300) C = 10 nF (C0805X103J5GACAUTO)	R = 1.8 MΩ (MMU01020C1804FB300) C = 10 nF (C0805X103J5GACAUTO)
LC tank circuit	-	L_1 = 220 nH (1206CS-221XJLB) L_2 = 470 nH (1206CS-471XJLB) L_3 = 820 nH (1206CS-821XJLB) L_4 = 1200 nH (1206CS-122XJLB) 4 × C varactor (MA46H070-1056)	-

Table B.2: Elements on the PCB board used in the relaxation time experiment. The manufacturer numbers are given in brackets.

C Rise time calculation

A simple calculating showing the connection between the rise time and the bandwidth for a simple one-stage low-pass RC filter is presented.

The rise time is defined as the time required for a pulse to rise from 10 % to 90 % of its steady value:

$$V(t_1) = 0.1V_0, \qquad V(t_2) = 0.9V_0, \tag{C.1}$$

where V_0 is the amplitude of the input signal.

The response of an RC network is

$$V(t) = V_0(1 - e^{-t/RC}). \tag{C.2}$$

From

$$\frac{V(t)}{V_0} - 1 = -e^{-t/RC}, \tag{C.3}$$

$$ln(1 - \frac{V(t)}{V_0}) = -\frac{t}{RC}, \tag{C.4}$$

we get

$$t = -RC\ln(1 - \frac{V(t)}{V_0}). \tag{C.5}$$

In the next step we plug in the values for t_1 and t_2 from the equation C.1:

$$t_1 = -RC\ln(1-0.1) = -RC\ln(0.9) = -RC[\ln(9) - \ln(10)] = RC[\ln(10) - \ln(9)], \tag{C.6}$$

$$t_2 = -RC\ln(1-0.9) = -RC\ln(0.1) = -RC[\ln(1) - \ln(10)] = RC[\ln(10) - \ln(1)] = RC\ln(10). \tag{C.7}$$

For the rise time t_r we get:

$$t_r = t_2 - t_1 = RC[\ln(10) + \ln(9) - \ln(10)] = RC\ln 9 \approx 2.2RC \tag{C.8}$$

Noting that for the low-pass RC network the time constant RC is equal to

$$RC = \frac{1}{2\pi f}, \tag{C.9}$$

the rise time is equal to

$$t_r = \frac{2.2}{2\pi f}. \tag{C.10}$$

Since the high frequency cut-off is equal to the bandwidth we finally get

$$t_r \approx \frac{0.35}{bandwidth} \tag{C.11}$$

D Software

D.1 Measurement scripts

The measurement scripts I used are based on QTLab (http://qtlab.sourceforge.net/), written in Python 2.7 and can be found on https://github.com/nanoelectronics-new/qtlab. Josip Kukučka edited most of the scripts according to our equipment. I have merely adapted them while the experiment was progressing.

D.2 Analysis scripts

The analysis scripts were as well written in Python 2.7. Here I will give parts of the code for the single-shot analysis, measurement fidelity analysis and averaged analysis.

Single-shot analysis: relaxation time and parameter α

```
import numpy as np
import matplotlib.pyplot as plt
from scipy.optimize import curve_fit, least_squares
%matplotlib inline
import os
import win32api

path_500mT = 'K:\\Measurement\\Lada\\November17\\20171112\\234417_ Break2 T1_meas 36 traces over 5000 200
    kHz By=500mT -35dBm read -2.4mV #140\\'

mat_500mT = np.loadtxt(path_500mT + 'averaged over 2365') #importing previously averaged single-shot
    measurement
num_samples_500mT, num_rows_500mT = np.shape(mat_500mT)
```

```
duration = 1500 #what is displayed on the scope; duration of the recorded part
step_500mT = float(duration)/num_samples_500mT

loading_time = np.array([2, 4, 6, 8, 10, 12, 15, 20, 25, 30, 35, 40, 45, 50, 55, 60, 65, 70, 75, 80, 85,
    90, 95, 100, 105, 110, 115, 120, 125, 130, 150, 200, 250, 300, 400, 500])

#start and stop should be duration of the readout phase
start = 91.2 #in us, when the pulse is actually applied
stop = 141.2

drawing_500mT = np.loadtxt(path_500mT + 'result_CH1matrix5') #loading just one single-shot matrix to
    determine averaged min and max RA
plt.plot(drawing_500mT[int(0/step_500mT):int(1400/step_500mT), 35]) #drawing one trace

min_500mT = np.mean(drawing_500mT[0:5000,35]) #averaged min RA
max_500mT = np.mean(drawing_500mT[7000:10000,35]) #averaged max RA
print (min_500mT, max_500mT)

threshold65_500mT = ((max_500mT - min_500mT)*0.65) + min_500mT #determining threshold

###Analyzing single shots, for each matrix we check if there is an event (if there is RA higher than
    threshold). If yes, we append the list.

tw_500mT_thr65 = [0 for i in range(num_rows_500mT)] #just creating a list full of zeros

ref_matrix = np.loadtxt(path_500mT + 'result_CH1matrix1')

#now counting
for j in range (1,2365):
    temp = np.loadtxt(path_500mT + 'result_CH1matrix' + str(j))
    if np.shape(temp) == np.shape(ref_matrix): #if shape is different means that sth was saved wrongly, can
      happen, that's why we are checking

        for k in range(num_rows_500mT):
            if max(temp[int(start/step_500mT):int(stop/step_500mT), k]) >= threshold65_500mT:
                tw_500mT_thr65[k] = tw_500mT_thr65[k] + 1




###############################################################################
###Plotting and extracting T1 and parameter alpha, together with standard deviations
###############################################################################

tw_500mT_thr65 = np.array(tw_500mT_thr65)
plt.plot(loading_time[4:],tw_500mT_thr65[4:]/2365.0, '.') #taking loading times from 10us
plt.title('single shot 500mT from 10 (incl) for threshold ' + str(threshold65_500mT))

def exponential_func(x, a, b, c):  #defining the fit function
    return a*(np.exp(b*x))+c

xaxisforfit = loading_time[4:]
popt, pcov = curve_fit(exponential_func,xaxisforfit, tw_500mT_thr65[4:]/2365.0 ,p0=(1, -6e-2, 70))
fit = exponential_func(xaxisforfit, *popt)
```

```
plt.plot(xaxisforfit, fit, color = '#FF6600', lw = 2)
ax = plt.gca()
ax.get_xaxis().get_major_formatter().set_useOffset(False)
plt.show()


a = popt[0]
b_500mT_thr65 = popt[1]
c = popt[2]


perr_b_500mT_thr65 = np.sqrt(np.diag(pcov))

print (a,b_500mT_thr65,c) #parameter c is actually alpha

print 'standard deviation for a, b, c: ', perr_b_500mT_thr65  #parameter c is actually alpha
print 'standard deviation for b: ', perr_b_500mT_thr65[1]
print ('Relaxation time at 700mT in microseconds for threshold ' + str(threshold65_500mT), (-1/
    b_500mT_thr65))
print('*********************************************\n')

stdev_b = round(perr_b_500mT_thr65[1], 3) #rounding has to be changed manually, depending on the extracted
    values!
mean_b = round(b_500mT_thr65, 3) #rounding has to be changed manually, depending on the extracted values!
print stdev_b, mean_b
t = -1/mean_b
print t
stdev_t = stdev_b/(mean_b**2)
print stdev_t
```

Single-shot analysis: parameter β

Part of the code for extracting β.

```
####################
###Extracting beta
#####################

#first determining t_detect (If there is an event, when does it appear?)

t_detect_500mT_tr65 = [] #just creating an empty list

#I need one matrix as a reference shape in order to eliminate empty/wrongly saved files
ref_matrix = np.loadtxt(path_500mT + 'result_CH1matrix1')

#now counting
for j in range (1,2365): #allofthem
    temp = np.loadtxt(path_500mT + 'result_CH1matrix' + str(j))
    if np.shape(temp) == np.shape(ref_matrix): #if shape is different means that sth was saved wrongly
        for k in range(4, num_rows_500mT):      #again from 10us
```

```
        index_trace_tr65 = np.argmax(temp[int(start/step_500mT):int(stop/step_500mT), k] >=
    threshold65_500mT)
            if index_trace_tr65 != 0: #I guess
                t_detect_500mT_tr65 += [index_trace_tr65*step_500mT]


#plotting the histogram of t_detect, fitting and extracting values

noBins = 50

plt.hist(t_detect_500mT_tr65, noBins)
#plt.show()

binHeights, binEdges = np.histogram(t_detect_500mT_tr65,noBins)[:2]
binCenters = (binEdges[:-1] + binEdges[1:])/2
plt.title('Histogram t_detect 500mT for threshold ' + str(threshold65_500mT) )
plt.plot(binCenters, binHeights, '.', color = 'k')

xaxisforfit = binCenters[np.argmax(binHeights):]


def exponential_func(x, a, b, c):
    return a*(np.exp(b*x))+c
popt, pcov = curve_fit(exponential_func,xaxisforfit,binHeights[np.argmax(binHeights):]
,p0=(1, -6e-2, 0))
fit = exponential_func(xaxisforfit, *popt)

plt.plot(xaxisforfit, fit, color = '#FF6600', lw = 2)
ax = plt.gca()
ax.get_xaxis().get_major_formatter().set_useOffset(False)
plt.show()


a = popt[0]
b_500mT_tr65 = popt[1]
c = popt[2]


perr_b_500mT_tr65 = np.sqrt(np.diag(pcov))

print (a,b_500mT_tr65,c)

print ('standard deviation for a, b, c: ', perr_b_500mT_tr65)
print ('standard deviation for b: ', perr_b_500mT_tr65[1])
print ('Tunnelling time ', (-1/b_500mT_tr65))
print('*****************************************\n')

stdev_b = round(perr_b_500mT_tr65[1], 3)
mean_b = round(b_500mT_tr65, 3)
print ('devijacija, b', stdev_b, mean_b)
t = -1/mean_b
print (t)
stdev_t = stdev_b/(mean_b**2)
print (stdev_t)
```

```
##############################################
###Calculating beta from the extracted values
##############################################


#relaxation time depending on the threshold, rounded, from lower to higher threshold
t1_500mT = np.array([70.0, 90.0, 88.0, 85.0, 88.0, 88.0, 88, 87.0, 88.0, 86.0, 87.0])
t1_500mT_dev = np.array([30.0, 20.0, 7.0, 6.0, 5.0, 5.0, 5.0, 5.0, 5.0, 6.0, 5.0])

gamma1_500mT = np.array([0.086, 0.104, 0.125, 0.132, 0.134, 0.131, 0.119, 0.126, 0.120, 0.125, 0.105])
gamma1_500mT_stdev = np.array([0.004, 0.007, 0.007, 0.007, 0.007, 0.008, 0.006, 0.007, 0.005, 0.007,
    0.005])

beta_500mT_calc = 1/(1 + t1_500mT*gamma1_500mT)
beta_500mT_stdev_calc = np.sqrt(( (t1_500mT*gamma1_500mT_stdev)/(1 + t1_500mT*gamma1_500mT)**2 )**2 +  ( (
    gamma1_500mT*t1_500mT_dev)/(1 + t1_500mT*gamma1_500mT)**2 )**2)
```

Averaged analysis

```
import numpy as np
import matplotlib.pyplot as plt
from scipy.optimize import curve_fit, least_squares
import scipy
%matplotlib inline
import os

path_500mT = 'K:\\Measurement\\Lada\\November17\\20171112\\234417_ Break2 T1_meas 36 traces over 5000 200
    kHz By=500mT -35dBm read -2.4mV #140\\'

mat_500mT = np.loadtxt(path_500mT + 'averaged over 2365')
num_samples_500mT, num_rows_500mT = np.shape(mat_500mT)

duration = 1500 #what is displayed on the scope
step_500mT = float(duration)/num_samples_500mT

loading_time = np.array([2, 4, 6, 8, 10, 12, 15, 20, 25, 30, 35, 40, 45, 50, 55, 60, 65, 70, 75, 80, 85,
    90, 95, 100, 105, 110, 115, 120, 125, 130, 150, 200, 250, 300, 400, 500])

#to plot it a correct scale)
t_500mT = np.linspace(0*step_500mT, num_samples_500mT*step_500mT, num_samples_500mT)

#plotting one averaged trace to see where it saturates
plt.plot(t_500mT[int((91.2)/step_700mT):int(700/step_700mT)], mat_500mT[int((91.2)/step_700mT):int(700/
    step_700mT),7])


#calculating offset
offset_500mT = []
for i in range(len(loading_time)):
    offset_500mT += [np.mean(mat_500mT[int((250)/step_500mT):int(450/step_500mT),i])] #starts to saturate
    around 250us. I took values until 450
```

```
print offset_500mT


#substracing the offset
mat_500mT_norm_2 = mat_500mT
for i in range(len(loading_time)):
    mat_500mT_norm_2[int((91.2)/step_500mT):int(700/step_700mT),i] = mat_500mT_norm_2[int((91.2)/step_700mT
    ):int(700/step_500mT),i] - offset_500mT[i]



################################################
###Calculating the area with the trapz function
################################################

from numpy import trapz
area_t_500mT = np.array([])

mat_500mT_norm_positive = np.zeros((len(t_500mT[int((a_start)/step_500mT):int(350/step_500mT)]),
    num_rows_500mT))

for i in range(len(loading_time)):
    temp_mat_500mT_norm_positive = np.array([])

    for point in mat_500mT_norm_2[int(a_start/step_500mT):int(350/step_500mT), i]:
        if point > 0:
            temp_mat_500mT_norm_positive = np.append(temp_mat_500mT_norm_positive, point)
        else:
            temp_mat_500mT_norm_positive = np.append(temp_mat_500mT_norm_positive, 0.0)
    area_t_500mT = np.append(area_t_500mT, trapz(temp_mat_500mT_norm_positive, x = t_500mT[int((a_start)/
    step_500mT):int(350/step_500mT)], axis = 0))


print area_t_500mT
print np.shape(area_t_500mT)


########################
###Plotting and fitting
########################

plt.plot(loading_time[7:], area_t_500mT[7:]) #From 20us loading time, since there were strage artefacts for
     shorter loading times
plt.title('Field = 500mT, from time traces = ' + str(a_start) + '-' + str(a_stop), fontsize = 12)
def exponential_func(x, a, b, c):
    return a*(np.exp(b*x))+c

xaxisforfit = loading_time[7:]
popt, pcov = curve_fit(exponential_func,xaxisforfit, area_t_500mT[7:] ,p0=(0.0002, -0.01, 0.0035))
fit = exponential_func(xaxisforfit, *popt)

plt.plot(xaxisforfit, fit, color = '#FF6600', lw = 2)
ax = plt.gca()
ax.get_yaxis().get_major_formatter().set_useOffset(False)
```

```
plt.show()


Aa = popt[0]
Ab_500mT_no8 = popt[1]
Ac = popt[2]


perr_b_500mT = np.sqrt(np.diag(pcov))

print ('a, b, c'), (Aa,Ab_500mT_no8,Ac)


print 'standard deviation for a, b, c: ', perr_b_500mT
print 'standard deviation for b: ', perr_b_500mT[1]
print ('Relaxation time at 500mT from area '), (-1/Ab_500mT_no8)


stdev_b = round(perr_b_500mT[1], 3)
mean_b = round(Ab_500mT_no8, 3)
print stdev_b, mean_b
t = -1/mean_b
print t
stdev_t = stdev_b/(mean_b**2)
print stdev_t
```